ABSTRACT

Title of Dissertation: THE APPLICATIONS OF MULTIPHOTON ABSORPTION POLYMERIZATION

Sijia Qin, Doctor of Philosophy, 2013

Directed By: Professor John T. Fourkas, Department of Chemistry and Biochemistry

Among various nano/micro-fabrication techniques, multiphoton absorption polymerization (MAP) stands out for its high resolution and its capability of creating arbitrary three-dimensional micro-structures. This thesis will focus on the applications of, and improvements to, MAP.

MAP was used to fabricate polymer double-ring resonators (DRRs) because MAP's high resolution allows for precise control of the coupling gap sizes. Pedestal acrylic DRRs with 33 nm free spectral range and -15 dB isolation were fabricated, and their properties showed qualitative agreement with simulation results.

Single-mode, acrylic microring resonator devices were fabricated on a low-index substrate using MAP and were coupled to side-polished fibers as in-line devices. High-finesse spectral notches with low insertion loss were observed at the

fiber output. Surface mapping of the polished face of the fiber was accomplished by moving a microring resonator device across and along the fiber core. The optimal coupling region on the polished face of the fiber could be identified through the change of modulation depth. Spectral modulation induced by varying the pressure on a microring resonator device coupled to a side-polished fiber was also investigated.

Efficient multiphoton radical generation chemistry has been developed for use in aqueous media and has been applied to the fabrication, manipulation, and assembly of 3-D polymeric and biomolecular structures through a combination of MAP and optical tweezers. The combination of MAP and optical tweezers allows for the realization of structures such as tape-like and rope-like microthreads that can be used in complex microfabrication techniques such as microbraiding and microweaving. These capabilities enhance the toolbox of methods available for the creation of functional microstructures in aqueous media.

MAP-fabricated and UV-cured acrylic patterns were treated with reactive ion etching (RIE) to create high-roughness "nanograsses." The nanograss patterns have shown the potential to be used as superhydrophobic materials. The density and dimension of the nanograss depends on the total exposure dose. Different etch angles gave different etch structures.

THE APPLICATIONS OF MULTIPHOTON ABSORPTION POLYMERIZATION

By

Sijia Qin

Dissertation submitted to the Faculty of the Graduate School of the
University of Maryland, College Park, in partial fulfillment
of the requirements for the degree of
Doctor of Philosophy
2013

Advisory Committee:

Professor John T. Fourkas, Chair

Professor Neil Blough

Professor Julius Goldhar

Professor Amy Mullin

Professor Janice Reutt-Robey

© Copyright by

Sijia Qin

2013

Acknowledgements

This thesis would not have been possible without the guidance, help and support from many important individuals. I'd like to express my sincere appreciation to all of them.

First, my gratitude must go to my advisor Dr. John T. Fourkas. Without his support, this thesis would remain only a dream. I couldn't find a better sentence to describe John than what Dr. Linjie Li said in his thesis, thus I must cite it here: "One simply could not wish for a better or friendlier supervisor." This is exactly who John is. He provides plenty of sparkling ideas, and tons of practical suggestions. His abundant knowledge, patience, and always encouraging feedback have sustained me throughout the last 5 years. I'm extremely lucky to be advised by him.

I also wish to thank all of the group members.

I owe deep gratitude to Dr. Linjie Li who helped me start my first research project. He gave enormous suggestions, and help to me for academics, and also for normal life. He is a great teacher and also a good friend.

I owe Dr. Qin Zhong many thanks also for his suggestions on choosing research groups, which enabled me to make the wisest decision.

Dr. Rafael Gatass' conscientious attitude to science, and his humor in daily life leave me a deep impression and a long-term impact.

I considered it an honor to work with Dr. George Kumi. George has been helping me with the project of resonator fabrication for two years. He has everything that one need to be an excellent scientist, and a great teacher. He is smart, patient, knowledgeable, curious, persistent, and diligent. He has set a remarkable example for

me. I could always expect positive feedback and helpful tips from him. I wish I had known him earlier.

Dr. Farah Dawood has helped me throughout the whole project of simultaneous manipulation, fabrication, and positioning in aqueous system. I will never forget all those funny chatting time chats in the summer of 2010.

I am grateful to all the colleagues in our group. Thanks Dr. Kathleen Monaco for the safety training. Thanks go to Dr. Sanghee Nah for all the happy lunch time together. I thank Dr. Mike Stocker for all his delicious snacks. Thanks Alison Sikorsky for always helping me to take care of my samples. Thanks to Floyd Bates and Xiaoyu Sun for help with PDMS molding. Thanks to Dr. Samrat Dutta, Matt Hourwitz and Shirl Phelps for useful writing suggestions. Thanks to Xiaoxiao He for beiing a nice officemate and friend. Thanks to Emily Lin for helping with the BSA fabrication. Thanks also go to other group members: Dr. Chris Rivera, Zulya Tomova, John Bender, Jarrett Leeds, and Dr. Carlos Toro.

I wish to thank all the co-workers in LPS who offered me great help with my research.

It is with immense gratitude that I acknowledge the support and help of Dr. Warren Herman, the project manager in Laboratory for Physical Science (LPS), who is always kindly and careful. He gives steadfast encouragement and pertinent suggestions at weekly meetings. I also appreciate his help on Matlab programming.

Dr. Julius Goldhar always brings all kinds of outstanding and even crazy ideas together with his typical, loud laughter.

I am indebted to Dr. Donghun Park for his unselfish and unfailing guidance in the field of optics and electronic engineering. I received big help from him for

simulation, programming, and experiments. Those valuable suggestions and discussions always benefited and improved my research.

I would like to thank Victor Yun for his help in mechanical engineering and also in "finding lost parts". I also appreciate his valuable suggestions.

I want to thank Dr. Pak Cho for comprehensive and beautiful simulations for the project of double ring resonators, and also for paper revising.

Many thanks also go to Dr. P. T. Ho for all the explanations about ring resonators, and to Dr. Yongzhang Leng for research guidance and the green tea.

Special thanks to my committee, Dr. John T. Fourkas, Dr. Neil Blough, Dr. Julius Goldhar, Dr. Amy Mullin, and Dr. Janice Reutt-Robey for their support, guidance, and helpful suggestions. I owe them my sincere appreciation.

I would like to thank Dr. Wen-An Chiou and Li-Chung Lai for help with SU-70 SEM. All the SEM images were taken in Maryland Nanocenter at University of Maryland, College Park.

Lastly, I wish to thank my parents for their selfless and everlasting love. Thanks for bringing me up and loving me whenever and wherever. I would like to thank my husband who lets me know that I am never alone.

Most of the work presented in this thesis was supported by funds from the National Science Foundation.

Table of Contents

Acknowledgements ii
Table of Contents v
List of Figures ix

Chapter 1: Microfabrication Techniques 1

1.1 Introduction 1

1.2 Parallel methods 2

1.2.1 Contact lithography 2

1.2.2 Proximity lithography 3

1.2.3 Projection lithography 3

1.2.4 Extreme UV lithography and X-ray lithography 4

1.2.5 Electron projection lithography and ion projection lithography 5

1.3 Serial methods 5

1.3.1 Electron-beam lithography 5

1.3.2 Focused ion beam lithography 6

1.3.3 Atomic force microscopy (AFM) lithography 6

1.3.4 Nano-imprint lithography 6

1.4 Multiphoton absorption polymerization 7

1.4.1 Fundamentals of MAP 7

1.4.2 Experimental setup of MAP 10

1.5 The improvements and applications of MAP 11

1.5.1 High-speed MAP and fabrication of microfluidic devices 11

1.5.2 MAP and MA-μTM 12

1.5.3 MAP-fabricated microring resonators 13

1.5.4 MAP-fabricated movable structures 15

References 17

Chapter 2: MAP-Fabricated Double-Ring Resonators 21

2.1 Introduction 21

2.1.1 Microring resonators 21

2.1.2 Double-ring resonators 22

2.2 Fundamentals of microring resonators 24

2.2.1 Definitions 24

2.2.2 Microring resonators 25

2.2.3 Double-ring resonators 29

2.3 Experiments and data analysis 32

2.3.1 Sample preparation 32

2.3.2 Serial double-ring resonators 33

2.3.3 Cascaded double-ring resonators 38

2.3.3 Thermal reflow 40

2.4 Conclusions 41

References 42

Chapter 3: Surface mapping of side-polished fibers with externally actuatable microring resonators 47

3.1 Introduction 47

3. 2 Experimental details 50

3.3 Results and discussion 54

3.3.1 Spectral properties of single racetrack resonator on an SPF 54

3.3.2 SPF surface mapping 55

3.3.3 Pressure sensing using a microring resonator on an SPF 57

3.3.4 Waveguides with a pedestal cross section 59

3.3.5 Effect of the coupling region length 60

3.4 Conclusions 61

References 62

Chapter 4: Simultaneous Optical Microscale Manipulation, Immobilization, and Fabrication in Aqueous Media 65

4.1 Introduction 65

4.2 Materials and methods 69

4.2.1 Preparation of acrylate-functionalized glass substrates 69

4.2.2 Preparation of fluorinated substrates 69

4.2.3 Photoinitiator synthesis 70

4.2.4 Water-soluble acrylic photoresist 71

4.2.5 Biophotoresist 72

4.2.6 Fabrication of free-standing microstructures 73

4.2.7 Fabrication and development of structures with water-soluble photoresist 73

4.2.8 Simultaneous optical trapping and fabrication 74

4.2.9 Two-photon fluorescence imaging 75

4.3 Results and discussion 75

4.3.1 MAP and optical tweezers for constructing two- and three- dimensional structures 75

4.3.2 3-D structures consisting of silica microbeads 76

4.3.3 Structures consisting of silica microbeads and acrylic polymer features. 77

4.3.4 Biomolecular materials 82

4.4 Conclusions 85

References 86

Chapter 5: Reactive-Ion-Etched Nanograss Fabricated using MAP and UV Exposure 92

5.1 Introduction 92

5.2 Experiments and Results 96

5.2.1 RIE-treated MAP-fabricated acrylic film 96

5.2.2 Velocity of MAP 97

5.2.3 RIE-treated UV-cured acrylic films 100

5.2.4 Tilted RIE 102

5.3 Conclusions 104

References: 106

Chapter 6: Conclusions and Future Works 113

6.1 Conclusions 113

6.2 Future work 115

6.2.1 On-chip optical devices 115

6.2.2 Side-polished optical fibers 117

6.2.3 MAP in aqueous system 118

6.2.4 Nanograss and superhydrophobicity 118

References:..120

List of Figures

Figure 1.1 Diagrams of the basic lithography setups....4

Figure 1.2 One-photon vs. two-photon excitation. 8

Figure 1.3 MAP-fabricated microstructures 9

Figure 1.4 Experimental setup of MAP. 10

Figure 1.5 Microfluidic channels fabricated using high-speed MAP 12

Figure 1.6 MA- μTM of an arch 13

Figure 1.7 MAP-fabricated microring resonators 14

Figure 1.8 MAP-fbricated microturbine 16

Figure 2.1 Examples of microresonators 22

Figure 2.2 An example of double-ring resonators. 23

Figure 2.3 The schematic of a waveguide coupler 24

Figure 2.4. Schematic of a single microring resonator. 26

Figure 2.5. Transmission characteristics of a resonator....29

Figure 2.6. Schematic of a DRR device....30

Figure 2.7. A typical drop-port spectrum of a DRR device....31

Figure 2.8. Scheme for sample preparation. 33

Figure 2.9. SEM images of acrylic couplers....34

Figure 2.10. Plot of coupling/transmission coefficient vs. coupling gap sizes....35

Figure 2.11. SEM images of DRRs with pedestals....35

Figure 2.12. Simulation results vs. experimental data for DRRs....37

Figure 2.13. Polarization dependance of a DRR device. 38

Figure 2.14. A cascaded DRR device 39

Figure 2.15. Thermal reflow 40

Figure 3.1. SEM of SPF cross sections 49

Figure 3.2. Simulation results 50

Figure 3.3. SEM image of a μRR device 52

Figure 3.4. Schematic diagram of the resonator-based SPF device measurement setup 52

Figure 3.5. Schematic diagram of the optical measurement system 54

Figure 3.6. Through and drop ports spectra for a racetrack μRR device on SPF 55

Figure 3.7 SPF surface mapping 56

Figure 3.8. Pressure sensing 57

Figure 3.9. Cross section: pedestal vs. rectangular 59

Figure 3.10. Coupling-length effect 60

Figure 4.1 Absorption spectrum of MBS. 70

Figure 4.2 Schematic diagram of the experimental setup for simultaneous optical trapping and MAP. 74

Figure 4.3 “UMD” 76

Figure 4.4 Silica microbead pyramid and cube. 77

Figure 4.5 Schematic representation of fabrication Method I. 78

Figure 4.6 Microscale tetherball pole 79

Figure 4.7 Schematic representation of fabrication Method II 80

Figure 4.8 Microscale needle eye 81

Figure 4.9 Microthreads braided using optical tweezers 82

Figure 4.10 Maze and pyramid created in BSA. 83

Figure 4.11 Fluorescence intensity image of microwoven threads of acrylic polymer and BSA 85

Figure 5.1. Superhydrophobic structures 93

Figure 5.2. Applications of the superhydrophobic coating 94

Figure 5.3. An acrylic waveguide with nanograss feature 96

Figure 5.4. MAP (high speed)-fabricated nanograss 98

Figure 5.5. MAP (middle speed)-fabricated nanograss 99

Figure 5.6. MAP (low speed)-fabricated nanograss. 100

Figure 5.7. UV-cured nanograss 101

Figure 5.8. Tilted-RIE-treated, MAP-fabricated nanograss...................................... 103

Figure 5.9. Tilted-RIE-treated, UV-cured nanograss... 103

Figure 5.10. Comparasion and conclusions 105

Figure 6.1. PDMS pedestal 115

Figure 6.2. New photoresist NOA61 116

Figure 6.3. NOA61 vs. acrylic resin 117

Chapter 1: Microfabrication Techniques

1.1 Introduction

Recently, nano- and micro- sized structures and materials have drawn significant attention. Owing to their unique characteristics they have been used for a variety of applications [1]. For instance, due to the large surface area of nano structures, solar-cell devices composed of nano-structured thin films provide much higher efficiency of light capture and electron-hole separation and transport than do bulk materials [1]. Similarly, microfluidic devices that consist of multiple channels printed on a single piece of paper can be used for field diagnostics [2]. These devices provide the opportunity to perform diverse analysis on a single drop of analyte. Another important application of micro-fabrication is in electrical and optical on-chip microarrays [3], which enable the creation of thinner and lighter electronic devices. In micro-fabrication processes, many micro-sized functional units can be put on a single chip, leading to reduced usage of materials and lower cost.

The advantages of nano/micro structures have raised the demand for better fabrication techniques that can provide higher resolution, easier fabrication, and mass production. In this chapter, I will briefly discuss several conventional micro-fabrication techniques along with their advantages and drawbacks. Later, I will highlight multiphoton absorption polymerization, a nontraditional lithographic technique that enables fabrication of improved micro devices.

The micro-fabrication methods can be divided into two different classes: parallel and sequential writing. In the following, I will discuss each in turn.

1.2 Parallel methods

Parallel writing allows an entire pattern to be made simultaneously in a single step, such as with ultraviolet (UV) exposure. Normally, a mask containing the feature information needs to be designed and fabricated in advance, and then is used for the parallel writing process. Parallel writing is fast, as the whole structure can be obtained in a single step. However, it requires a mask for each individual design, and its resolution is limited by diffraction. Moreover, parallel writing is not suitable for creating complicated three-dimensional (3D) designs, such as those with regions of different heights or featuring a spherical wall. Here I give a brief introduction to some common parallel writing methods, such as contact, proximity and projection lithography, X-ray lithography, extreme UV lithography, electron projection lithography, and ion projection lithography. Among these techniques, contact, proximity and projection optical lithography are the most well-known methods that use electromagnetic radiation.

1.2.1 Contact lithography

Contact lithography [4] requires intimate contact between a photoresist [5] and the chrome side of a mask, as shown in Figure 1.1(a). Ideally, no gap exists at the interface, and diffraction effects are significantly reduced, allowing sub-micron resolution to be achieved. However, having no gap places extremely high demands on the treatment and cleanliness of the sample, as any debris in the interface can cause

serious damage to the sample and the mask, leave defects in the pattern, and reduce the resolution. If either the mask or photoresist is not perfectly planar, it is impossible to achieve intimate contact over the entire substrate. Moreover, there is no feature size reduction realized in this technique, as the photoresist receives a 1:1 copy of the mask pattern.

1.2.2 Proximity lithography

As illustrated in Figure 1.1(b), proximity lithography is similar to contact lithography except that the photoresist and the mask are separated by a distance of 10-30 microns. The defects caused by the debris in the physical contact step are reduced with this micro gap, while the resolution decreases to 2-4 μm due to near-field diffraction (Fresnel diffraction) [6]. The aligner used to set the accurate gap adds extra complexity and cost to the method as well. The mask and the fabricated pattern are in a 1:1 dimensional ratio, so there is no image reduction.

1.2.3 Projection lithography

Figure 1.1(c) shows a diagram of the basic setup for projection lithography, in which the mask is held far away from the photoresist and its image is projected onto the resist by lenses. Limited by the Fraunhofer diffraction [7], projection lithography may reach a resolution of around 100 nm with correction techniques. The step-repeat projection [8] approach uses the whole pattern on the mask and projects it onto a small area of the substrate. The substrate is then moved to allow a neighboring area to be exposed. Overall, projection lithography significantly decreases the number of defects and improves the yield rate, but it requires an expensive system and has relatively low resolution.

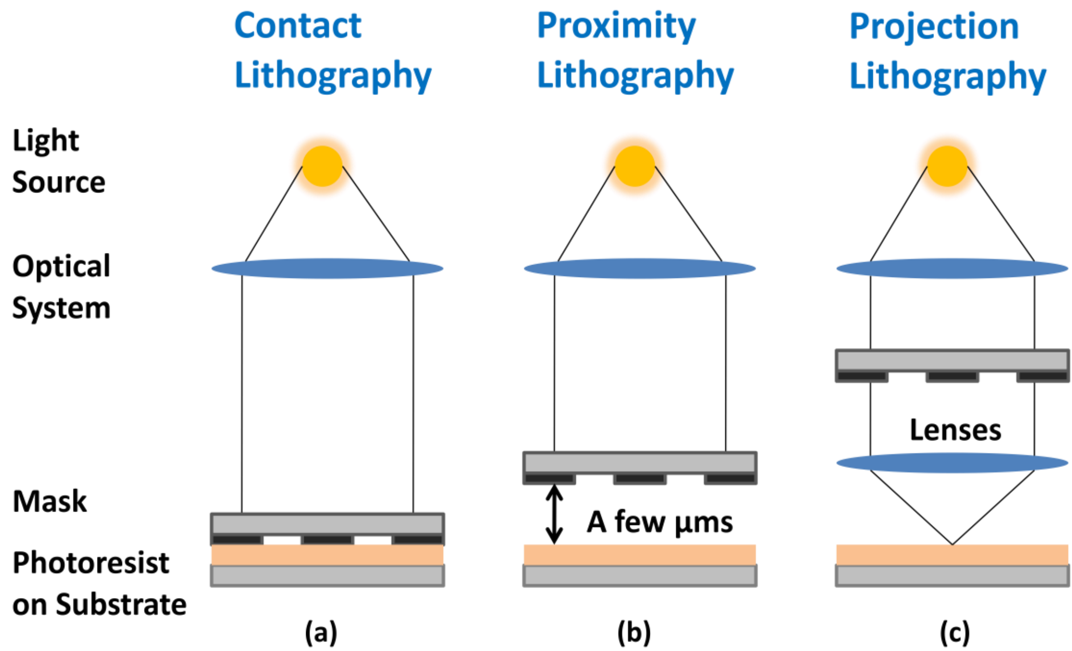

Figure 1.1. Diagrams of the basic experimental setups for (a) contact lithography, (b) proximity lithography and (c) projection lithography

1.2.4 Extreme UV lithography and X-ray lithography

Extreme ultraviolet (EUV) lithography uses radiation with a wavelength of 10-15 nm. To date, EUV lithography has attained resolution as fine as 20 nm [9]. The disadvantage of EUV lithography is that the fabrication system is expensive and EUV radiation is strongly absorbed by all materials. X-ray lithography is analogous to EUV lithography but uses even shorter wavelengths (0.5 – 2 nm), leading to diffraction-limited structures with higher resolution [10]. However, EUV and X-rays are also difficult to manipulate and require a large amount of power to generate. Moreover, the huge investment required and the poor transparency of most materials prevented EUV lithography from becoming a practical tool.

1.2.5 Electron projection lithography and ion projection lithography

In addition to electromagnetic radiation, beams composed of particles such as electrons or ions can also be used to fabricate nano/micro-structures. Electrons have short de Broglie wavelengths, and resolution finer than 30 nm has been achieved in the electron projection lithography, in which a pre-designed mask is required. However, space-charge effects and heating of the mask still challenge mask manufacturing for electron projection [11]. Ion projection lithography similarly offers a short particle de Broglie wavelength with negligible diffraction. Ion projection mask systems still face the problems of erosion, heating and distortion [12].

1.3 Serial methods

Unlike parallel writing, serial writing produces nano/micro-patterns on a point by point basis, similar to handwriting. This stepwise method is slower, since each individual point in the pattern requires a single exposure. The beam needs to be moved along the entire pattern to create the whole structure. The fabrication of complicated 3D structures with high resolution can benefit from serial writing, and the cost can be reduced as no mask is needed. Electron beam (e-beam) lithography, focused ion beam (FIB) lithography, atomic force microscopy (AFM) lithography, nano imprinting and multiphoton absorption polymerization (MAP) are the serial methods that I will discuss here.

1.3.1 Electron-beam lithography

E-beam lithography makes use of the short de Broglie wavelength of electrons to provide high resolution (< 10 nm). It writes the nano/micro-pattern in a

stepwise manner without use of a mask [13]. Electron backscattering and proximity effects must be taken into account, and the low throughput of e-beam lithography makes it unpractical for large-area patterning. Furthermore, the complicated e-beam system is expensive.

1.3.2 Focused ion beam lithography

Compared with an electron beam, a focused ion beam is subject to much less scattering and is also suitable for writing on metal. The strong absorption of ions on the resist decreases resolution and the strong interaction between the ions and the material makes FIB lithography a better tool for etching than for fabrication [14].

1.3.3 Atomic force microscopy (AFM) lithography

A wide range of materials, such as polymers, biomolecules, metals and semiconductors, are suitable for AFM lithography. Since AFM itself possesses excellent characterization capabilities, nano/micro-structures fabricated in AFM lithography can be charaterized *in situ*. Still, a number of challenges need to be solved for this method, such as the incomplete understanding of its complex physico-chemical mechanism, its sensitivity to the environmental fluctuations and manipulation, and its low throughput [15].

1.3.4 Nano-imprint lithography

In nano-imprint lithography [16], a stamp with the desired pattern is pressed onto a resist film on a solid substrate above the glass transition temperature of the polymer. The simplicity of nano-imprint lithography and its ability to print functional

materials have drawn much attention, but its drawbacks, such as the requirement of a pre-fabricated mask, low throughput, overlay and defects, raise many concerns.

1.4 Multiphoton absorption polymerization

1.4.1 Fundamentals of MAP

Multiphoton absorption polymerization (MAP) is a micro-fabrication technique that can create structures with arbitrary 3-D geometries on a point-by-point basis. MAP is the primary method of fabrication discussed throughout my thesis.

MAP was first reported as a fabrication tool in 1997 by Kawata [17]. Multiphoton absorption, the fundamental concept behind MAP, was first predicted 45 years ago [18]. The multiphoton absorption process involves the simultaneous absorption of *n* photons, the total energy of which is equal to the transition energy from the ground electronic state to an excited electronic state of a molecule. The most popular implementation of this method is degenerate two-photon absorption (2PA) which involves two photons with the same energy. To realize 2PA, the two photons must arrive at the targeted molecule at the same time. The probability for excitation is therefore proportional to the square of the light intensity, so the absorption is localized in the focal region if a focused laser is used for excitation (Figure 1.2) [19]. On the other hand, with one-photon excitation, absorption generally occurs throughout the entire beam, and the beam intensity is attenuated during its propagation through a sample.

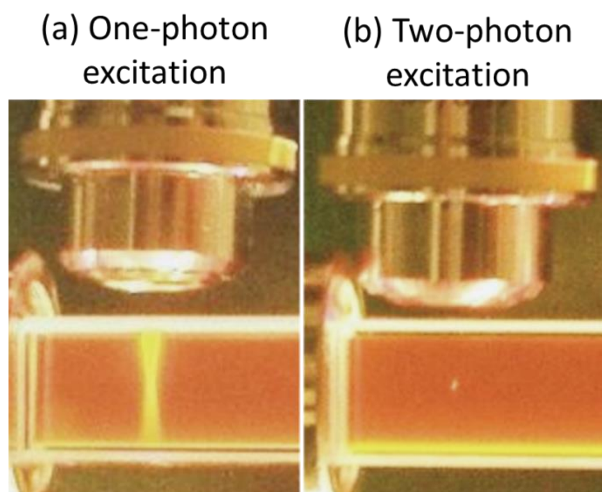

Figure 1.2. Fluorescence in a rhodamine B solution excited by single-photon excitation from a UV lamp (left) and by TPA of a mode-locked Ti:Sapphire laser tuned to 800 nm (right) [19].

The selection rule for the two-photon absorption process is different from that for one-photon absorption in symmetric molecules. In centrosymmetric molecules, for one-photon absorption, allowed transitions require opposite parity between an initial state and final state [28] (from a gerade (g) state to an ungerade (u) state, or vice versa). In the case of two-photon absorption, one photon is absorbed to excite the molecule from its ground state to a virtual intermediate state (which must have the same symmetry as a real state) and a second photon is absorbed immediately after to enable the transition to a higher excited electronic state. Thus, two-photon absorption is only allowed between two states that have the same parity [28] ($g \rightarrow g$ or $u \rightarrow u$). In centrosymmetric molecules, the one-photon-allowed transitions from a given state occur to different states than do the two-photo-allowed transitions. For molecules without an inversion center, transitions can be both one-photon and two-photon allowed.

The process of MAP applies 2PA in a prepolymer resin to fabricate complex structures. By focusing an ultrafast laser beam in the resin, polymerization can be limited to the focal point to create a solid region called a voxel. Voxels are the basic building blocks that are used to build complex 3-D structures by accurate positioning and patterning. Upon polymerization of a particular region of the prepolymer resin, the change of refractive index usually allows real-time monitoring of the fabrication process. Examples of 3D structures created with MAP are shown in Figure 1.3 [20].

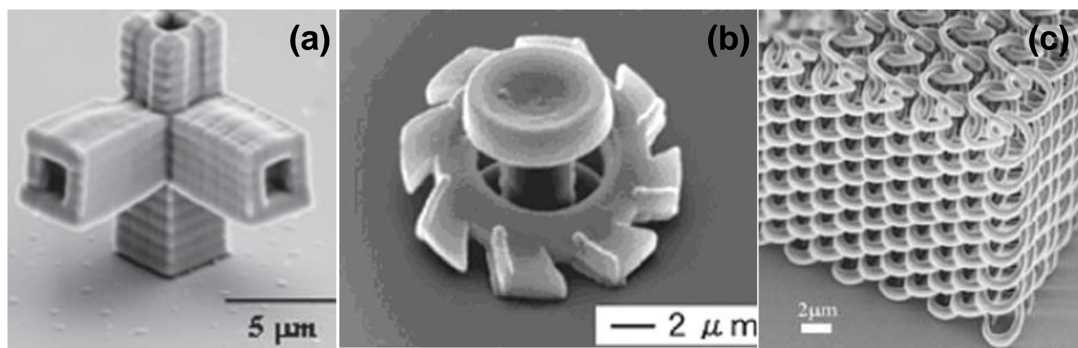

Figure 1.3. (a) A complex set of microchannels fabricated in polydimethylsiloxane (b) a microrotor [26] and (c) a spiral photonic crystal created from SU-8 [20].

Compared with projection lithography, EUV lithography and e-beam writing, MAP can be performed with a simple setup and is relatively inexpensive. Unlike electron and ion projection lithography, MAP is a mask-free process. For arbitrary 3-D structure fabrication, MAP offers advantages over traditional fabrication methods such as X-ray lithography (LIGA), soft lithography, self-assembly and holographic fabrication. These other techniques are usually based on layer-by-layer technology, and it is difficult to create non-periodic, arbitrary 3-D structures. On the other hand, MAP can write any desired 3-D structures on a substrate. Moreover, the MAP process is not sensitive to environmental conditions compared to AFM lithography, and thus MAP has great reproducibility and the fabrication system is easily maintained. MAP's

resolution is related to the laser beam intensity, the composition of the photoresist, the objective lens and the fabrication velocity. 100-nm resolution can be easily attained in MAP. Recent work in our group has demonstrated that MAP resolution of 40 nm using a technique called resolution augmentation through photo-induced deactivation (RAPID) [21].

1.4.2 Experimental setup of MAP

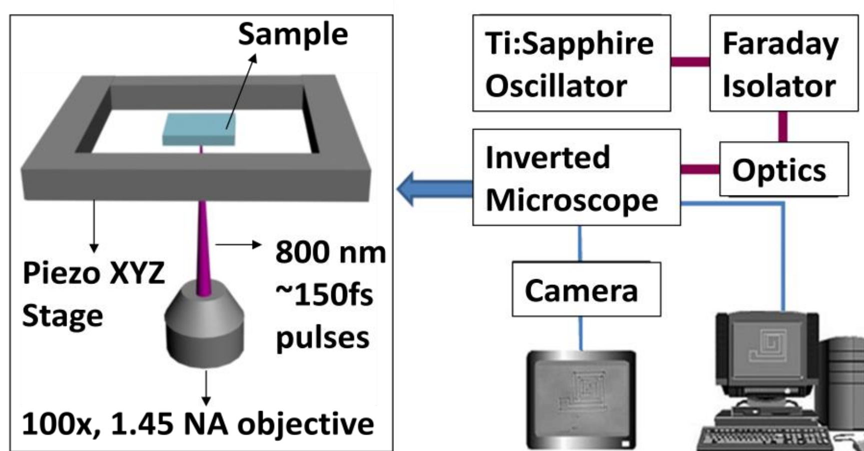

Figure 1.4. Schematic diagram of the sample setup and the laser beam path. For MAP, 800-nm, 150-fs laser pulses are sent into an inverted microscope after passing through a Faraday isolator and other optics. The laser is focused into the sample using a 100×, oil-immersion objective. The movement of the sample stage is controlled by a LabVIEW (National Instruments) program and fabrication is monitored using a CCD camera.

Our tunable excitation source is a Ti:Sapphire oscillator (Coherent Mira 900-F) that produces 150-fs pulses. A Faraday isolator is used to prevent back reflections or other radiation from entering the cavity, in order to protect the oscillator. The laser intensity is controlled by sending the beam through a polarizer after a half-wave plate.

The beam is then focused inside the sample by a 100×, 1.45 NA, oil-immersion objective. The sample is mounted on a piezoelectric stage on an inverted microscope. The stage movement is controlled by the LabVIEW program. The movement of the sample relative to the laser beam creates patterns inside the sample. The fabrication of a pre-designed pattern can be monitored in real time using a CCD camera. Different sample preparation methods, which vary based on the requirements of the specific applications, will be discussed in later chapters.

1.5 The improvements and applications of MAP

1.5.1 High-speed MAP and fabrication of microfluidic devices

Like any other method, MAP has its own shortcomings. One issue with MAP that needs to be addressed is the fabrication speed. Due to the typical fabrication speed (10-20 μm/s), MAP is only suitable for fabricating structures over distances of up to hundreds of micrometers. To extend MAP's application to large-scale devices, previous work from our group has reported high-speed MAP, which has been used to fabricate the master structures of large-area microfluidic devices [22].

As shown in Figure 1.5(a), a mold of the master structure is composed of two channels with different cross sections, the "V" shape channel in Figure 1.5(b) and the rectangular channel with large aspect ratio in Figure 1.5(c). Centimeter-scale microfluidic devices with arbitrary cross sections can be realized using MAP and channels with different shapes of cross sections are readily integrated in a single device.

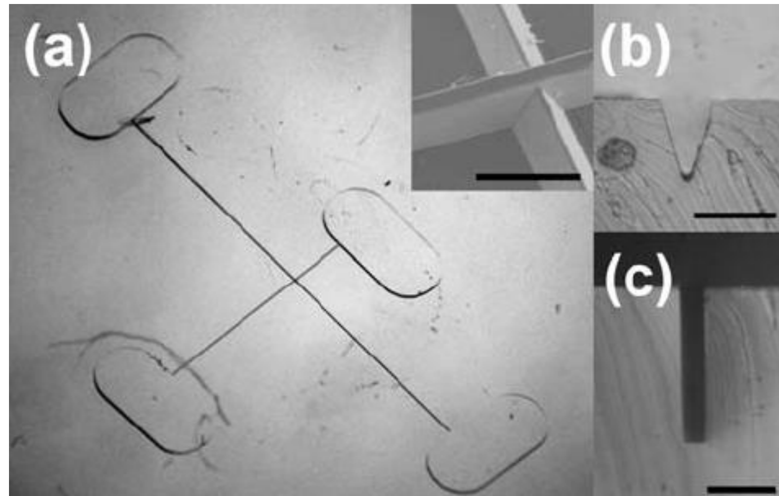

Figure 1.5 (a) An optical image of the PDMS mold of the master structure for a microfluidic device. The inset shows a scanning electron micrograph (SEM) of the intersection region of the walls (the scale bar is 100 μm). (b) and (c) Optical images of cross-sections of the two different channels in this device; the scale bars are each 50 μm. [22]

1.5.2 MAP and MA-μTM

To further improve MAP's throughput, molding has been employed. If MAP is only used to fabricate a master structure that can be replicated using another lithographic method, such as nano-imprinting, the throughput can be dramatically improved. A major advantage of MAP is its ability to build up complicated 3D structures that can contain closed loops. Traditional molding processes are not capable of single-step replication of closed-loop designs except by a layer-by-layer approach. Thus, the membrane-assisted microtransfer molding (MA-μTM) method was created [23]. As illustrated in Figure 1.6, in the molding step, a thin membrane inside the closed loop creates an opening in the mold that can easily be released from the replica without damage to the closed loop. MA-μTM can solve the topological restrictions that are typical in molding.

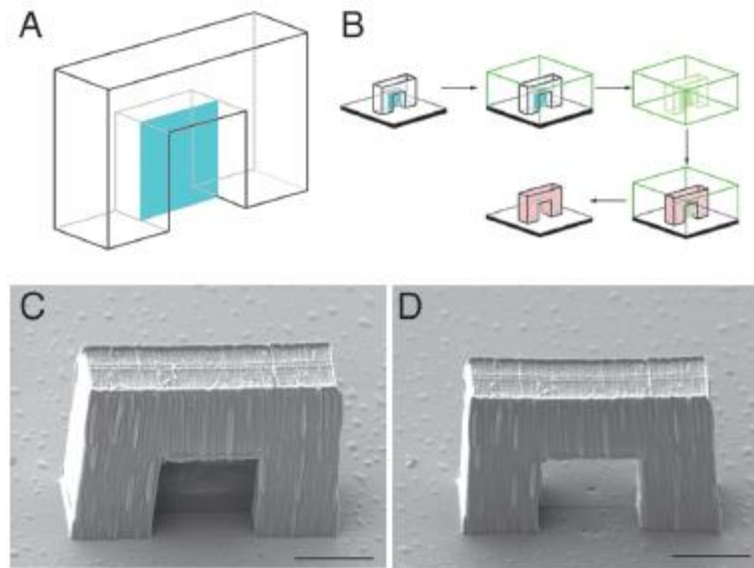

Figure 1.6. Replication of a master structure that has a closed loop. (a) Schematic diagram of a master structure for the creation of an arch. The blue plane is the membrane. (b) Procedure for MA-μTM of an arch. The master structure of an arch made using MAP is immersed in PDMS. After curing, the mold is peeled off of the substrate. The mold is filled with a molding material and pressed against a substrate. After curing of the molding material, the mold is removed, leaving a daughter arch without the membrane. (c) SEM of a master structure for an arch. (d) The corresponding daughter structure. (The scale bars are 10 μm.) [23]

1.5.3 MAP-fabricated microring resonators

High quality polymeric microring resonator fabrication using MAP was also demonstrated in previous work from our group [24]. The properties and applications of resonators will be discussed in Chapter 2. In Figure 1.7, acrylic micro-sized resonators fabricated in this manner show extinction of up to -22 dB with a finesse (the ratio of separation between neighboring resonances to the width of transmission band pass) as high as 15. However, the free spectral range (*FSR*) (the separation

between neighboring resonances) still requires improvement. Two approaches, using a smaller radius of curvature and creating serial coupled resonators, come to mind. Decreasing the radius introduces considerable bending loss, however. Serial coupled resonators have been investigated and have proven to provide a *FSR* as wide as 33 nm. The details will be given in Chapter 2.

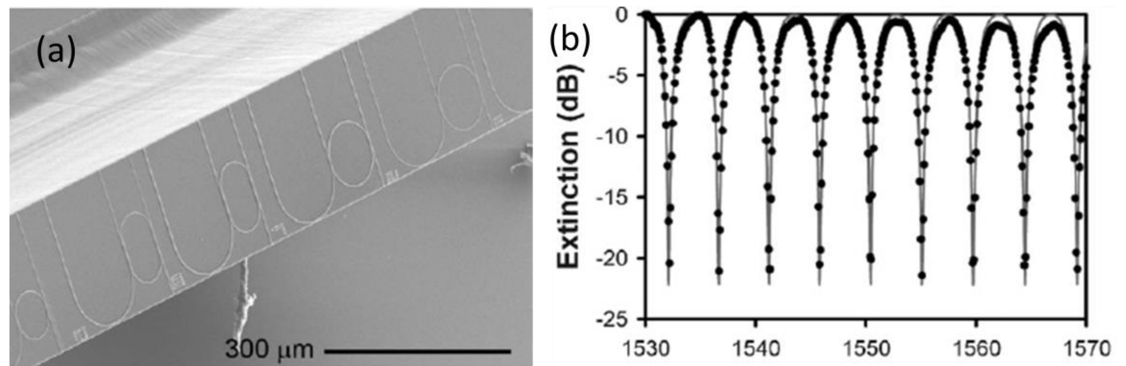

Figure 1.7. (a) SEM image of a set of "IOU" microring resonator structures with different ring designs on top of a PDMS ridge. (b) Experimental through-port spectrum (symbols) and fit (line) for a device with a 50 μm radius of curvature and a 10 μm coupling region. [24]

When these on-chip devices are integrated with fibers, 2-3 dB insertion loss will be introduced at each junction between a fiber and a waveguide. To reduce this insertion loss, resonator-based, in-line, side-polished fiber (SPF) devices were designed and created. These devices were further used to map the polished surface of an SPF and to sense pressure. I will discuss these integrated SPF devices in Chapter 3.

1.5.4 MAP-fabricated movable structures

In addition to stationary microstructures, movable devices such as microrotors (Figure 1.8) [25] and micropumps [26] have been created using MAP. These devices can be optically driven or manipulated in an aqueous environment. In this two-step method, it is necessary to wash away the resin after fabrication and then to fill the system with water for manipulation, because most of the resins are too viscous to carry out optical manipulation. Moreover, in most cases the movable parts are installed in a microfluidic device or used in a bio-compatible system. Therefore, the hydrophobic and toxic resin needs to be removed in advance. However, adhesion often occurs in this solvent-change process, causing the microstructures to fail to function. To simplify the procedure and prevent stiction, an aqueous photoresist suitable for MAP was developed and used to fabricate patterns composed of acrylic polymers or biomaterials, such as bovine serum albumin (BSA). Through the combination of MAP and optical tweezers (OTs), we successfully realized the fabrication and manipulation in one pot without changing the solvent [27]. Complicated microstructures containing glass beads, which are difficult to realize using traditional fabrication methods, were also created using MAP and OTs, as demonstrated in Chapter 4.

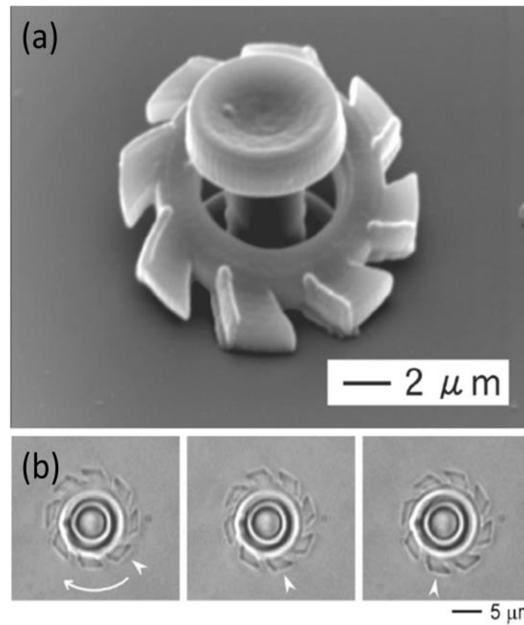

Figure 1.8. (a) SEM image of a microturbine fabricated by 3-D direct laser writing; (b) Sequential optical micrographs of a rotating microturbine observed at time intervals of one second. A wing of the microturbine, marked with an arrow in each photo, was optically trapped and rotated clockwise by the circular scanning of a focused laser beam. [26]

In Chapter 5, I will discuss how to achieve nanograss-like features on MAP-fabricated polymer films. The superhydrophobic nature of these films will be discussed.

References

[1] Z.-S. Wang, H. Kawauchi, T. Kashima, and H. Arakawa, "Significant influence of TiO2 photoelectrode morphology on the energy conversion efficiency of N719 dye-sensitized solar cell," *Coord. Chem. Rev.*, vol. 248, pp. 1381–1389, 2004.

[2] A. W. Martinez, S. T. Phillips, G. M. Whitesides, and E. Carrilho, "Diagnostics for the developing world: microfluidic paper-based analytical devices," *Anal. Chem.*, vol. 82, pp. 3–10, 2010.

[3] M. E. Motamedi, T. Oaks, M. C. Wu, L. Angeles, and K. S. J. Pister, "Micro-opto-electro-mechanical devices and on-chip optical processing," *Opt. Eng.*, vol. 36, pp. 1282–1297, 1997.

[4] M. V Schneider, "Contact lithography," U.S. Patent US39363011976.

[5] H. Lorenz, M. Despont, N. Fahrni, J. Brugger, P. Vettiger, and P. Renaud, "High-aspect-ratio, ultrathick, negative-tone near-UV photoresist and its applications for MEMS," *Sensor. Actuat. A*, vol. 64, pp. 33–39, 1998.

[6] J. Appelbaum, N. Plainfield, M. Feldman, and M. Hill, "Proximity lithography," U.S. Patent US40266531975.

[7] H. Kawata, J. M. Carter, A. Yen, and H. I. Smith, "Optical projection lithography using lenses with numerical apertures greater than unity," *Microelectron. Eng.*, vol. 9, pp. 31–36, 1989.

[8] J. D. Buckley, "Step-and-scan lithography using reduction optics," *J. Vac. Sci. Technol. B*, vol. 7, pp. 1607–1612, 1989.

[9] J. E. Bjorkholm, “EUV lithography — The successor to optical lithography,” *Intel Technol. J.*, pp. 1–8, 1998.

[10] A. Heuberger, “X-ray lithography,” *Microelectron. Eng.*, vol. 5, pp. 3–38, 1986.

[11] L. R. Harriott, B. Laboratories, L. Technologies, and M. Hill, “Scalpel : Projection electron beam lithography,” *Proc. 1999 Part. Accelerator Conf.*, pp. 595–599, 1999.

[12] A. A Tseng, “Recent developments in nanofabrication using ion projection lithography,” *Small*, vol. 1, pp. 594–608, 2005.

[13] C. Vieu, F. Carcenac, A. Pepin, Y. Chen, M. Mejias, A. Lebib, L. Couraud, and H. Launois, “Electron beam lithography : Resolution limits and applications,” *Appl. Surf. Sci.*, vol. 164, pp. 111–117, 2000.

[14] J. Melngailis, “Focused ion beam lithography,” *Nucl. Instrum. Meth. B*, vol. 80–81, pp. 1271–1280, 1993.

[15] X. N. Xie, H. J. Chung, C. H. Sow, and A. T. S. Wee, “Nanoscale materials patterning and engineering by atomic force microscopy nanolithography,” *Mater. Sci. Eng. R*, vol. 54, pp. 1–48, 2006.

[16] H. Search, C. Journals, A. Contact, M. Iopscience, and I. P. Address, “Nanoimprint lithography : Challenges and prospects,” *Nanotechnology*, vol. 91, pp. 91–95, 2001.

[17] S. Maruo, O. Nakamura, and S. Kawata, “Three-dimensional microfabrication with two-photon-absorbed photopolymerization,” *Opt. Lett.*, vol. 22, pp. 132–134, 1997.

[18] Y.-H. Pao and P. M. Rentzepis, "Multiphoton absorption and optical-harmonic generation in highly absorbing molecular crystals," *J. Chem. Phys.*, vol. 43, pp. 1281–1286, 1965.

[19] C. N. LaFratta, J. T. Fourkas, T. Baldacchini, and R. a Farrer, "Multiphoton fabrication," *Angew. Chem. Int. Ed.*, vol. 46, pp. 6238–58, 2007.

[20] L. Li and J. T. Fourkas, "Multiphoton polymerization," *Mater. Today*, vol. 10, pp. 30–37, 2007.

[21] L. Li, R. R. Gattass, E. Gershgoren, H. Hwang, and J. T. Fourkas, "Achieving lambda/20 resolution by one-color initiation and deactivation of polymerization," *Science*, vol. 324, pp. 910–913, 2009.

[22] G. Kumi, C. O. Yanez, K. D. Belfield, and J. T. Fourkas, "High-speed multiphoton absorption polymerization: fabrication of microfluidic channels with arbitrary cross-sections and high aspect ratios," *Lab Chip*, vol. 10, pp. 1057–1060, 2010.

[23] C. N. LaFratta, L. Li, and J. T. Fourkas, "Soft-lithographic replication of 3D microstructures with closed loops," *Proc. Nat. Acad. Sci. U.S.A.*, vol. 103, pp. 8589–8594, 2006.

[24] L. Li, E. Gershgoren, G. Kumi, W.-Y. Chen, P.-T. Ho, W. N. Herman, and J. T. Fourkas, "High-performance microring resonators fabricated with multiphoton absorption polymerization," *Adv. Mater.*, vol. 20, pp. 3668–3671, 2008.

[25] S. Maruo, K. Ikuta, and H. Korogi, "Force-controllable, optically driven micromachines fabricated by single-step two-photon," *J. Microelectromech. Syst.*, vol. 12, pp. 533–539, 2003.

[26] T. Umversrty, A. Aoba, and A. Aobaku, "Micropump and sample-injector for integrated chemical analyzing systems," *Sensor. Actuat. A*, vol. 23, pp. 189–192, 1990.

[27] F. Dawood, S. Qin, L. Li, E. Y. Lin, and J. T. Fourkas, "Simultaneous microscale optical manipulation, fabrication and immobilisation in aqueous media," *Chem. Sci.*, vol. 3, pp. 2449–2456, 2012.

[28] K. D. Bonin and T. J. Mcllrath, "Two-photon electric-dipole selection rules," *J. Opt. Soc. Am. B*, vol. 1, pp. 52-55, 1984

Chapter 2: MAP-Fabricated Double-Ring Resonators

2.1 Introduction

2.1.1 Microring resonators

Since 1980, optical communication systems have been deployed worldwide. The change from electronic to optical networks has been driven by the numerous advantages of optical hardware, such as high bandwidth, low signal attenuation and ultra-low crosstalk. However, the implementation of *all-optical systems*, which would allow even higher bandwidths and processing speeds than current systems, has been prevented by the lack of the optical components (e.g., routers and filters) necessary for such an advanced network. Recently, microring resonators have been shown to be promising candidates for various elements of photonic systems such as filters, switches, and spectroscopic devices [1-4]. In addition, these resonators have also been used in biochemical/mechanical sensors and light-matter coupling [5-6].

In 1971, Weber and Ulrich [7] demonstrated the first optical ring resonator. Over the next 20 years, many research groups have further explored the field of optical resonators. Improvements included expanding to ring resonators with different materials such as polymers [8-9], semiconductors [10-11], and doped/undoped silica-based glasses [12-15]. However, the sizes of the resonators mentioned above were too large (in millimeters or greater) to be appropriate for *all-optical* signal processing systems or lab-on-a-chip designs. Moreover, the dimensions of resonators should be

on the order of the wavelength of interest to achieve reasonable finesse (see section 2.2.2) and quality for modern optical communications systems [16]. To use wavelengths on the order of micrometers, there has been an increased interest in the field of microresonators. Polymer-based microresonators [17], planar disc ring resonators [18], microtoroids [19], and fiber microring resonators [4, 20] (shown in Figure 2.1) are representative examples of microresonators.

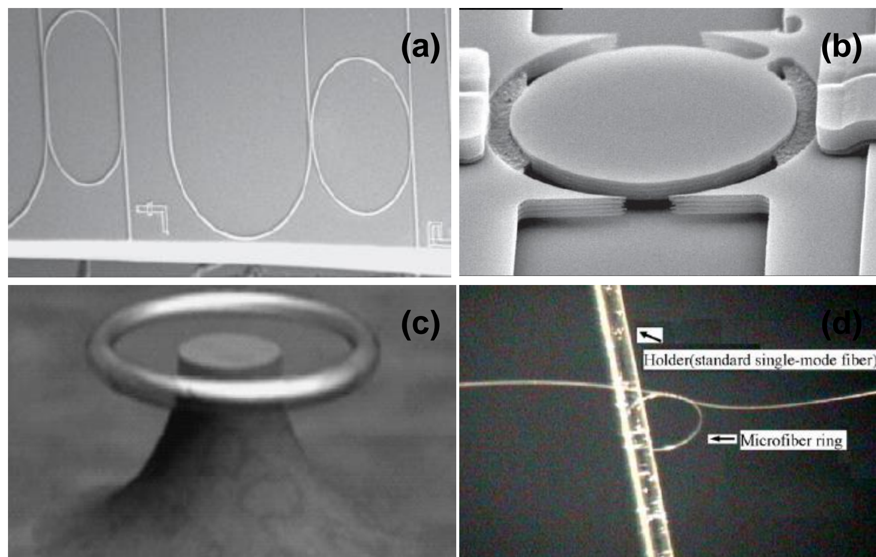

Figure 2.1. Examples of microresonators. (a) Polymer-based resonators, (b) planar disc ring resonators, (c) microtoroid and (d) fiber microring resonators. [17-20]

2.1.2 Double-ring resonators

Multiple resonators or cascaded resonators are often designed to achieve desired performance, such as for multiplexed or high-sensitivity sensors [21], multi-bit delay lines [22], slow-wave devices, and band filters [23]. Based on the Vernier effect [24], double-ring resonators (DRRs) can be used to increase free spectral range (*FSR*) for applications in filters [25], lasers [26], modulators and dense wavelength division multiplexing (DWDM) [27]. As shown in Figure 2.2, DRRs have a simple structure and provide a large tuning range.

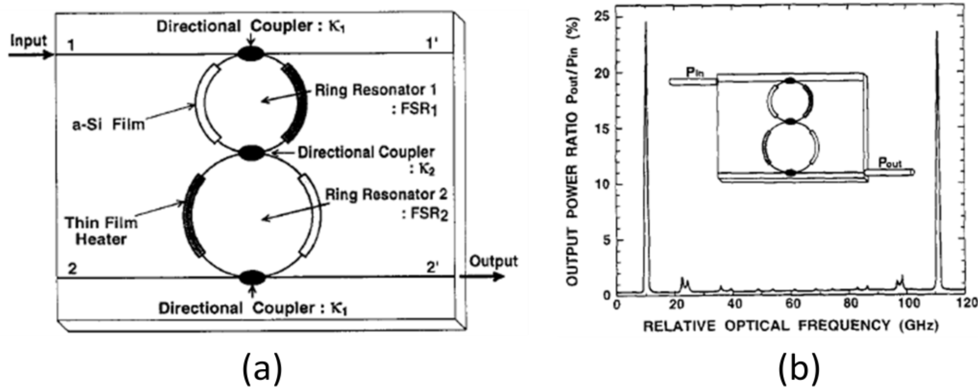

Figure 2.2 (a) Configuration of an integrated, optical double-ring resonator. (b) Measured optical frequency response of a double-ring resonator module [28].

To achieve a high rejection between the pass band and stop bands (see section 2.2.3), appropriate parameters, and especially the coupling coefficients of the directional couplers, should be designed and fabricated with precision [15]. The fabrication tolerance of traditional lithography makes it difficult to realize nanometric precision for both the radius and the gap size of microring resonators independently without thermo-optical or electro-optical frequency tuning [29]. Here, multiphoton absorption polymerization (MAP) is used for the one-step fabrication of passive, acrylic DRRs with large *FSR* and high quality. Moreover, the fabrication of DRRs using MAP is rapid, simple, and amenable to a wide variety of designs.

In this chapter, I discuss the fundamental principles of single and double-ring resonators. Fabrication of single-mode DRRs using MAP and subsequent characterization are demonstrated. The design of waveguides with a pedestal cross-section and thermal reflow of these devices are also discussed as means of improving the performance of DRRs.

2.2 Fundamentals of microring resonators

2.2.1 Definitions

A waveguide, which has a higher refractive index than the materials that surround it, guides light via total internal reflection [31]. Field distributions that do not change during propagation are called waveguide modes. A large refractive index contrast between a waveguide and its surroundings gives better mode confinement and may allow higher-order modes to exist. On the other hand, the number of modes decreases when the refractive index contrast or the waveguide dimensions are reduced. Optical, single-mode fibers are one good example of a single-mode waveguide operating with a core size of about 10 micrometers.

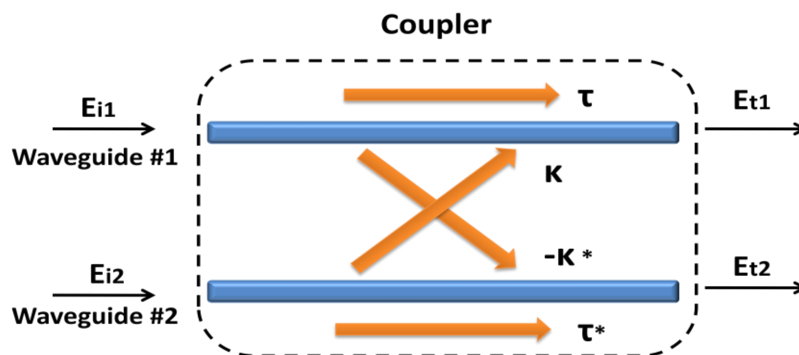

Figure 2.3. Schematic of a waveguide coupler. The device consists of two waveguides, #1 and #2. The orange arrows indicate the direction of the radiation propagation inside and between the waveguides.

If two waveguides are brought close enough to one another, power exchange will occur between their optical modes. This process is known as mode coupling [32]. As shown in Figure 2.3, when two waveguides with the same cross section and same refractive index are coupled to each other, mode exchange takes place between them.

Given a coupler that is lossless and symmetric, the electric fields of the incident and transmitted waves satisfy the transfer-matrix equation [35]

$$\begin{bmatrix} E_{t1} \\ E_{t2} \end{bmatrix} = \begin{bmatrix} \tau & \kappa \\ -\kappa^* & \tau^* \end{bmatrix} \begin{bmatrix} E_{i1} \\ E_{i2} \end{bmatrix}, \tag{2.1}$$

where the κ and τ are coupling and transmission coefficients, respectively. Asterisks denote a complex conjugate. When the phase-matching condition is met, τ and κ are equal to their complex conjugates. For a lossless and symmetric coupler, we have

$$|\tau|^2 + |\kappa|^2 = 1. \tag{2.2}$$

2.2.2 Microring resonators [8, 29]

Figure 2.4 is a schematic of a microring resonator. Multiple wavelengths of light can be introduced at the input of the upper straight waveguide (the "bus"). Radiation with wavelengths λ_i that satisfy the resonance condition will be coupled strongly into the resonator. The coupling of all the other wavelengths will be suppressed. Theoretically, only the resonant wavelengths should be detected at the drop port terminal, and the remaining wavelengths will be detected at the through port. The resonance condition is satisfied when an integer multiple of wavelength λ_i equals to the total optical length of the resonator. This condition is written as

$$n_{eff}L = m\lambda_i, \tag{2.3}$$

where n_{eff} is the effective index of the microring, L is the total round-trip length of the microring, and m is any positive integer.

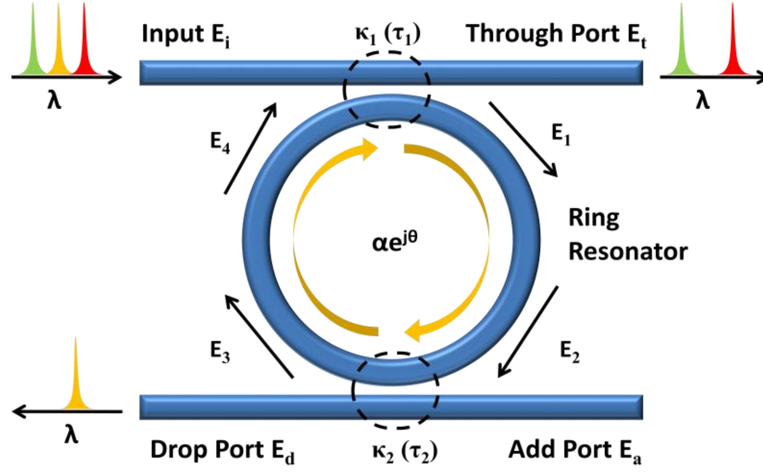

Figure 2.4. Schematic of a single microring resonator.

Ignoring the coupling between the microring resonator and the straight waveguide, after one round trip inside the ring, E_4 and E_1 in Figure 2.4 satisfy the equation

$$E_4 = \alpha \cdot e^{j\theta} E_1, \tag{2.4}$$

where j is the imaginary unit and α is the round-trip transmission coefficient of the ring; if the ring is lossless, α = 1. The phase difference is θ = ωL/c, c is the phase velocity of the ring mode ($c = c_0/n_{eff}$) and the fixed angular frequency $\omega = kc_0$, where c_0 refers to the speed of light in vacuum. The vacuum wavenumber k is 2π/λ. The circumference of the microring is L = 2πR, where R is the radius of the ring measured from the center of the ring to the center of the waveguide. By using the vacuum wavenumber, the effective refractive index n_{eff} can be introduced into the ring-coupling relations via

$$\theta = \frac{\omega L}{c} = \frac{kc_0 L}{c} = k \cdot n_{eff} \cdot L = \frac{2\pi n_{eff} L}{\lambda}. \tag{2.5}$$

If there is coupling between the resonator and the buses, we need to consider the half round trip of the radiation inside the resonator instead of an entire round trip, and we obtain

$$E_2 = \sqrt{\alpha \cdot e^{j\theta}} E_1 \tag{2.6}$$

and

$$E_4 = \sqrt{\alpha \cdot e^{j\theta}} E_3. \tag{2.7}$$

As illustrated in Figure 2.4, there are two couplers that can have different coupling coefficients. Let us assume that the couplers are lossless and symmetric. According to the matrix-transfer equation (2.1), we will have

$$\begin{bmatrix} E_t \\ E_1 \end{bmatrix} = \begin{bmatrix} \tau_1 & \kappa_1 \\ -\kappa_1{}^* & \tau_1{}^* \end{bmatrix} \begin{bmatrix} E_i \\ E_4 \end{bmatrix} \tag{2.8}$$

and

$$\begin{bmatrix} E_3 \\ E_d \end{bmatrix} = \begin{bmatrix} \tau_2 & \kappa_2 \\ -\kappa_2{}^* & \tau_2{}^* \end{bmatrix} \begin{bmatrix} E_2 \\ E_a \end{bmatrix}. \tag{2.9}$$

To simplify the calculation, we assume that there is no incident radiation at the add port. Thus,

$$E_a = 0. \tag{2.10}$$

We can then combine equations (2.6)-(2.10) to obtain an expression for the electric field at the through and drop ports as

$$E_t = \frac{\tau_1 - \tau_2 \alpha e^{j\theta}}{1 - \tau_1 \tau_2 \alpha e^{j\theta}} E_i \tag{2.11}$$

and

$$E_d = \frac{\kappa_1 \kappa_2 \sqrt{\alpha e^{j\theta}}}{1 - \tau_1 \tau_2 \alpha e^{j\theta}} E_i, \tag{2.12}$$

The respectively corresponding intensities are given by $|E|^2$.

We now discuss some important parameters that are often used to evaluate the performance of the resonators. Free spectral range (*FSR*) is defined as the separation between neighboring resonance frequencies. This separation is given by

$$FSR = \Delta\lambda \approx \frac{\lambda^2}{n_{eff}L}\,. \tag{2.13}$$

Because *FSR* is inversely proportional to the size of the microring resonator, smaller resonators give higher *FSR*s. Similarly, a smaller refractive index yields a larger *FSR*. When the resonator has a larger *FSR*, the resonances are more separated.

The finesse, *F*, is an important indicator of the resolution of a resonator. *F* is defined as the ratio of the *FSR* to the width of transmission band pass (see Figure 2.5). The finesse is given by

$$F = \frac{FSR}{FWHM} = \frac{\Delta\lambda}{\Delta\lambda_{FWHM}}. \tag{2.14}$$

Here, $\Delta\lambda_{\text{FWHM}}$ is the full width at half maximum of the resonance peak. Sharp resonance peaks and a large *FSR* work together to give a high finesse.

The finesse of a resonant cavity is related to another significant characteristic, the quality factor *Q*. *Q* is a measure of the energy storage capability of a resonator. *Q* is defined as the ratio of the wavelength to $\Delta\lambda_{\text{FWHM}}$:

$$Q = \frac{\lambda}{\Delta\lambda_{FWHM}}. \tag{2.15}$$

Shown in Figure 2.5 are two drop-port spectra that have the same *FSR* but different finesses. The larger finesse (red) gives sharper peaks with better separation. F is dependent on both the internal loss coefficient α and the coupling coefficient κ (that is, the external loss) of a resonator. The higher the total loss of a resonator, the lower its finesse. The internal loss includes radiation by non-perfect reflections at the boundaries, and absorption and scattering in the resonator medium. As a result, internal loss should be minimized to achieve high *F* and *Q*.

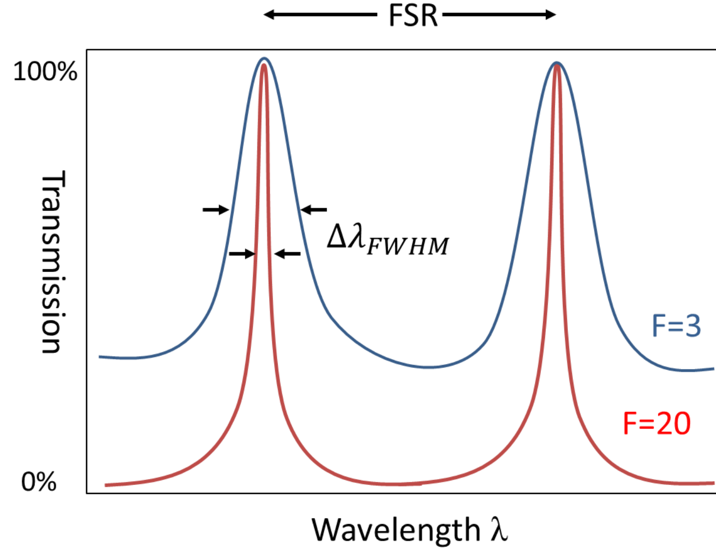

Figure 2.5. Transmission characteristics of a resonator. *FSR* is the free spectral range, $\Delta\lambda_{FWHM}$ is full width at half maximum, and $F=FSR/\Delta\lambda_{FWHM}$. A larger finesse implies a better separation of resonance frequencies.

2.2.3 Double-ring resonators [15]

In our case, a DRR device is composed of two straight waveguides and two resonators, one with radius R_1 and one with radius R_2. If $R_1 \neq R_2$, the two resonators have different sets of resonance wavelengths. Only the shared resonance wavelengths can be detected at the drop port. Thus, resonances exist when

$$N \cdot FSR_1 = M \cdot FSR_2, \tag{2.16}$$

where the M and N are integers and FSR_1 and FSR_2 are the free spectral ranges of the two resonators. This result implies that the overall *FSR* is

$$FSR = |M-N| \frac{FSR_1 \cdot FSR_2}{|FSR_1 - FSR_2|}. \tag{2.17}$$

For instance, if two resonators with *FSR*s of 5 nm and 6 nm are chosen to create a DRR device, this device will have an *FSR* of 30 nm.

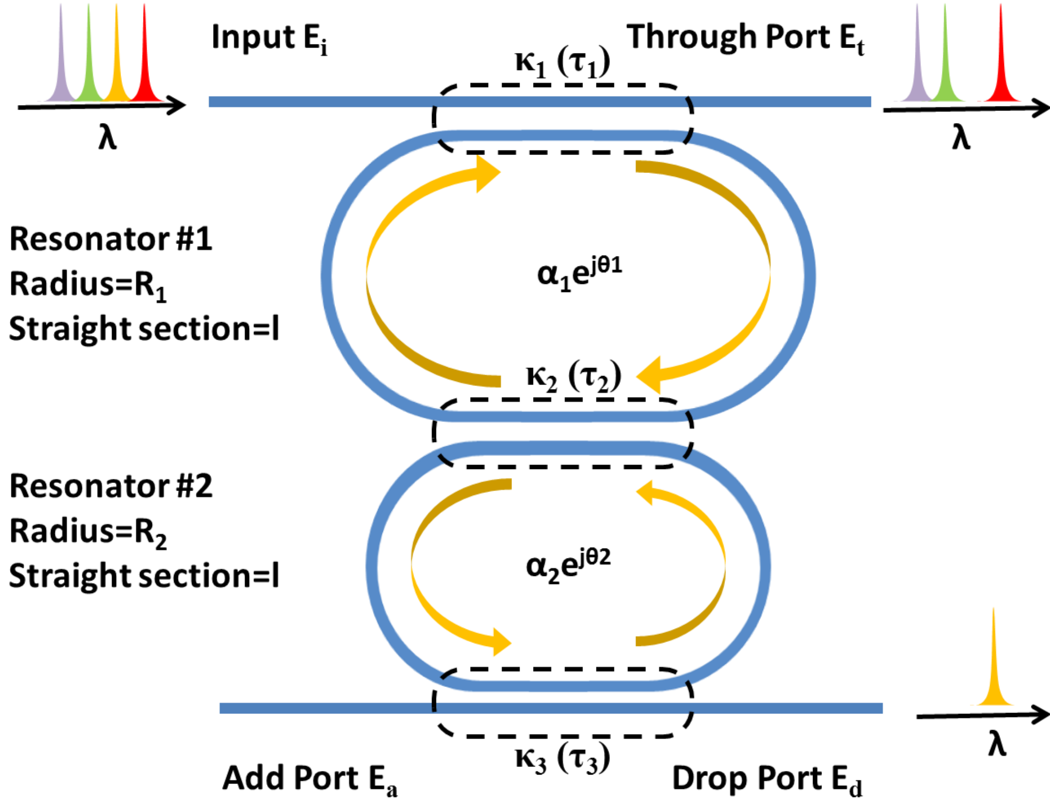

Figure 2.6. Schematic of a DRR device. The first resonator has a radius of R_1 and a straight section of length l. The second resonator has a radius of R_2 and straight coupling region of length l. κ_1 and τ_1 represent the coupling and transmission coefficients between the first bus and the first resonator, κ_2 and τ_2 are the coefficients for the coupling between the two resonators, and κ_3 and τ_3 indicate the coefficients of coupler between the second resonator and second bus.

Figure 2.6 shows a schematic diagram of a DRR device. All of the couplers are assumed to be lossless and symmetric and there is no input at the add port. The through-port and drop-port electric fields, as derived using matrix-transfer method, are given by

$$E_t = \frac{\alpha_1 e^{j\theta_1}(\tau_3\alpha_2 e^{j\theta_2} - \tau_2) + \tau_1(1 - \tau_3\tau_2\alpha_2 e^{j\theta_2})}{1 - \tau_3\tau_2\alpha_2 e^{j\theta_2} - \tau_2\tau_1\alpha_1 e^{j\theta_1} + \tau_3\tau_1\alpha_1\alpha_2 e^{j\theta_1} e^{j\theta_2}} E_i \quad (2.18)$$

and

$$E_d = \frac{\kappa_1 \kappa_2 \kappa_3 \sqrt{\alpha_1 \alpha_2 e^{j\theta_1} e^{j\theta_2}}}{1 - \tau_3 \tau_2 \alpha_2 e^{j\theta_2} - \tau_2 \tau_1 \alpha_1 e^{j\theta_1} + \tau_3 \tau_1 \alpha_1 \alpha_2 e^{j\theta_1} e^{j\theta_2}} E_i \quad (2.19)$$

To increase the chance of coupling between the straight bus and the ring resonator, a straight section was added in the resonator. This design is called a racetrack resonator.

A typical drop-port spectrum of a DRR device is shown in Figure 2.7. The pass bands are the common resonances of the two resonators, while the other resonances are called the stop band. The *FSR* is equal to the separation between adjacent pass bands. The intensity difference between the pass bands and the stop band is the isolation. A large isolation is usually desired.

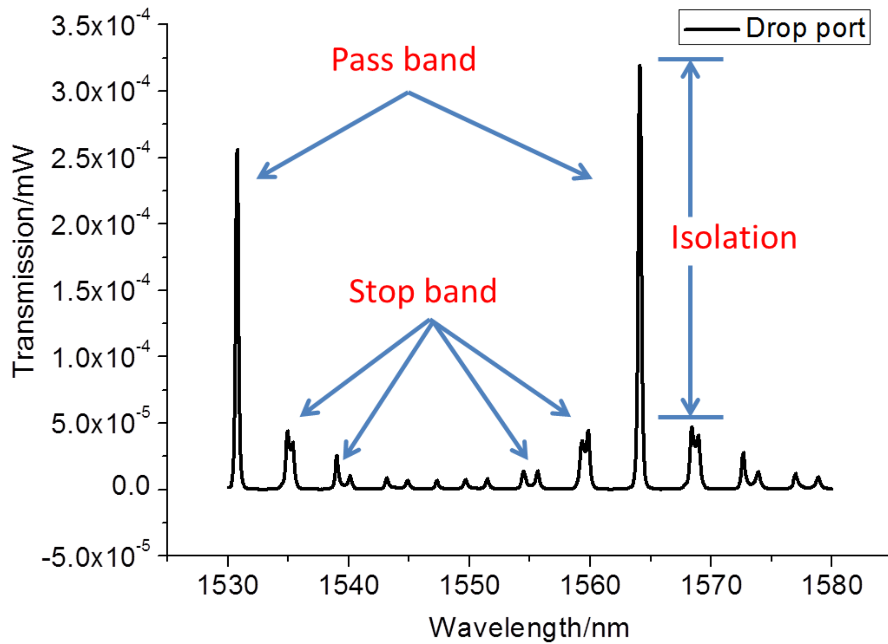

Figure 2.7. A typical drop-port spectrum of a DRR device.

2.3 Experiments and data analysis

2.3.1 Sample preparation

The resonators were fabricated on a 200-μm-wide polydimethylsiloxane (PDMS) ridge to enable the through-port and drop-port measurements. Moreover, PDMS has a refractive index of 1.41, which makes it a good bottom cladding layer for the waveguides. To prepare the PDMS substrate, Sylgard 184 (Dow Corning) prepolymer was mixed with curing agent in a 10:1 mass ratio. The mixture was stirred and then centrifuged to remove air bubbles. One drop of the PDMS was sandwiched with a 200-μm spacer between oxygen-plasma-cleaned glass cover slip and a pretreated silicon wafer. The plasma-cleaned cover slip provides good adhesion to the PDMS. The silicon wafer was treated in an evacuated desiccator using (tridecafluoro-1,1,2,2-tetra-hydrooctyl)dimethylchlorosilane overnight to prevent the PDMS film from sticking. After baking in the oven at 100 ℃ for 30 min, the PDMS film together with the glass slip was peeled off from the silicon wafer. To improve the adhesion of acrylic polymer on PDMS, the PDMS substrate was treated with oxygen plasma for 3 min and then immersed in an ethanol solution containing 2 vol% (3-acryloxypropyl)trimethoxysilane and 5 vol% deionized water overnight. PDMS substrate was then rinsed with ethanol and baked at 100 ℃ for one hour. A razor blade mounted on a micrometer was used to cut a 200-μm-wide ridge in the PDMS. This ridge served as the bottom cladding for the waveguides [17].

The acrylic resin, whose refractive index is 1.49, was composed of 54 wt% dipentaerythritol pentaacrylate (Sartomer) and 43 wt% tris (2-hydroxy ethyl) isocyanurate triacrylate (Sartomer), with 3 wt% Lucirin TPO-L (BASF) as the photoinitiator [6]. One drop of acrylic resin was added on the PDMS ridge and the

sample was covered by a No. 0 glass cover slip (Corning) with a 40-μm spacer (Figure 2.8).

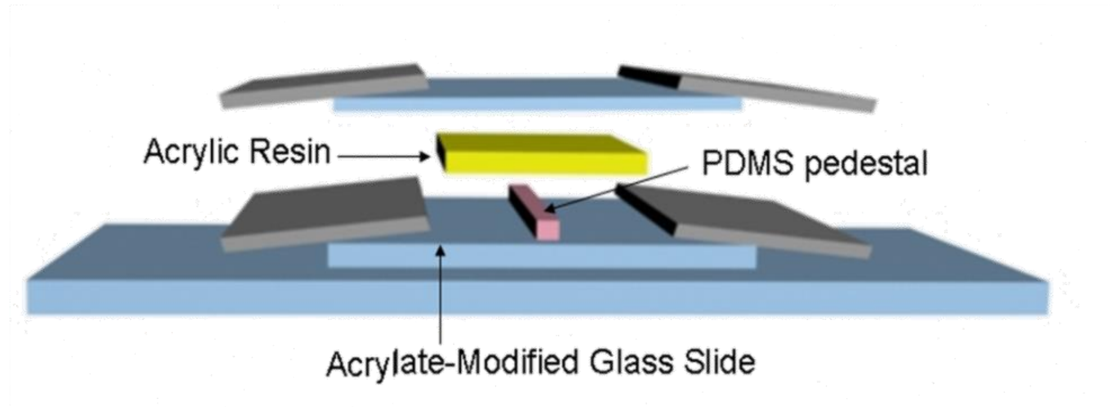

Figure 2.8. Scheme for sample preparation.

The setup for MAP was introduced in Chapter 1. An 800-nm ultrafast laser is used to excite the photoinitiator in the acrylic resin by two-photon absorption using a 100X, 1.45 NA, oil-immersion objective. The sample is moved in three dimensions using a piezoelectric stage controlled by LabView software, while the laser beam focus is fixed in space.

2.3.2 Serial double-ring resonators

For the DRRs, the contrast between the pass band and the stop band (isolation) is highly sensitive to the coupling coefficients. The coupling coefficients depend on the waveguide cross sections, the coupling lengths and the coupling gaps. We have successfully established the dependence of the coefficients on the gap sizes by varying the gap sizes and keeping the waveguide dimensions unchanged. As shown in Figure 2.9, acrylic couplers with different gap sizes were fabricated using MAP. The coupling/transmission coefficients of these couplers are plotted in the Figure 2.10.

According to the simulation results, appropriate gaps and ring sizes can be chosen to give the DRRs desired performance.

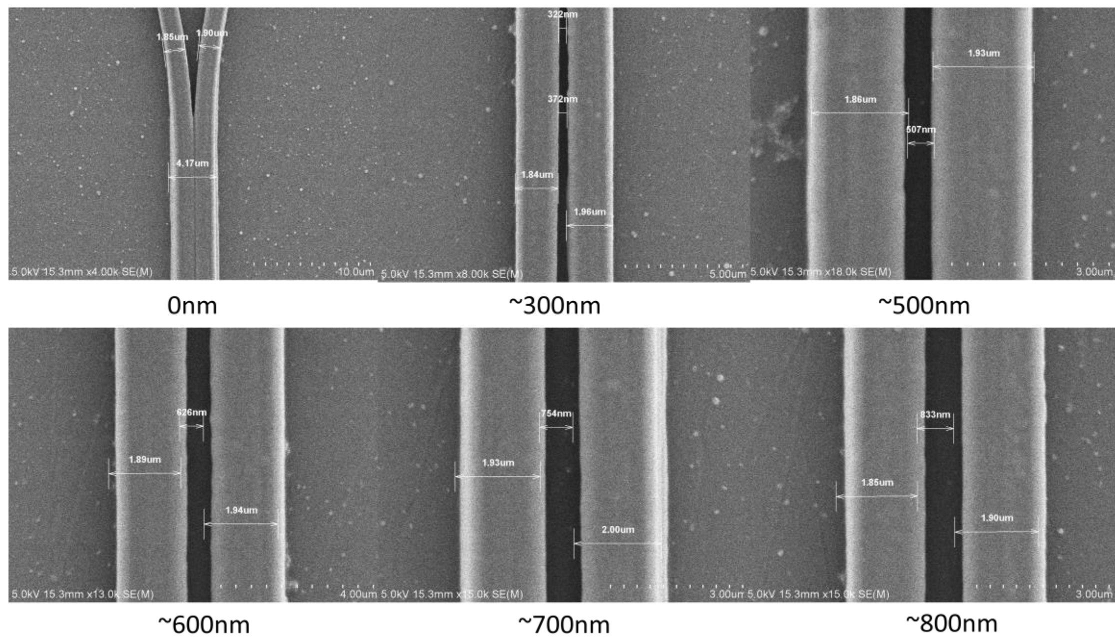

Figure 2.9. SEM images of acrylic couplers with different coupling gaps.

Figure 2.11 shows SEM images of DDR waveguide structures on a PDMS ridge. Their pedestal-shaped cross-section reduces bending loss (light leakage into the substrate), improves the mode confinement and lowers the propagation loss. The pedestal design will be further discussed in Chapter 3.

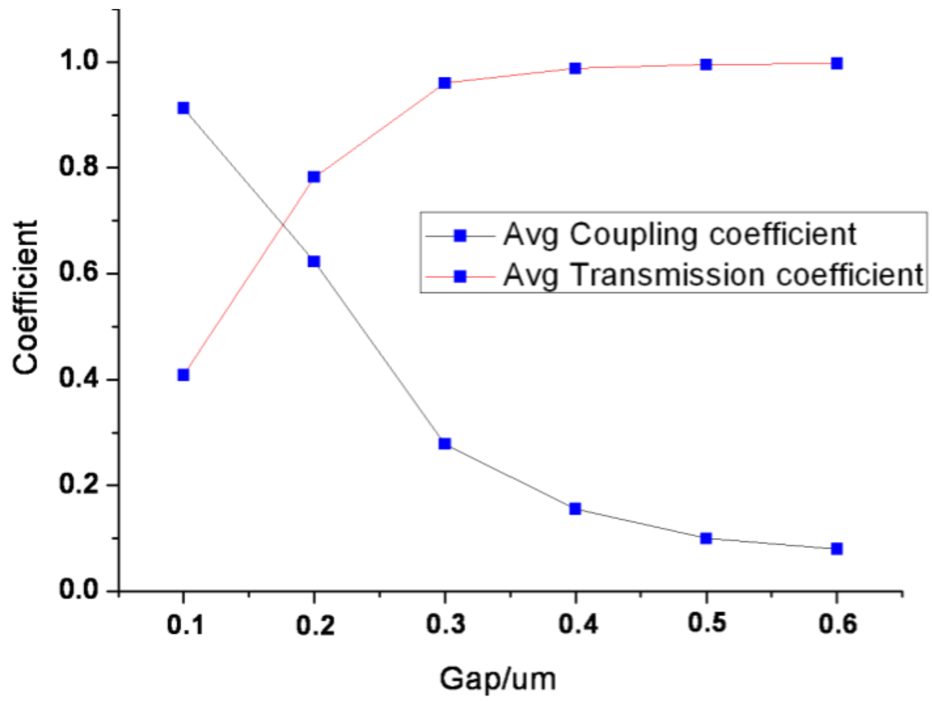

Figure 2.10. Plot of coupling/transmission coefficient vs. coupling gap.

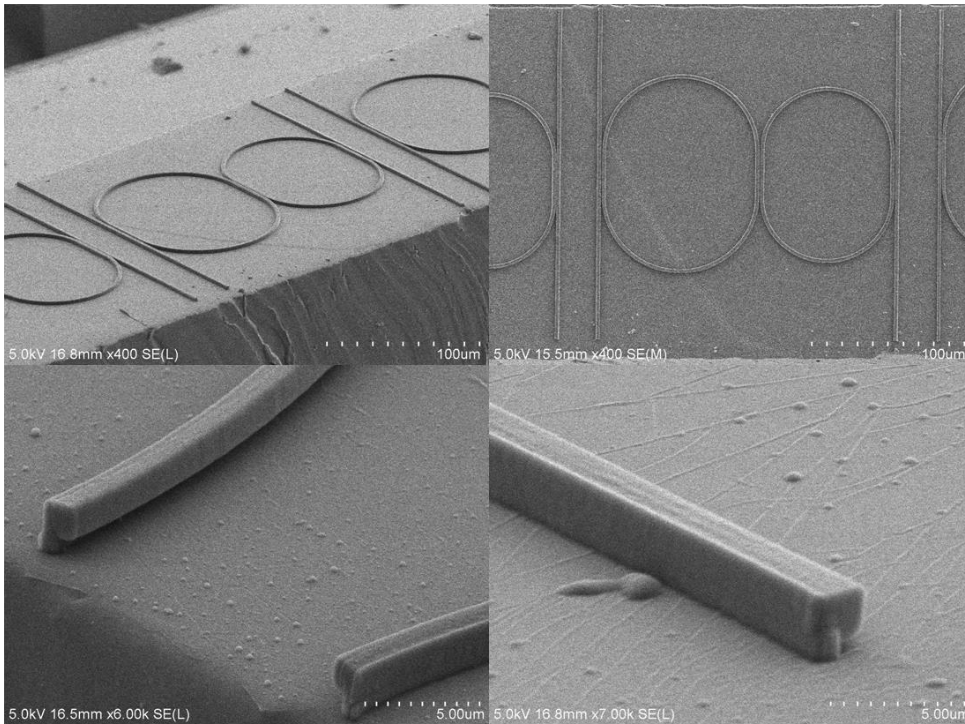

Figure 2.11. SEM images of DRRs with pedestals.

To test a device, tapered lensed fibers were used to couple the light into or out of a resonator. A tunable laser (1520 nm to 1580 nm) from an Agilent 8164A lightwave measurement system was coupled into and out of the DRR device. The output signal was measured by the Agilent 8164A system and was analyzed using a LabVIEW program. The optical source inside the Agilent lightwave measurement system is an InGaAsP Fabry-Perot laser, tunable from 1495 nm to 1640 nm. The beam waist is 9 μm. The wavelength-dependent transmission of resonators can be measured by carrying out a "wavelength sweep" and a transmission measurement simultaneously. For the wavelength sweeps in our experiments, the measurement system changes the wavelength of the optical output (with power of 1 mW) across a pre-defined wavelength range (1530.00 nm to 1580.00 nm) by a specific step size (0.01 nm) with a sweep speed of 10.00 nm per second. Every single device needs two or three cycles of wavelength sweeps. The measurement system contains optical power meters, which receive the transmissions as input light. The power meters measure the optical power of the input light by converting light (photons) to electricity (a current, electrons) and measuring the value of the current. Eventually the data set of wavelengths and corresponding optical intensities are recorded and plotted as the wavelength dependent transmission.

Characteristics such as cross section and surface details of the devices were checked with SEM. This characterization allows for further optimization of the fabrication conditions.

The DRRs were composed of two straight waveguides and two racetrack-shaped microring resonators. The two resonators have radii of 50.7 μm and 43.2 μm, respectively. The straight coupling section is 30 μm long in each microring. As illustrated in Figures 2.12(a) and 2.12(b), two simulated DRR devices with the same

dimensions but different transmission coefficients give completely different spectral responses. Appropriate gap sizes were selected based on the calculations. MAP was used to create the devices with parameters designed to achieve the desired performance, as shown in Figures 2.12(c) and 2.12(d). The simulation and experimental data are in good agreement. Larger isolation can be achieved by further reduction of the propagation loss in the waveguides. Some potential approaches to reduce the loss will be discussed later in this chapter.

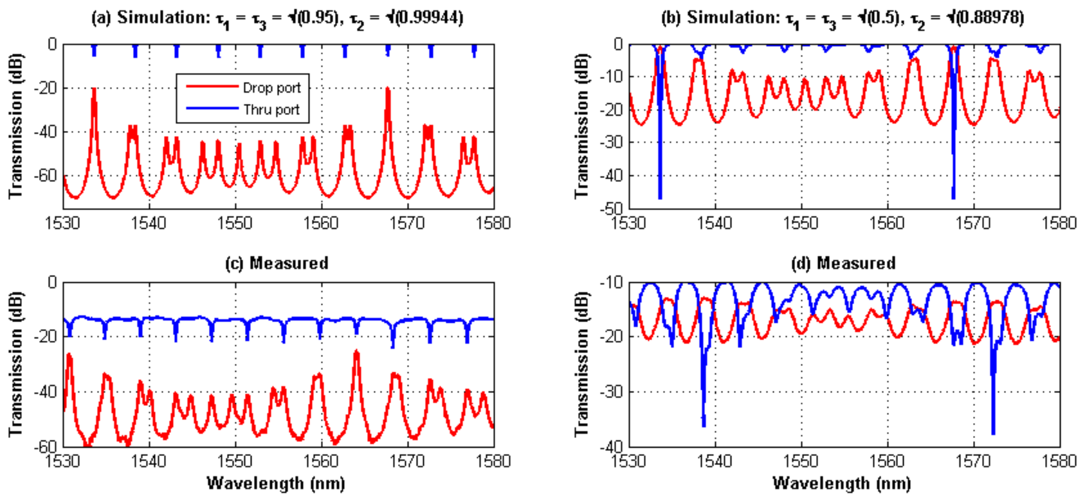

Figure 2.12. (a) and (b) Simulation results for two DRRs with the same pair of ring sizes but different coupling gaps. τ_1 and τ_3 are transmission coefficients between the bus and resonator while τ_2 indicates the transmission coefficient between two resonators in the DRRs; (c) and(d) coresponding experimental data.

The polarization dependence of the device in Figure 2.12 (c) is shown in Figure 2.13. At the drop-port of the DRR, the transverse electric (TE) mode and transverse magnetic (TM) mode have a separation of 1.6 nm and have different transmission intensities. The DRRs are polarization dependent because of polarization dependent coupling/transmission coefficients .

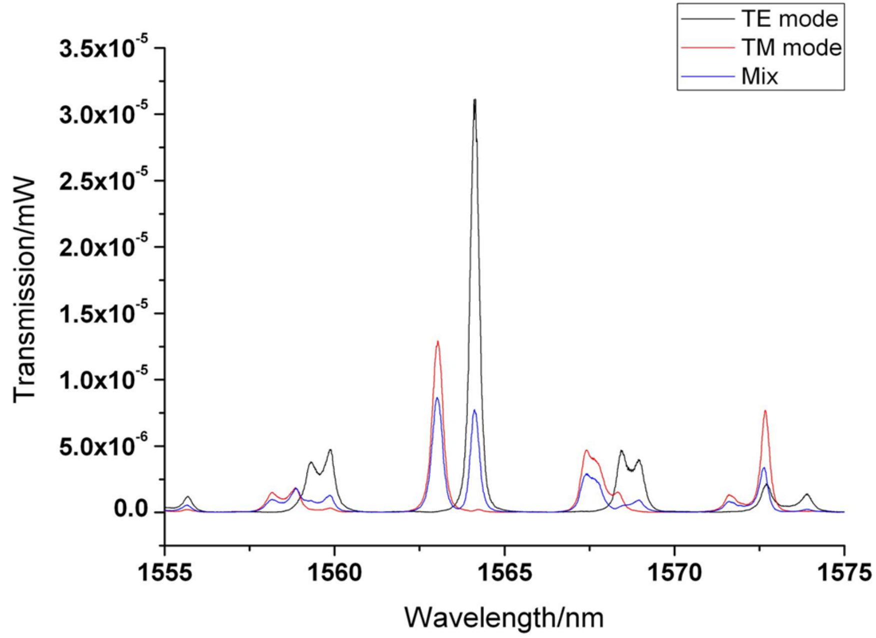

Figure 2.13. Drop-port spectra of a DRR using different polarization states.

2.3.3 Cascaded double-ring resonators

Cascaded DRRs were also investigated. The configuration used is shown in Figure 2.14(a). The pedestal design was again used for the cross section. The drop-port spectrum of this device is shown in Figure 2.14(b). The *FSR* is 26 nm and the isolation is 10 dB.

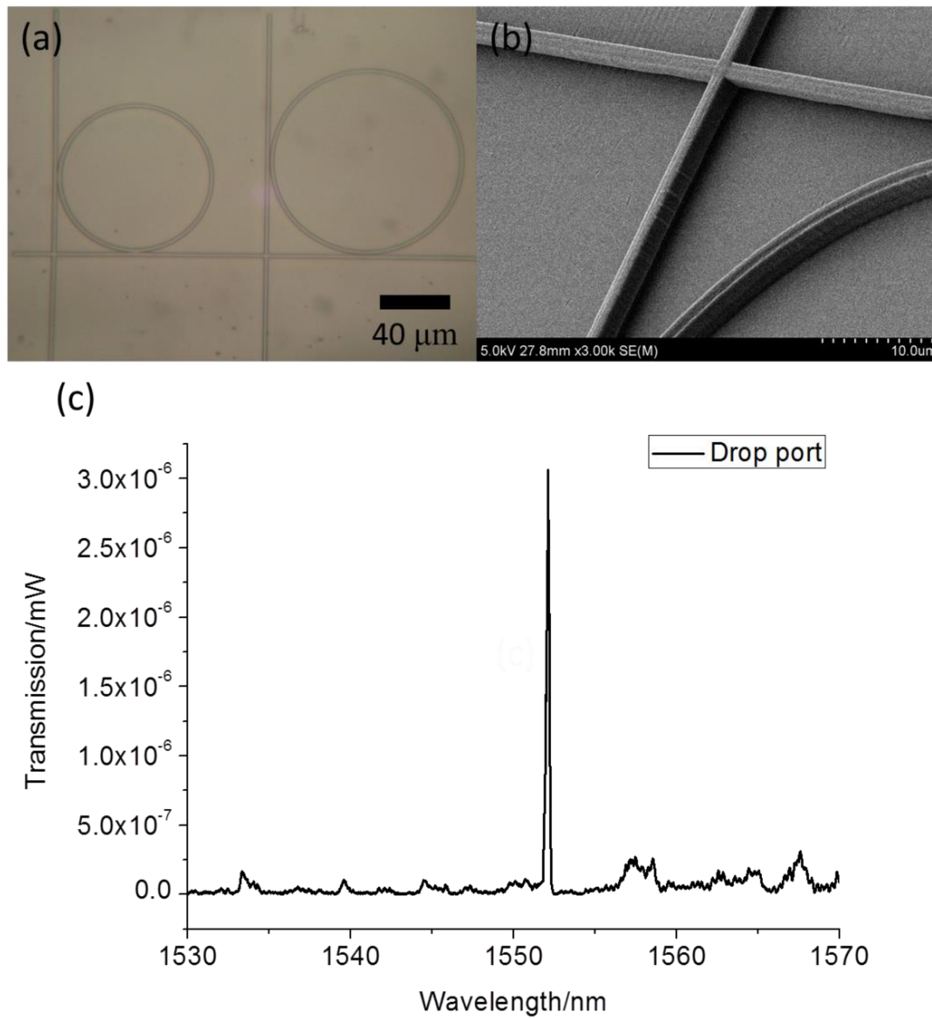

Figure 2.14. (a) Optical image and (b) SEM image of a cascaded DRR device (Radius_small = 40 μm, Radius_big = 50 μm, all gaps are ~ 500 nm). (c) The drop-port spectrum of this device.

2.3.3 Thermal reflow

To improve the device performance further, we have explored thermal reflow as a means to reduce the surface roughness. The surfaces of devices created with MAP in our typical photoresists are smooth, with a roughness of less than 10 nm.

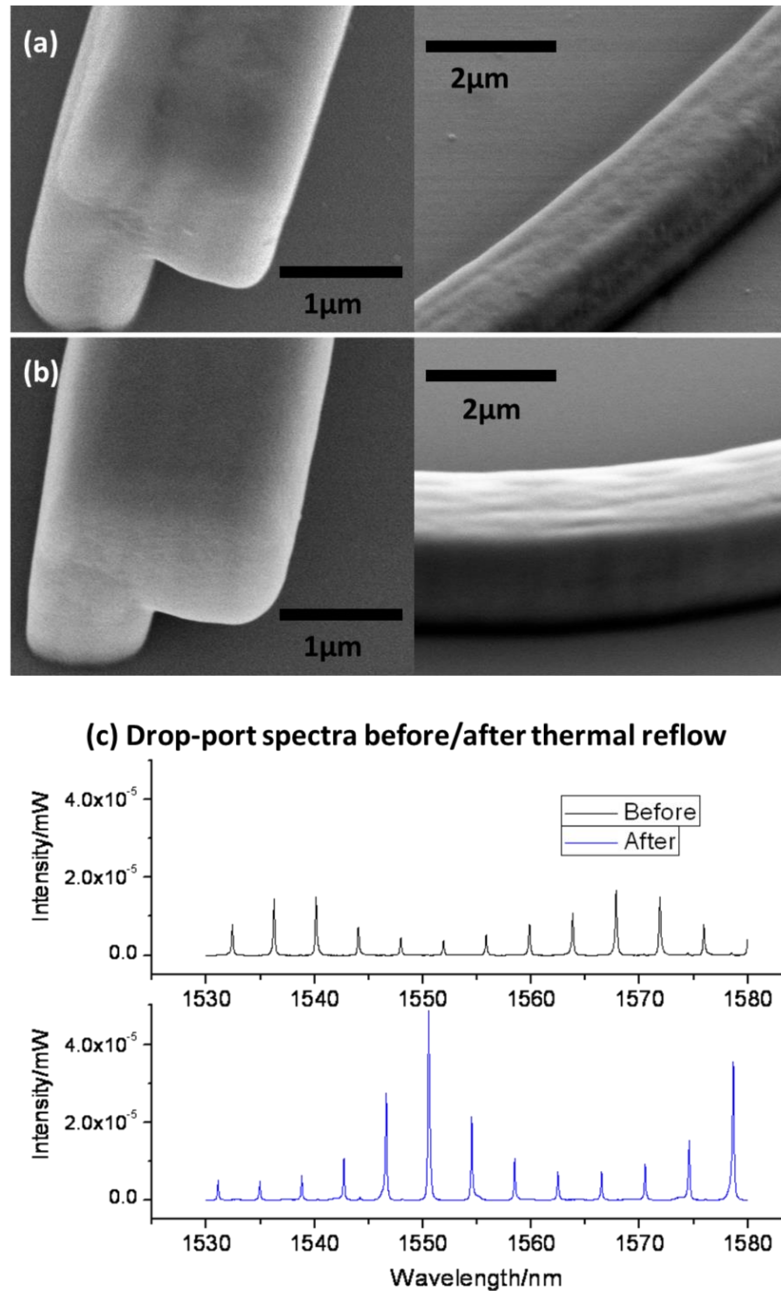

Figure 2.15. (a) and (b) SEM image of the waveguide before and after thermal reflow at 250 ℃ for 60 seconds. (c) Performance of a "snow man" microring resonator device before and after thermal reflow.

However, because MAP is a point-by-point fabrication technique, microscopic or nanoscopic inhomogeneities may exist within the bulk of waveguides, and can degrade performance. We have discovered that holding a device briefly at an elevated temperature can improve its optical performance substantially, and can also increase the yield of high-performance devices considerably. An example of the typical improvement in device performance before and after thermal reflow is shown in Figure 2.15.

2.4 Conclusions

Making use of the coupling coefficient dependence on the coupling gap sizes, proper gap sizes were selected on the basis of calculations to achieve optimum quality of DRRs. Using the chosen parameters, pedestal DRRs with a large *FSR* (>30 nm) and large isolation were directly fabricated using MAP and demonstrated a good match to the simulation results. Thermal reflow and an alternative resin are currently under study for the improvement of device performance.

References

[1] A. H. J. Yang and D. Erickson, "Optofluidic ring resonator switch for optical particle transport," *Lab Chip*, vol. 10, pp. 769–774, 2010.

[2] A. Rostami and G. Rostami, "Full-optical realization of tunable low pass, high pass and band pass optical filters using ring resonators," *Opt. Commun.*, vol. 240, pp. 133–151, 2004.

[3] D. Yevick, "High-speed polymer/silicon on insulator ring resonator switch," *Opt. Eng.*, vol. 47, p. 094601, 2008.

[4] G. Chen, Y. Zhang, D. Huang, X. Zhang, H. Cao, and W. Chen, "Photonic generation of a microwave signal by employing a microfiber ring resonator," *Opt. Commun.*, vol. 282, pp. 2552–2555, 2009.

[5] J. Hu, X. Sun, A. Agarwal, and L. C. Kimerling, "Design guidelines for optical resonator biochemical sensors," *J. Opt. Soc. Am. B*, vol. 26, pp. 1032–1041, 2009.

[6] M. S. Luchansky and R. C. Bailey, "Silicon photonic microring resonators for quantitative cytokine detection and T-cell secretion analysis," *Anal. Chem.*, vol. 82, pp. 1975–1981, 2010.

[7] H. P. Weber and R. Ulrich, "A thin-film ring laser," *Appl. Phys. Lett.*, vol. 19, pp. 38–40, 1971.

[8] P. Rabiei, S. Member, W. H. Steier, L. Fellow, C. Zhang, and L. R. Dalton, "Polymer micro-ring filters and modulators," *J. Lightwave Technol.*, vol. 20, pp. 1968–1975, 2002.

[9] J. Haavisto and G. a Pajer, "Resonance effects in low-loss ring waveguides," *Opt. Lett.*, vol. 5, p. 510, 1980.

[10] D. Rafizadeh, J. P. Zhang, S. C. Hagness, A. Taflove, K. A. Stair, and S. T. Ho, "Waveguide-coupled AlGaAs ¯GaAs microcavity ring and disk resonators with high finesse and 21.6-nm free spectral range," *Opt. Lett.*, vol. 22, pp. 1244–1246, 1997.

[11] P. P. Absil, J. V Hryniewicz, B. E. Little, P. S. Cho, R. a Wilson, L. G. Joneckis, and P. T. Ho, "Wavelength conversion in GaAs micro-ring resonators," *Opt. Lett.*, vol. 25, pp. 554–556, 2000.

[12] Y. Kokubum, S. Kubota, and S. T. Chu, "Polarisation-independent vertically coupled microring resonator filter," *Electron. Lett.*, vol. 37, pp. 90–92, 2001.

[13] B. E. Little, T. Kaneko, and Y. Kokubun, "Cascaded microring resonators for crosstalk reduction and spectrum cleanup in add-drop filters," *IEEE Photon. Technol. Lett.*, vol. 11, pp. 1423–1425, 1999.

[14] S. T. Chu, W. Pan, S. Sato, B. E. Little, T. Kaneko, and Y. Kokubun, "ARROW-type vertical coupler filter: design and fabrication," *J. Lightwave Technol.*, vol. 17, pp. 652–658, 1999.

[15] K. Oda, N. Takato, and H. Toba, "A wide-*FSR* waveguide double-ring resonator for optical FDM transmission systems," *J. Lightwave Technol.*, vol. 9, pp. 728–736, 1991.

[16] D. Rezzonico, A. Guarino, C. Herzog, M. Jazbinsek, and P. Günter, "High-finesse laterally coupled organic – inorganic hybrid polymer microring resonators for VLSI photonics," *IEEE Photon. Technol. Lett.*, vol. 18, pp. 865–867, 2006.

[17] L. Li, E. Gershgoren, G. Kumi, W.-Y. Chen, P.-T. Ho, W. N. Herman, and J. T. Fourkas, "High-performance microring resonators fabricated with multiphoton absorption polymerization," *Adv. Mater.*, vol. 20, pp. 3668–3671, 2008.

[18] A. Schweinsberg, S. Hocdé, N. N. Lepeshkin, R. W. Boyd, C. Chase, and J. E. Fajardo, "An environmental sensor based on an integrated optical whispering gallery mode disk resonator," *Sensor. Actuat. B*, vol. 123, pp. 727–732, 2007.

[19] A. M. Armani and K. J. Vahala, "Heavy water detection using ultra-high-Q microcavities," *Opt. Lett.*, vol. 31, pp. 1896–1898, 2006.

[20] P. P. Yupapin, "Coupler-loss and coupling-coefficient-dependent bistability and instability in a fiber ring resonator," *Int. J. Light Electron Opt.*, vol. 119, pp. 492–494, 2008.

[21] J. Zhang, Y. Zhang, Q. Song, H. Tian, X. Zhang, H. Wu, J. Wang, C. Yu, G. Li, D. Fan, and P. Yuan, "A double-ring Mach–Zehnder interferometer sensor with high sensitivity," *J. Phys. D: Appl. Phys.*, vol. 45, p. 255102, 2012.

[22] W. Bogaerts, P. De Heyn, T. Van Vaerenbergh, K. De Vos, S. Kumar Selvaraja, T. Claes, P. Dumon, P. Bienstman, D. Van Thourhout, and R. Baets, "Silicon microring resonators," *Laser Photon. Rev.*, vol. 6, pp. 47–73, 2012.

[23] J. Yang, Q. Zhou, F. Zhao, X. Jiang, B. Howley, M. Wang, and R. T. Chen, "Characteristics of optical bandpass filters employing series-cascaded double-ring resonators," *Opt. Commun.*, vol. 228, pp. 91–98, 2003.

[24] C. H. Chaichuay, P. R. P. Yupapin, and P. R. Saeung, "The serially coupled multiple ring resonator filters and Vernier effect," *Opt. Appl.*, vol. 39, pp. 175–194, 2009.

[25] B. E. Little, S. T. Chu, H. a. Haus, J. Foresi, and J.-P. Laine, “Microring resonator channel dropping filters,” *J. Lightwave Technol.*, vol. 15, pp. 998–1005, 1997.

[26] A. Shakouri and J. E. Bowers, “Wide tunable double ring resonator coupled lasers,” *IEEE Photon. Technol. Lett.*, vol. 14, pp. 600–602, 2002.

[27] B. D. Timotijevic, F. Y. Gardes, W. R. Headley, G. T. Reed, M. J. Paniccia, O. Cohen, D. Hak, and G. Z. Masanovic, “Multi-stage racetrack resonator filters in silicon-on-insulator,” *J. Opt. A*, vol. 8, pp. S473–S476, 2006.

[28] S. Suzuki, K. Oda, and Y. Hibino, “Integrated-optic double-ring resonators with a wide free spectral range of 100 GHz,” *J. Lightwave Technol.*, vol. 13, pp. 1766–1771, 1995.

[29] D. G. Rabus, M. Hamacher, and H. Heidrich, “Resonance frequency tuning of a double ring resonator in GaInAsP/InP: Experiment and simulation,” *Japan. J. Appl. Phys.*, vol. 41, pp. 1186–1189, 2002.

[30] L. Li, R. R. Gattass, E. Gershgoren, H. Hwang, and J. T. Fourkas, “Achieving lambda/20 Resolution by One-Color Initiation and Deactivation of Polymerization,” *Science*, vol. 324, pp. 910–913, 2009.

[31] A Yariv, Y. Xu, R. K. Lee, and A. Scherer, “Coupled-resonator optical waveguide: A proposal and analysis,” *Opt. Lett.*, vol. 24, pp. 711–713, 1999.

[32] M. Cai, O. Painter, and K. Vahala, “Observation of critical coupling in a fiber taper to a silica-microsphere whispering-gallery mode system,” *Phys. Rev. Lett.*, vol. 85, pp. 74–77, 2000.

[33] H. Kogelnik and T. Li, “Laser beams and resonators,” *Proc. IEEE*, vol. 54, pp. 1312–1329, 1966.

[34] J. Poon, J. Scheuer, S. Mookherjea, G. Paloczi, Y. Huang, and A. Yariv, “Matrix analysis of microring coupled-resonator optical waveguides,” *Opt. Express*, vol. 12, pp. 90–103, 2004.

[35] A. Yariv, "Universal relations for coupling of optical power between microresonators and dielectric waveguides," *Electron. Lett.*, vol. 36, pp. 321-322, 2000

Chapter 3: Surface mapping of side-polished fibers with externally actuatable microring resonators

Adapted from the paper to be submitted to Opt. Exp.

3.1 Introduction

Optical fibers have been used widely in optical communications applications due to their excellent performance in long-distance, high-bandwidth light propagation [1]. For on-board processing or analysis of signals with an optical fiber, other optical components (e.g., modulators or filters) must be employed. However, such components generally introduce significant insertion loss [2]. Micro-structured optical fibers [3-4], such as adiabatically tapered fibers [5], fused conical tapered fibers [6] and side-polished fibers [7] (SPFs) have been investigated as means of reducing insertion loss and facilitating fiber-to-device interfacing. SPFs have proven to be attractive for use as fiber directional couplers [8], sensors [9], polarizers [10], modulators [11], amplifiers [12], and filters [13].

The distance from the polished surface of an SPF to its core critically affects its evanescent coupling to external optical components. Due to the variation of the core dimension of the fiber and the position of the core relative to the polished surface, it is difficult in practice to achieve uniform thickness of the residual cladding in the polished region of the fiber. As shown in Figure 3.1, even in commercial SPFs the cladding layer thickness varies as a function of position on the side-polished face.

Current technology offers good control over the degree of polishing for the polished area as a whole, as typically evaluated by monitoring the transmission loss at the fiber output [7]. However, there are an infinite number of polished configurations that can lead to the same transmission loss, and so monitoring and maintaining local uniformity during polishing remains a challenge. Thus, if an optical device needs to be coupled precisely to an SPF, it is essential to be able to identify the best coupling spot on the polished face. Here we demonstrate the mapping of the polished surface of an SPF using an external, microring-resonator-based device that can be coupled to any desired portion of the side-polished region.

Microring resonators (μRRs) support resonances for specific wavelengths of light [14]. These resonant wavelengths can be isolated without affecting the off-resonance wavelengths, which makes μRRs good candidates for optical wavelength filtering in devices such as integrated photonic circuits [15], modulators [16], sensors [17] and lasers [18]. Many spectral properties of μRRs, such as the wavelengths of the resonances and their finesse (defined in Chapter 2, section 2.2.2), depend sensitively on environment.

We take advantage of this environmental sensitivity to characterize SPFs using polymeric μRR devices. The creation of multimode, polymeric μRRs on SPFs has been reported previously [11, 19]. In contrast, here we use MAP [20, 21] to fabricate high-quality, single-mode polymer μRR devices with a finesse as high as 40 on a separate, low-index substrate. By controlling the position of the substrate, these μRRs can be coupled directly and reproducibly at any point along an SPF without any index-matching liquid [11], thus achieving low insertion loss. As a μRR device is moved along or across the polished surface of an SPF, the varying distance to the fiber core gives different coupling coefficients, leading to a change of the resonance

modulation depth at the fiber output. Based on the modulation depth profile, which depends on the cladding thickness, desirable coupling regions on the SPF can be identified readily. We further demonstrate that the spectral properties of the fiber output are sensitive to the pressure with which a μRR device is pressed against the polished face of the SPF.

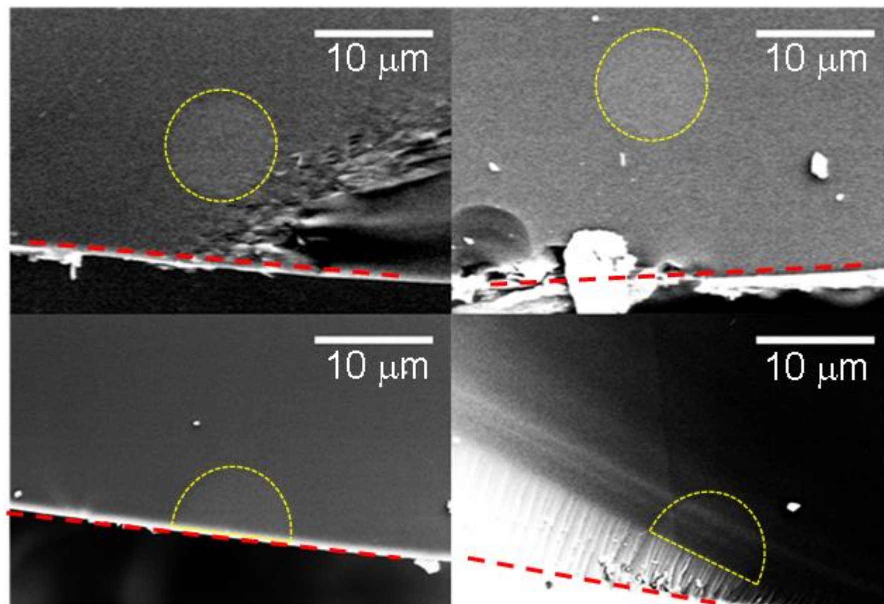

Figure 3.1. Scanning electron micrographs (SEMs) of the cross sections of a single SPF at four different positions within a 500-μm-long polished region. In each SEM image, the region indicated by a dashed yellow boundary is the fiber core and the red dashed line indicates the polished surface. These images clearly show that the residual cladding layer is not uniform.

3. 2 Experimental details

MAP was chosen for the fabrication of the μRRs owing to its ability to create complex, 3D polymeric structures with low surface roughness [20, 21]. We have previously demonstrated that MAP can be used to create high-quality, single-mode, acrylic μRR-based devices [22]. The theory and experimental setup of MAP have been discussed in Chapter 1.

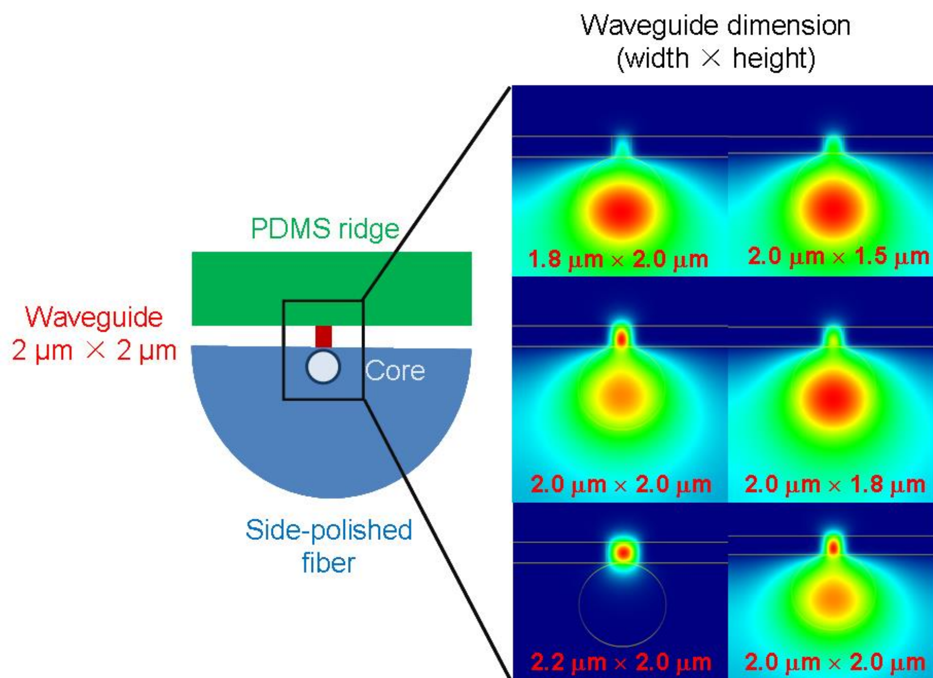

Figure 3.2. (a) A schematic side view of a waveguide on a PDMS ridge coupled to an SPF. (b) Simulations of waveguides of different dimensions coupled to an SPF. The optimal waveguide cross section was determined to be 2 μm × 2 μm.

The μRR devices were fabricated on ridges composed of polydimethylsiloxane (PDMS). The PDMS substrate has a refractive index of 1.41 at 1.5 μm, thus providing a large refractive index contrast with the acrylic polymer (which has a refractive index of 1.49). Due to its elasticity, the PDMS substrate also helps to

protect the μRR devices from damage when they are pressed against SPFs. To prepare the substrate, well-mixed Sylgard 184 (Dow Corning) with a 10:1 mass ratio of prepolymer to curing agent was poured onto a silicon wafer that had been pretreated in a vacuum desiccator using (tridecafluoro-1,1,2,2-tetrahydrooctyl)dimethyl-chlorosilane for 24 h. The Sylgard 184 was sandwiched between the wafer and an oxygen-plasma-cleaned cover glass with a 200 μm separation between them. After curing for 30 min at 95 °C, the PDMS film was peeled off of the silicon wafer and plasma cleaned for 3 min.

To improve the adhesion of the acrylate-based polymer on PDMS, the PDMS was functionalized by immersion in an ethanol solution with 2 vol% (3-acryloxypropyl)-trimethoxysilane and 5 vol% deionized water overnight and then rinsed for 30 min in pure ethanol, followed by heating for 30 min at 95 °C. A 300-μm-wide ridge was cut in the substrate using a razor blade, and the remaining PDMS was peeled away.

The photoresist was prepared by mixing 48.5 wt% tris (2-hydroxy ethyl) isocyanurate triacrylate (SR368, Sartomer) and 48.5 wt% ethoxylated (6) trimethylolpropane triacrylate (SR499, Sartomer), with 3 wt% Lucirin TPO-L (BASF) as a photoinitiator. To prepare the sample for fabrication, one drop of acrylate resin was placed on the PDMS ridge and covered by a thin glass slide with a 40 μm spacer in between. The sample was mounted on a 3D piezo stage (Physik Instrumente) that was installed on an inverted microscope. As Ti:Sapphire laser (Coherent Mira 900-F) produced 800-nm, 150-fs pulses that were focused by a 100×, 1.45 NA, oil-immersion objective (Zeiss α Plan-FLUAR). A LabView program controlled the movement of the piezo stage to fabricate a pre-designed structure. The unexposed photoresist was then developed away in ethanol.

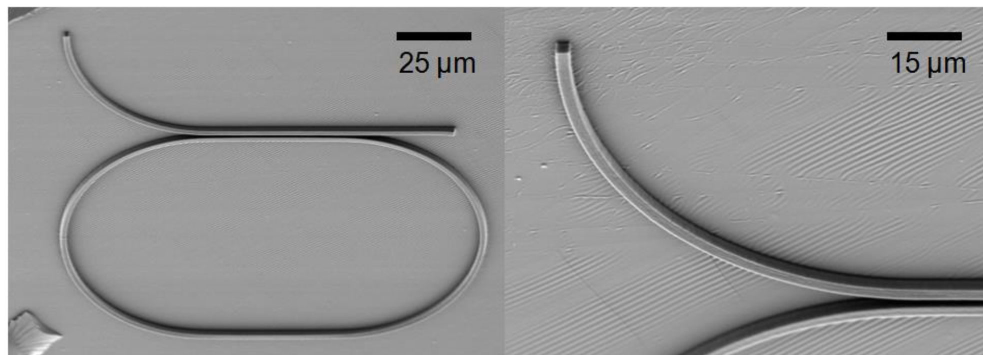

Figure 3.3. (a) SEM image of a µRR device on a PDMS substrate. The radius of curvature of the ring is 50 µm, the length of the straightaways (and the coupling region) is 50 µm and the cross section is 2 µm × 2 µm. (b) A closeup view of the same device. The curved bus was designed to facilitate measurements at the drop port.

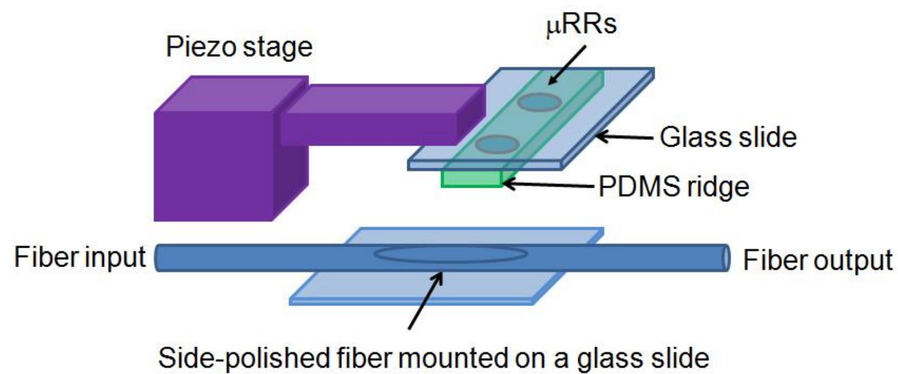

Figure 3.4. Schematic diagram of the device measurement setup. The sample was mounted on the 3D piezo stage with the µRR devices facing down. The SPF was glued on a glass slide with the polished face up. An Agilent 8164A Lightwave Measurement System acted as the infrared light source and was used to measure the through-port and drop-port signals.

The optimal waveguide dimensions were determined using a finite-element program (Fiber Optical Mode Solver, Apollo Photonics), as illustrated in Figure 3.2.

In the calculations, a linear polymer waveguide on a PDMS substrate was contacted with the SPF, which had a refractive index 1.440 for the core and 1.437 for the cladding. The thickness of the cladding between the waveguide and fiber core was assumed to be zero. Different combinations of waveguide height and width were examined, and it was determined that dimensions of 2 μm × 2 μm were optimal for meeting the phase-matching condition and maintaining single-mode properties. A microring design in a "racetrack" pattern was chosen for fabrication, as the elongated coupling region gives more efficient coupling between the resonator and the fiber core. SEMs of a representative μRR device are shown in Figure 3.3.

The measurement setup is shown in Figure 3.4. The sample was mounted on a piezoelectric motorized stage above an SPF (Phoenix Photonics) immobilized on a glass slide with its polished side up. Examination under a microscope was used to ensure that the polished face of the SPF was horizontal and free of twist. An Agilent 8164A Lightwave Measurement System was used to introduce the tunable infrared laser source into the SPF and to measure the through-port and drop-port outputs. The coupling region of the μRR was aligned with the fiber core, and the device performance was analyzed as the μRR was moved relative to the SPF. As illustrated in Figure 3.5, the through-port spectrum was collected at the SPF output and the drop-port spectrum was collected at the end of the curved waveguide (using a tapered fiber).

3.3 Results and discussion

3.3.1 Spectral properties of single racetrack resonator on an SPF

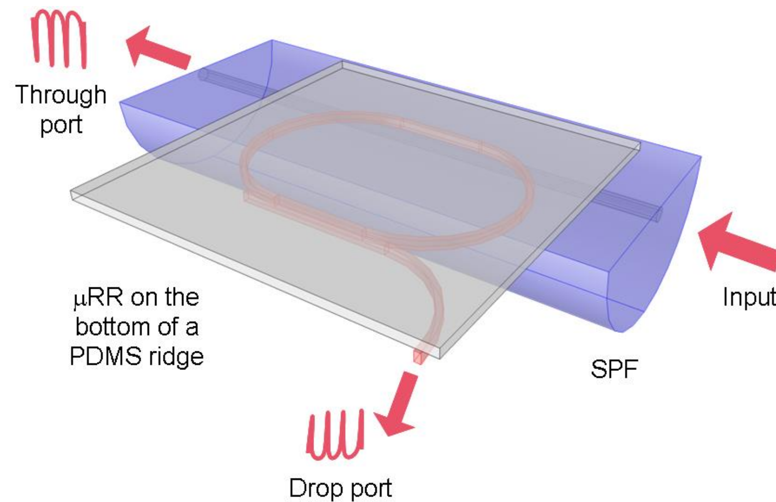

Figure 3.5. Schematic diagram of the optical measurement system. A μRR device is contacted with the SPF, allowing light propagating in the SPF to couple into the resonator. Spectral notches are observed at the fiber output (the through port) and complementary transmission maxima are observed at the end of the curved waveguide (the drop port) using a tapered fiber.

When a μRR device is coupled to an SPF, spectral notches are observed in the fiber output, as shown in Figure 3.6(a). Spectra for the through port and the drop port of a racetrack μRR that had been contacted with an SPF are shown in Figures 3.6(a) and 3.6(b). In this case the μRR had a radius of curvature of 50 μm in the semicircular regions and a "straightaway" length of 50 μm. The finesse in the through-port spectrum was ~22. Through-port modulation depths observed for typical devices were on the order of 1 to 2 dB. The baseline of a typical through-port spectrum was less than -0.2 dB, indicating the low insertion loss of these devices.

The finesse of typical drop-port spectra was lower than that in the through-port spectra, although the resonances were generally more than 10 dB above the baseline.

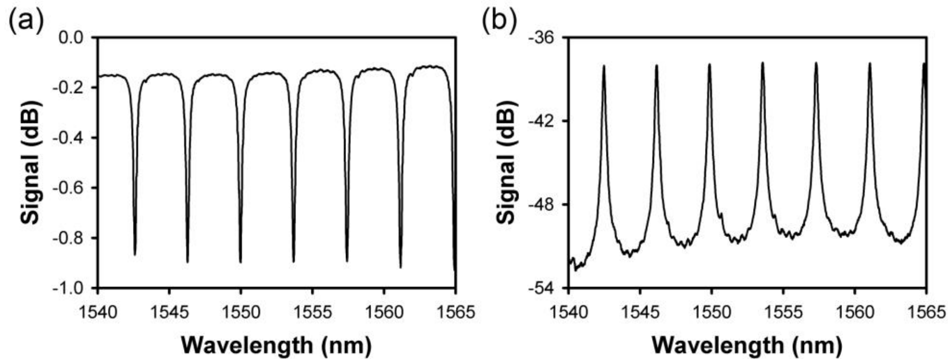

Figure 3.6. (a) Through-port and (b) drop-port spectra for a racetrack μRR device with a 50 μm radius of curvature and a 50-μm-long coupling region.

3.3.2 SPF surface mapping

The spectra shown in Figure 3.6 were obtained with a μRR device in contact with an optimized position on the SPF used. As shown in Figure 3.7, the spectrum at the fiber output is highly dependent on the position of the coupling region of the μRR device relative to the fiber core. Figure 3.7(a) shows a portion of the through-port spectrum as a device is translated across the core at a fixed position along the length of the core. As shown in Figure 3.7(b), the finesse remains relatively constant as the device is moved across the core, while the modulation depth is highly sensitive to position. Conversely, as a device is translated along the core while remaining at the optimal position across the core, the through-port spectrum changes in a manner that reflects the local thickness of the cladding (Figure 3.7(c)). The finesse is also relatively insensitive to the position along the core (except at the extremities of the side-polished region), while the modulation depth depends strongly on position (Figure 3.7(d)). The optimal position for coupling the device to the SPF can be

identified readily from these plots. The same ideal coupling position on a given SPF was found in multiple experiments and with different μRR devices, demonstrating the robustness of this technique.

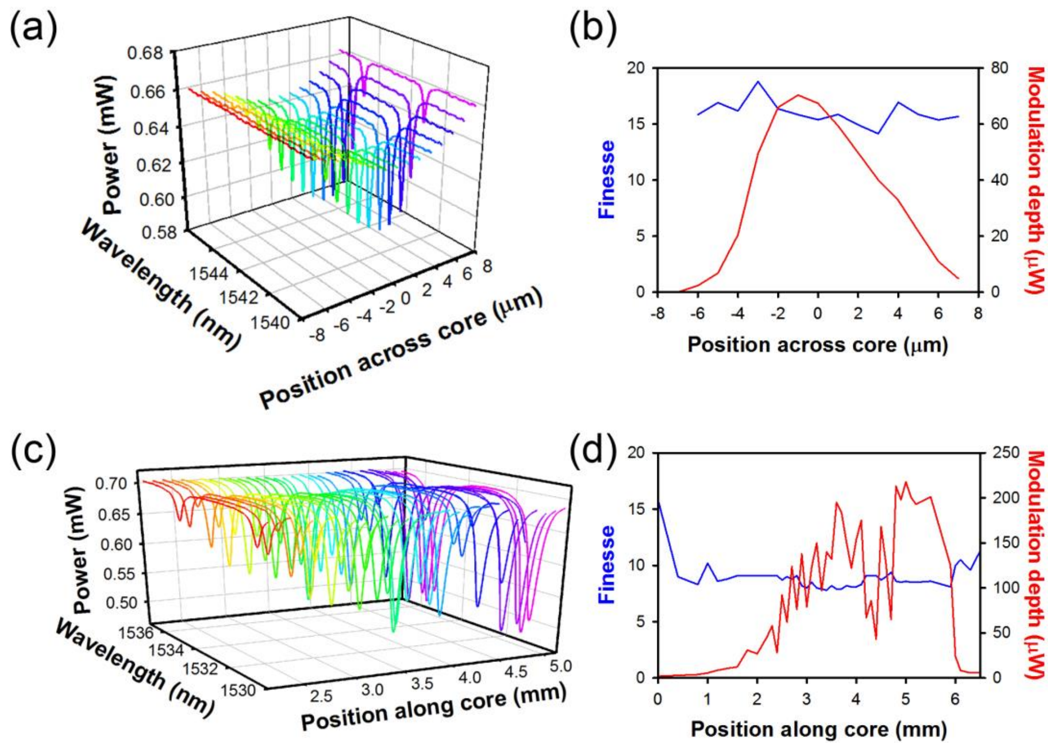

Figure 3.7. (a) Through-port spectrum when a μRR device with a 50 μm radius of curvature and a 50 μm coupling region was moved across the core of an SPF. (b) Finesse and modulation depth of the through-port spectrum as a function of position across the core. (c) Through-port spectrum when a μRR device with a 40 μm radius of curvature and a 60 μm coupling region was moved along the core of the SPF. (d) Finesse and modulation depth of the through-port spectrum as a function of position along the core.

3.3.3 Pressure sensing using a microring resonator on an SPF

The through-port and drop-port spectra are also sensitive to the vertical position of μRR device relative to the polished face of an SPF. Shown in Figure 3.8(a) are through-port spectra obtained as a device was lowered onto the core of an SPF. The evanescent coupling increases with decreasing distance between the device

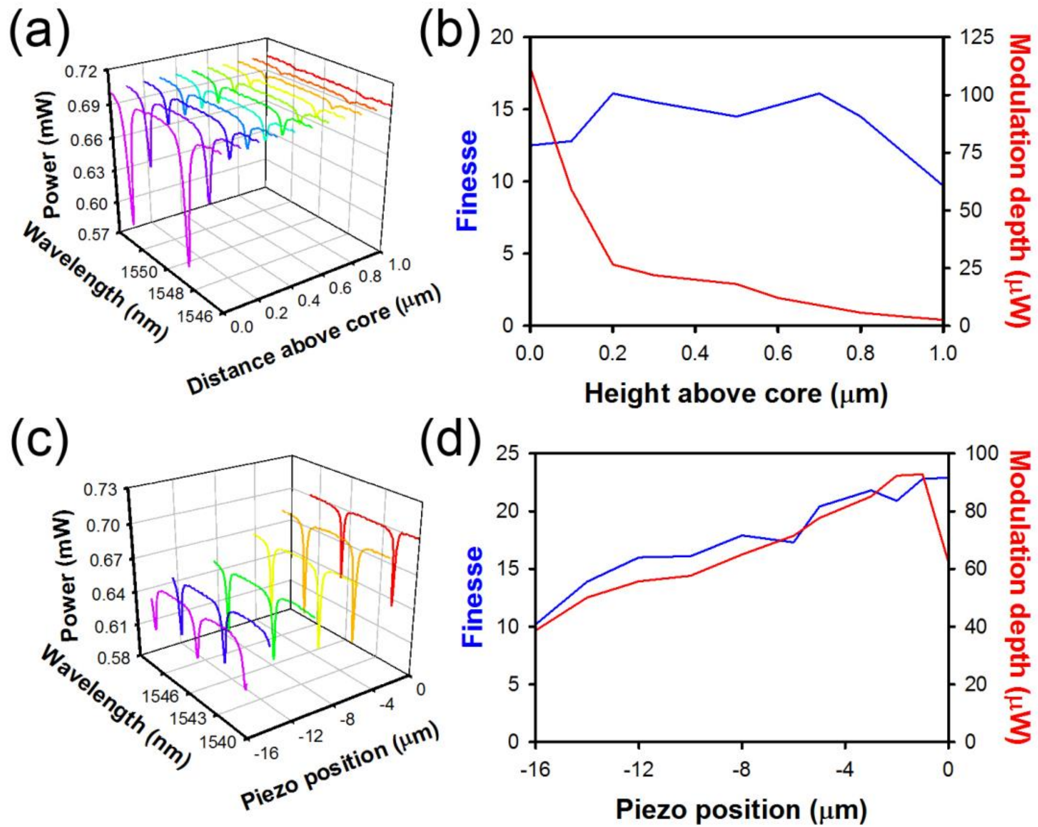

Figure 3.8. (a) Through-port spectrum when a μRR device with a 40 μm radius of curvature and a 60 μm coupling region approached the side-polished face of an SPF vertically. (b) Finesse and modulation depth of the through-port spectrum as a function of height above the core. (c) Through-port spectrum when a μRR device with a 40 μm radius of curvature and a 40 μm coupling region was pressed into the polished face of the SPF. (d) Finesse and modulation depth of the through-port spectrum as a function of the vertical piezo position (which is proportional to pressure).

and the SPF, leading to a substantial increase in the modulation depth of the through-port spectrum while the finesse remains relatively constant (Figure 3.8(b)). The dependence of the modulation depth on distance from the SPF face is roughly exponential, with a decay constant of approximately 0.3 μm. This distance is in reasonable agreement with the evanescent decay constant expected based on the refractive indices of the media [23].

Once a μRR device has been brought into contact with an SPF, the through-port and drop-port spectra are also dependent upon the pressure with which the contact is made. Because PDMS is highly elastic, it is possible for the device to function even after the vertical piezo has been moved for many μm past the point of contact. Thus, a μRR coupled to an SPF by this method can also serve as a pressure sensor. Typical through-port spectra are shown in Figure 3.8(c) as a function of the vertical piezo position, where 0 denotes the point of contact. There is a clear spectral shift as the pressure is increased. Furthermore, as shown in Figure 3.8(d), both the modulation depth and the finesse decrease linearly with increasing pressure. As the finesse is relatively insensitive to the position along, across or above an SPF, a decrease in finesse is a clear indication that pressure has been applied to the μRR device. The observed spectral changes are completely reversible over hundreds of cycles of a μRR device being brought into contact with an SPF.

3.3.4 Waveguides with a pedestal cross section

We have explored three different approaches to improving the performance of MAP-fabricated devices that can be coupled to SPFs. The first approach involves creating a pedestal for the waveguides to lower the effective refractive index of the substrate. Even though PDMS has a relatively low refractive index (~1.41), air-clad waveguides exhibit even lower propagation and bending losses than do waveguides fabricated on PDMS. Using MAP, it is relatively simple to create the waveguides on top of a narrow pedestal composed of the same material as the waveguide. With an appropriate design, relatively little light couples into the pedestal (and the PDMS), improving the overall device performance. In Figure 3.9 we show a comparison of some of the best SPF output spectra for microring resonators in which the waveguides are fabricated without a pedestal and with a pedestal. It is clear from this figure that the pedestal provides a substantial improvement in performance.

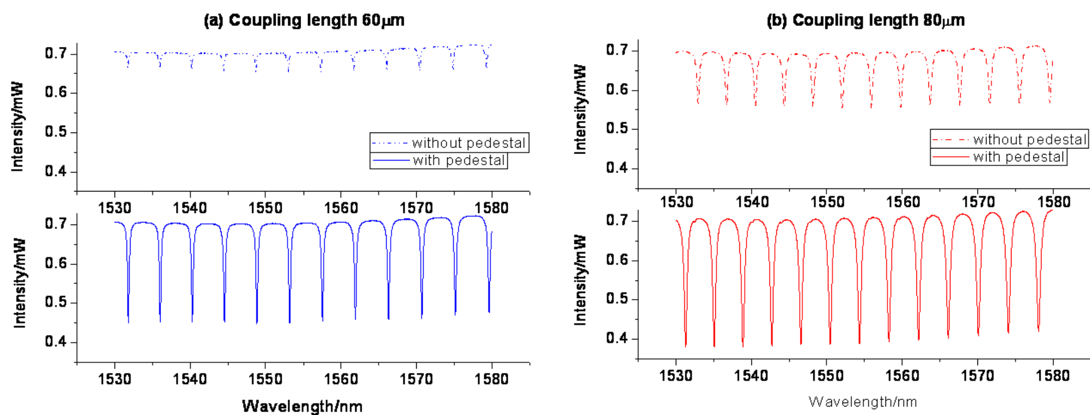

Figure 3.9. (a) Comparison of two microring resonators with and without a pedestal configuration. The μRRs have the same radius of curvature (40 μm) and the length of their straight sections is 60 μm. (b) Another group of resonators with a coupling length of 80 μm.

3.3.5 Effect of the coupling region length

As shown in Figure 3.10, to drop higher intensity out of the SPF, racetrack pedestal resonators with coupling lengths up to 200 μm have been fabricated and tested. When a 200 μm coupling length was used, 90% of the intensity in the SPF was filtered out at the resonance wavelengths. These pedestal resonators all have the same radius (40 μm) with a different coupling length.

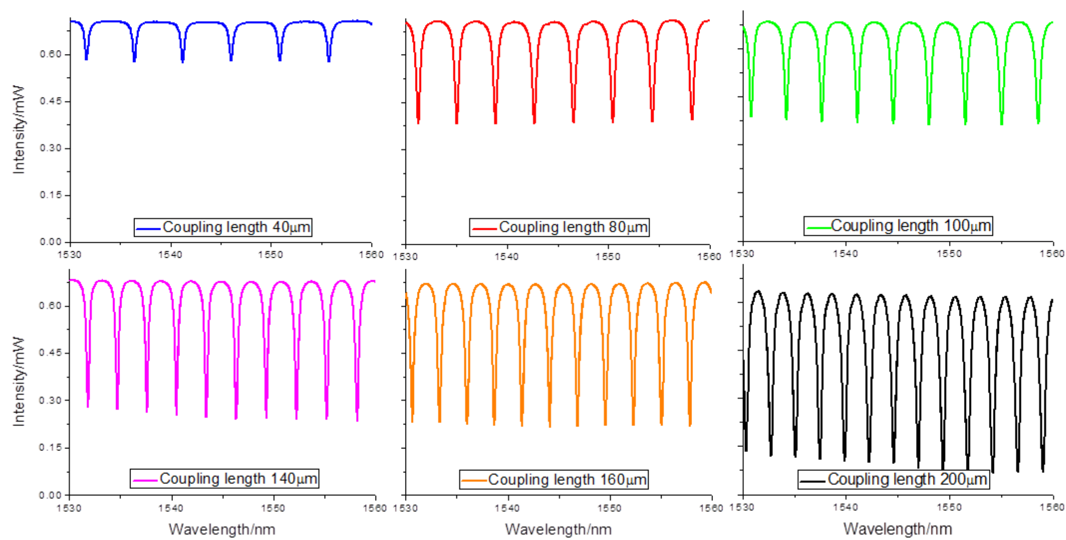

Figure 3.10. Pedestal resonators with the same radius of curvature (40 μm) and different coupling lengths were tested on the SPF. When the coupling length is increased, the extinction ratio improves.

3.4 Conclusions

We have demonstrated that μRR devices fabricated on a PDMS substrate offer a simple means of mapping the spatial dependence of the coupling on the polished face of an SPF. Coupling measurements made in this manner are non-destructive and highly reproducible. The resolution of the mapping depends on the length of the coupling region of the μRR device, which can be matched to the coupling length of whatever device is ultimately intended to be coupled to the SPF. It is also possible to fabricate a set of μRR devices with a range of coupling lengths on a single PDMS substrate so that mapping can be performed at any desired resolution.

Once a device has been fabricated on an SPF, whether with MAP or another technique, it can be difficult to remove cleanly. Thus, SPFs are not typically extensively reusable. The ability to identify the optimum coupling region on a given SPF can thus enable higher yields of SPF-based devices. Furthermore, given the low insertion losses of the μRR-based devices discussed here, it is apparent that in many applications it may be preferable to bring an external optical device into contact with an SPF rather than fabricating the device on the SPF. This strategy allows the SPF to be reused as many times as desired and makes it possible to couple different devices to the SPF as required.

We have also demonstrated that spectrum of a μRR device that has been fabricated on a PDMS substrate and is brought into contact with an SPF is sensitive to pressure. This phenomenon could lend itself to the development of new sensors. The fact that resonances of the device shift with increasing pressure could also be employed as a tuning mechanism.

References

[1] W. A. Gambling, “The rise and rise of optical fibers,” *IEEE J. Sel.Top. Quantum Electron.*, vol. 6, pp. 1084–1093, 2000.

[2] L. F. Stokes, M. Chodorow, and H. J. Shaw, “All-single-mode fiber resonator,” *Opt. Lett.*, vol. 7, pp. 288–290, 1982.

[3] M. J. Guy, S. V Chernikov, J. R. Taylor, and R. Kashyap, “Low-loss fibre Bragg grating transmission filter based on a fibre polarisation splitter,” *Electron. Lett.*, vol. 30, pp. 1512–1513, 1994.

[4] A. S. Kewitsch, G. A. Rakuljic, P. A. Willems, and A. Yariv, “All-fiber zero-insertion-loss add-drop filter for wavelength-division multiplexing,” *Opt. Lett.*, vol. 23, pp. 106–108, 1998.

[5] J. C. Knight, G. Cheung, F. Jacques, and T. a Birks, “Phase-matched excitation of whispering-gallery-mode resonances by a fiber taper,” *Opt. Lett.*, vol. 22, pp. 1129–1131, 1997.

[6] B. S. Kawasaki, K. O. Hill, and R. G. Lamont, “Biconical-taper single-mode fiber coupler,” *Opt. Lett.*, vol. 6, pp. 327–328, 1981.

[7] S. Tseng and C. Chen, “Side-polished fibers,” *Appl. Opt.*, vol. 31, pp. 3438–3447, 1992.

[8] J. Laegsgaard, O. Bang, and A. Bjarklev, “Photonic crystal fiber design for broadband directional coupling,” *Opt. Lett.*, vol. 29, pp. 2473–2475, 2004.

[9] W. Jung, S. Kim, K. Kim, E. Kim, and S. Kang, “High-sensitivity temperature sensor using a side-polished single-mode fiber covered with the polymer planar waveguide,” *IEEE Photon. Technol. Lett.*, vol. 13, pp. 1209–1211, 2001.

[10] F. Polarizers, S. Ma, and S. Tseng, "High-performance side-polished fibers and applications as liquid crystal clad," *J. Lightwave Technol.*, vol. 15, pp. 1554–1558, 1997.

[11] H. Sun, S. Member, A. Pyajt, J. Luo, Z. Shi, S. Hau, A. K. Jen, L. R. Dalton, A. Chen, and A. Abstract, "All-dielectric electrooptic sensor based on a polymer microresonator coupled side-polished optical fiber," *IEEE Sensor. J.*, vol. 7, pp. 515–524, 2007.

[12] R. K. Varshney, A. Singh, K. Pande, and B. P. Pal, "Side-polished fiber based gain-flattening filter for erbium doped fiber amplifiers," *Opt. Commun.*, vol. 271, pp. 441–444, 2007.

[13] N.-K. Chen, S. Chi, and S.-M. Tseng, "Wideband tunable fiber short-pass filter based on side-polished fiber with dispersive polymer overlay," *Opt. Lett.*, vol. 29, pp. 2219–2221, 2004.

[14] J. Heebner, R. Grover, and T. Ibrahim, "Optical microresonator theory," in *Optical Microresonators: Theory, Fabrication, and Applications*, 2008, pp. 71–103.

[15] J. V. Hryniewicz, P. P. Absil, B. E. Little, R. a. Wilson, and P.-T. Ho, "Higher order filter response in coupled microring resonators," *IEEE Photon. Technol. Lett.*, vol. 12, pp. 320–322, 2000.

[16] P. Rabiei, S. Member, W. H. Steier, L. Fellow, C. Zhang, and L. R. Dalton, "Polymer micro-ring filters and modulators," *J. Lightwave Technol.*, vol. 20, pp. 1968–1975, 2002.

[17] N. Jokerst, M. Royal, S. Palit, L. Luan, S. Dhar, and T. Tyler, "Chip scale integrated microresonator sensing systems," *J. Biophoton.*, vol. 2, pp. 212–226, 2009.

[18] M. K. S. Martin T. Hill, Harmen J. S. Dorren, Tjibbe de Vries, Xaveer J. M. Leijtens, Jan Hendrik den Besten, Barry Smalbrugge, Yok-Siang Oei, Hans Binsma, Giok-Djan Khoe, “A fast low-power optical memory based on coupled micro-ring lasers,” *Nature*, vol. 432, pp. 11–14, 2004.

[19] T. Sherwood, A. C. Young, J. Takayesu, A. K. Y. Jen, and L. R. Dalton, “Microring resonators on side-polished optical fiber,” *IEEE Photon. Technol. Lett.*, vol. 17, pp. 2107–2109, 2005.

[20] Shoji Maruo and J. T. Fourkas, “Recent progress in multiphoton microfabrication,” *Laser Photon. Rev.*, vol. 2, pp. 100–111, 2008.

[21] C. N. LaFratta, J. T. Fourkas, T. Baldacchini, and R. a Farrer, “Multiphoton fabrication.,” *Angew. Chem. Int. Ed.*, vol. 46, pp. 6238–58, 2007.

[22] L. Li, E. Gershgoren, G. Kumi, W.-Y. Chen, P.-T. Ho, W. N. Herman, and J. T. Fourkas, “High-performance microring resonators fabricated with multiphoton absorption polymerization,” *Adv. Mater.*, vol. 20, pp. 3668–3671, 2008.

[23] H. Zappe, *Fundamentals of Micro-Optics* (Cambridge University Press, Cambridge, UK, 2010)

Chapter 4: Simultaneous Optical Microscale Manipulation, Immobilization, and Fabrication in Aqueous Media

Adapted from Chem. Sci., vol. 3, pp. 2449-2456, 2012

4.1 Introduction

The development of next-generation microtechnologies for advancing fields such as biomedical engineering, nanophotonics, and analytical chemistry could benefit greatly from new methods for the integration of microstructures into functional devices. Fabrication schemes that substitute water for organic solvents would be highly advantageous, as water is inexpensive, non-toxic, and bio-compatible. For example, to understand the fundamental behavior of individual cells and their interactions with one another, it is beneficial to employ an *in vitro* environment that can mimic the 3D geometries of typical *in vivo* settings [1, 2]. Moreover, microfluidic devices, which are major components of a new generation of miniature instruments for molecular analysis, electrochemical sensing, medical analysis and other applications, are typically most compatible with water-based media [3-5]. Accordingly, for applications such as the incorporation of new structures (e.g., mixers or reactors) into existing microfluidic devices and structural modifications of the walls of microfluidic channels, it is vital to have water-based media for fabrication. In addition, water-based fabrication methods have the potential for use in

the creation of microstructures that are composed of multiple materials and/or that cannot be realized entirely through direct-write fabrication techniques.

It is therefore desirable to have a toolbox of microtechnologies for the fabrication and manipulation of complex, functional microstructures that can be used in applications such as biomolecular scaffolds, sensors, electronics, adhesives, and coatings [6-8]. This need is a major driving force for the advancement of optical fabrication techniques that are amenable to entirely water-based conditions.

Optical tweezers is an attractive candidate technique for incorporating nanoscale manipulation into water-based fabrication techniques. Optical trapping has revolutionized the non-invasive manipulation and positioning of microparticles in low-refractive-index liquids such as water [9-12]. By taking advantage of the refractive qualities of dielectric materials, optical tweezers can exert piconewton forces for applications in areas such as particle sorting [13-15], micromachines [16-18], single-molecule biophysical studies [19-22] and microfabrication [23].

While optical tweezers have been employed broadly for manipulation, their use for immobilizing objects in a given architecture has been limited to date. In one example of such immobilization, Marr and co-workers used photopolymerization of an aqueous photoresist to fabricate linear aggregates of silica microbeads for use in microfluidic devices [24, 25]. However, the polymerization could only take place at the focal region of the optically trapped microbead, which served as a lens. In addition, Arnold and co-workers have reported a method for direct-write patterning of surfaces using optically trapped microbeads as lenses [26, 27].

Nonlinear optical (NLO) techniques based on multiphoton absorption are powerful methods for fabricating microstructures. In NLO fabrication methods, the photochemical or photophysical transformation of a material is restricted to the focal

volume of a laser beam that has been focused through a microscope objective. One of the most developed NLO fabrication processes is multiphoton absorption polymerization (MAP), in which a prepolymer resin consisting of reactive monomers and a photoinitiator is activated with ultrafast pulses of near-infrared light [28-31]. Due to a combination of optical and chemical nonlinearity, structures created with MAP can have dimensions on the nanoscale [32, 33]. MAP also allows for the fabrication of complex 3D structures.

The vast majority of work in MAP to date has been accomplished either in neat photoresists or in photoresists with an organic solvent. Multiphoton fabrication in aqueous media has primarily been restricted to the crosslinking of biomolecules via photosensitizers, which is an area of rapidly growing interest [34-39]. While the resultant materials are generally bio-compatible, the biomolecular starting materials are typically considerably more expensive than their organic counterparts. Biomolecular microarchitectures are also often not as robust as ones created from synthetic polymers. Also, structures consisting solely of biomolecular materials may be unsuitable for optical manipulation, as the forces acting on the biomolecules can potentially change their conformations irreversibly.

To construct robust structures that are viable for optical trapping in water-based media, it is desirable to be able to perform free-radical photopolymerization in aqueous conditions. Radical photopolymerization carried out in aqueous media typically has a lower efficiency than in organic media. Thus, the need for efficient and water-soluble radical photoinitiators for MAP remains to be addressed. The types of photosensitizers that have been used for protein crosslinking have also been demonstrated to polymerize acrylates in water [40], but these species have high visible absorption and relatively small windows for processing (the maximum laser

power that can be used for fabrication divided by the minimum laser power that can be used for fabrication). Water-soluble photoinitiators such as chromium-based compounds are widely used in the stencil industry [41]. However, these materials have a short shelf life and are toxic, which poses environmental problems. Another approach to aqueous radical photopolymerization employs micro/miniemulsions and micellar polymerization [42]. Ober and co-workers have used a related method to solubilize a hydrophobic sensitizer/photoinitiator pair in water for MAP fabrication of hydrogels [43]. This chemistry was successful for 3D MAP fabrication, but the sample preparation time is long and the processing window is relatively small.

Here we introduce water-based photoresists that can be prepared rapidly and are capable of efficient MAP fabrication with a large intensity window for processing. Not only can these materials be used for the fabrication of robust 3D structures via MAP, but the optical clarity, low refractive index and low viscosity of the resists make them suitable for simultaneous MAP fabrication and optical manipulation. These capabilities in turn allow for the creation of structures that are otherwise unattainable using traditional fabrication techniques. Additionally, the mechanical properties of the structures created can be controlled through simple chemical means [44, 45]. Based on these combined abilities, we demonstrate a suite of techniques for microfabrication using a combination of manipulation, polymerization, and immobilization. These techniques include 2D and 3D microassembly, microbraiding and microweaving. We also demonstrate that these microfabrication techniques are compatible with structures created via the radical crosslinking of proteins.

4.2 Materials and methods

4.2.1 Preparation of acrylate-functionalized glass substrates

To promote adhesion of the polymeric structures, #2 Corning glass coverslips (25 mm × 25 mm) were first subjected to an oxygen plasma for 3 minutes. The cover slips were functionalized by immersion for ~16 h in a solution consisting of 93 vol% anhydrous ethanol, 5 vol% deionized water, and 2 vol% (3-acryloxypropyl)trimethoxysilane (Gelest). The coverslips were then submerged in anhydrous ethanol for 1 h, after which they were baked at 95 ℃ for 1 hour.

4.2.2 Preparation of fluorinated substrates

To confine the water-based photoresist during fabrication, wells with polydimethylsiloxane (PDMS) side walls were prepared as follows. A 10:1 mass ratio mixture of Sylgard 184 (Dow Corning) to curing agent was poured onto a silicon wafer that had been treated overnight in an evacuated desiccator with (tridecafluoro-1,1,2,2-tetra-hydrooctyl)dimethylchlorosilane (Gelest). A 40-μm-thick spacer was used to separate the silicon wafer from a coverslip that had been treated with an oxygen plasma for 3 minutes. The PDMS was cured in an oven at 95 ℃ for 20 minutes. After removing the silicon wafer, a razor blade was used to create a 5 mm × 5 mm well in the PDMS to expose the glass underneath it. The substrates were then treated overnight in an evacuated desiccator with (tridecafluoro-1,1,2,2-tetra-hydrooctyl)dimethylchlorosilane to prevent any silica microbeads from attaching to the glass surface during fabrication.

4.2.3 Photoinitiator synthesis

The water-soluble radical photoinitiator, sodium 4-[2-(4-morpholino)benzoyl-2-dimethylamino] butylbenzenesulfonate (MBS) was synthesized by modifying a literature procedure [46], as described previously [47]. As demonstrated by Kojima *et al.* [46], MBS has a broad absorption band with a peak at 325 nm and generates radicals when irradiated with UV light, giving it the ability to polymerize polyfunctional acrylate monomers. The use of MBS for MAP has not been reported previously, but MBS is a water-soluble variant of Irgacure 369, a photoinitiator that has been used widely for MAP [29]. The high solubility of MBS in water thus makes it a good candidate for MAP in aqueous media.

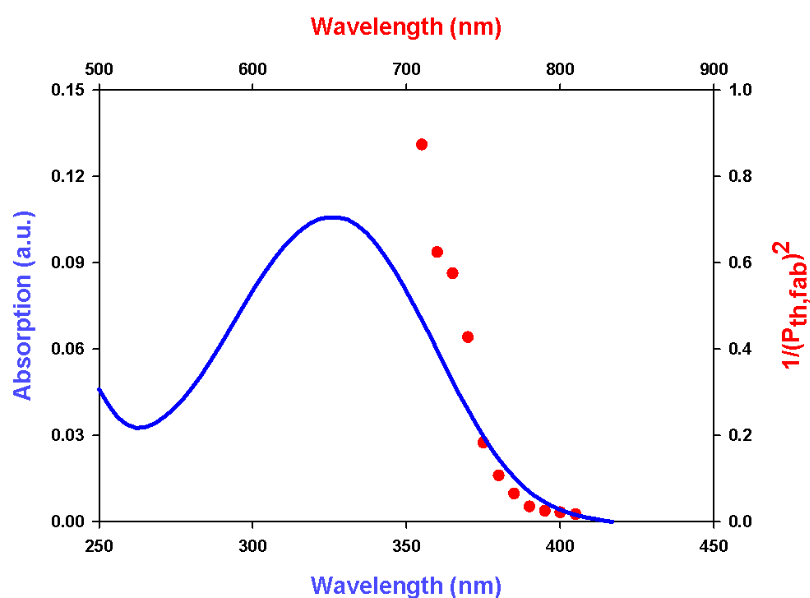

Figure 4.1 Absorption spectrum of MBS (solid line) and two photon polymerisation action spectrum of water-soluble acrylic photoresist containing 37.5 wt% ethoxylated-15 trimethylolpropane triacrylate and 1 wt% MBS in DI water (solid circles). Data for the polymerization action spectrum were collected by observing polymerization for 1 s exposures at 0 μm/sec. $P_{th,fab}$ is the threshold power measured at the sample required for polymerization.

The absorption spectrum of MBS was measured using a PerkinElmer Lambda 1050 UV/Vis/NIR spectrophotometer (PerkinElmer).

4.2.4 Water-soluble acrylic photoresist

Except where otherwise noted, the water-soluble photoresist was composed of 37.5 wt% ethoxylated(15) trimethylolpropane triacrylate (SR9035, Sartomer), 1 wt% MBS, and 61.5 wt% deionized (DI) water. This formulation is a negative-tone photoresist, i.e. polymerization takes place only where the photoresist is exposed to the laser beam. To incorporate silica microbeads into the photoresist, a solution containing 75 wt% SR 9035, 2 wt% MBS, and 23 wt% DI water was mixed with a solution containing 0.5 wt% of 5 μm diameter carboxyl-functionalized silica microbeads (Bangs Laboratories) in DI water in a 1:1 ratio. To vary the flexibility of the resulting polymers, Michael addition was performed on the acrylate monomers by adding 1 to 10 wt% diethanolamine (Sigma Aldrich) to the photoresist. To obtain fluorescent images of microwoven structures, 0.01 wt% Rhodamine B base (Acros Organics) was added to the acrylate monomer solution. Typical fabrication powers as measured at the sample were 4 mW for 3D structures, 7 mW for rigid threads and 5 mW for flexible threads. The processing window was a factor of nearly 5 at a fabrication velocity of 50 μm/sec.

Table 4.1 Physical properties of photoresist and photoinitiator

Refractive index of water-soluble acrylic photoresist	1.385
Density of water-soluble acrylic photoresist	1.05 g/mL
Viscosity of water-soluble acrylic photoresist	7.66 $\pm$0.02 cSt*
Solubility of MBS in 100 wt% DI water	0.638 $\pm$0.003 mol/L*
Solubility of MBS in 37.5 wt% ethoxylated-15 trimethylolpropane triacrylate and 62.5 wt% DI water	0.498 $\pm$0.067 mol/L*

*Values are reported to one standard deviation. Refractive index was measured using an ABBE-3L refractometer. Viscosity measurements were carried out using a 1C Ubbelohde viscometer at 25 ℃.

4.2.5 Biophotoresist

Solutions of bovine serum albumin (BSA) and MBS were prepared using methods similar to those in previous reports that used photosensitizers to crosslink proteins [37]. 400 mg/mL of BSA (Equitech-Bio) was prepared in 20 mM HEPES buffer (Sigma Aldrich) and MBS was added to the solution to obtain a total concentration of 10 to 15 mM. 0.25 wt% carboxyl-functionalized silica microbeads were introduced to the solution for optical trapping studies. Typical fabrication powers were 11 mW for both 3D structures and flexible threads. The processing window was greater than 2 at a fabrication velocity of 50 μm/sec.

4.2.6 Fabrication of free-standing microstructures

Free-standing microstructures were fabricated on acrylate-functionalized coverslips using an acrylate monomer resin that consisted of 54 wt% dipentaerythritol pentaacrylate (SR399, Sartomer), 43 wt% tris(2-hydroxyethyl) isocyanurate triacrylate (SR368, Sartomer), and 3 wt% Lucirin TPO-L (BASF) according to previously reported methods [48].

4.2.7 Fabrication and development of structures with water-soluble photoresist

A small amount of photoresist was placed on a coverslip (that could include previously fabricated free-standing structures), covered with a fluorinated substrate, and mounted on a *xyz* piezoelectric stage (Physik Instrumente). The movement and positioning of the substrate were controlled by programs written in LabView (National Instruments). Once fabrication was complete, any unexposed photoresist was removed by rinsing the substrates in ethanol and hexanes (acrylic photoresist) or HEPES buffer (biophotoresist). The final structures were examined by collecting scanning electron micrographs (SEMs) on a Hitachi SU-70. Samples for SEM analysis were prepared by sputter-coating approximately 10 nm of palladium/ platinum.

4.2.8 Simultaneous optical trapping and fabrication

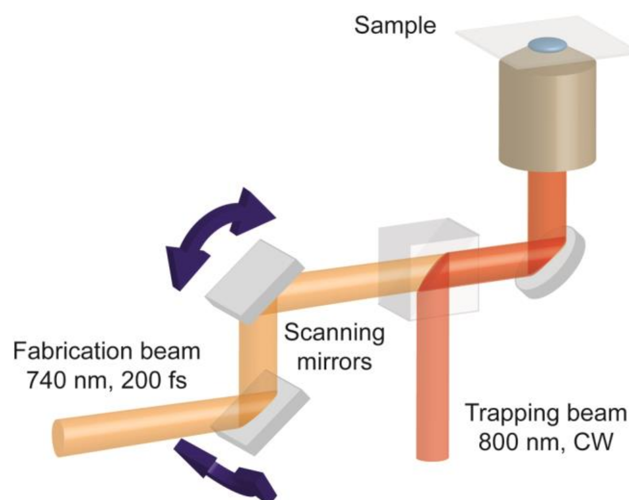

Figure 4.2 Schematic diagram of the experimental setup for simultaneous optical trapping and MAP.

A schematic diagram of our experimental setup is shown in Figure 4.2. For optical trapping in conjunction with MAP, two Ti:sapphire lasers (Coherent Mira 900-F) were used. Optical trapping was performed using a continuous-wave (CW) laser tuned to 800 nm and MAP was carried out using 200 fs pulses from a modelocked laser tuned to 740 nm. The two beams were of orthogonal polarizations and were merged together in a polarizing beam cube before being introduced into an inverted microscope (Zeiss Axiovert 100) and focused into the sample through a 1.45 NA, 100× oil-immersion microscope objective (Zeiss α Plan-FLUAR). Galvanometric scanning mirrors were used to move one laser beam relative to the other. The ability to control the laser beams independently permits the fabrication of unsupported structures within the liquid photoresist. Due to the unsupported nature of the structures, this scheme allows for the facile manipulation and transport of structures from the initial point of fabrication to other points of interest.

4.2.9 Two-photon fluorescence imaging

Two-photon fluorescence images were obtained by scanning the laser beam using galvanometric mirrors. The fluorescence signals were collected by a single-photon-counting avalanche photodiode (EG&G) and transferred to a computer. The fluorescence data processing was carried out using programs written in LabView.

4.3 Results and discussion

4.3.1 MAP and optical tweezers for constructing two- and three-dimensional structures

Because our photoresist is water based, it allows silica microbeads to be trapped with ease for precise positioning, while the polymer that is formed acts as a binding agent that can spot-weld microbeads to the substrate, to another microbead, or to any other microstructure. To demonstrate this capability, we first fabricated 2D structures, as shown in Figure 4.3. The letter “M” was fabricated with the water-soluble photoresist. The letters “U” and “D” were constructed by the controlled assembly of silica microbeads. Each microbead was delivered to the desired location using optical tweezers and then was secured to the surface by MAP. Since both laser beams were carefully overlapped in the plane of the sample surface, the resulting polymerization took place below the center of the trapped microbead. Also, since the polymerization is limited to the focal volume of the laser beam the silica beads could be immobilized by a small amount of polymer. Post-development imaging of the sample showed that the polymer structure maintained its overall morphology with minimal shrinkage and that the silica microbeads were well adhered to the surface.

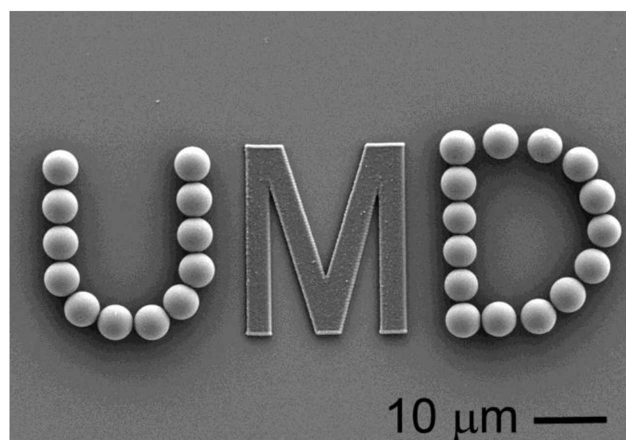

Figure 4.3 The letter “M” was created from the aqueous photoresist using MAP, while the letters “U” and “D” were created by manipulation of microbeads using optical tweezers followed by immobilization with MAP.

4.3.2 3-D structures consisting of silica microbeads

A combination of optical tweezers and MAP can also be applied to the construction of 3D structures consisting of immobilized silica microbeads. We fabricated structures consisting of three layers of microbeads as shown in Figures 4.4(A) and 4.4(B). Both structures were assembled following a step-by-step process in which each silica microbead was moved to a position of interest using optical tweezers, starting with the lowest layer. In the pyramid in Figure 4.4(A), the microbeads on higher levels were placed so as to form a close-packed arrangement in which there was optimal contact of a microbead with the three neighboring beads in the previous layer to allow for better “welding” by means of polymerization. On the other hand, in the 3×3 cube depicted in Figure 4.4(B), each particle contacts only one microbead in the previous layer, but the overall form of the structure is still maintained. This structure demonstrates the robust nature of the water-soluble photoresist after exposure and development. The confined polymerization made possible by MAP restricts the size of each polymer feature to a fraction of the size of

the microbead, and therefore no polymer is visible on the exteriors of the structures shown in Figures 4.4(A) and 4.4(B).

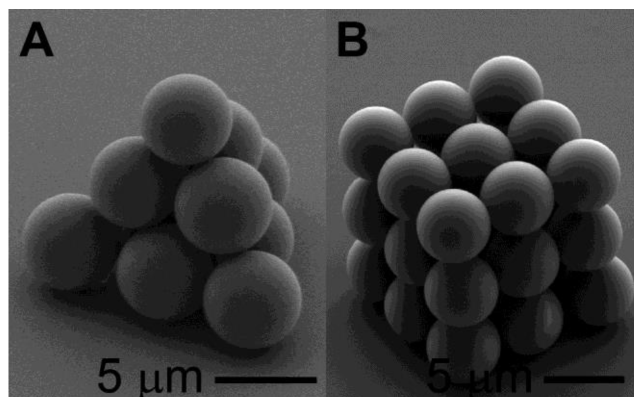

Figure 4.4 Silica microbead pyramid (A) and cube (B) created by optical trapping of individual beads followed by immobilization with MAP.

4.3.3 Structures consisting of silica microbeads and acrylic polymer features

The low refractive index of the photoresist allows for optical trapping of silica microbeads while fabricating polymer microthreads attached to them, as well as for trapping of the ends of the microthreads. Unsupported structures were fabricated using two methods. In Method I, a silica microbead or small polymer particle is trapped with optical tweezers within the liquid photoresist and fabrication is carried out with the second laser via galvanometric scanning mirrors (Figure 4.5).

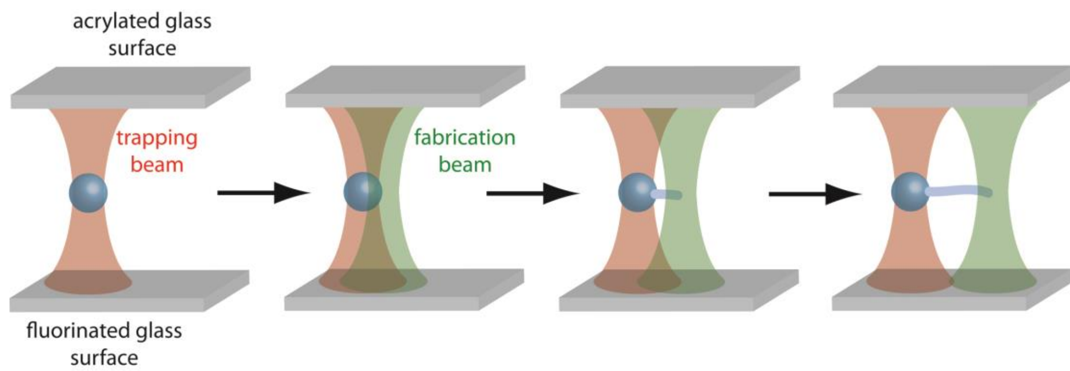

Figure 4.5 Schematic representation of Method I for creating microthreads attached to microbeads. A microbead is optically trapped, and then the fabrication beam is focused at one of its edges and moved horizontally to create a thread.

Because the initial fabrication point is tethered to a microbead that is trapped with optical tweezers, the second laser can freely fabricate within the liquid medium with no interference from the optical tweezers. The polymerized volume element (voxel) is elongated along the direction of laser propagation [29], so this technique is ideal for fabricating tape-like, lengthy, flexible structures parallel to the sample surface.

To demonstrate Method I, we fabricated a structure designed to mimic a tetherball and pole, in which a flexible microthread fabricated with the water-soluble photoresist was wrapped around a pre-fabricated post. A schematic diagram of the fabrication method is shown in Figure 4.6(A). The post structures were fabricated first, and the water-based photoresist was added to the sample to fabricate the microthreads via Method I. Here, a more flexible microthread was fabricated by controlling the laser power and sample velocity during the fabrication process. Translating the focal point of the laser beam at a higher velocity results in a thinner and less stiff thread due to the reduced exposure at each point. Once a flexible microthread had been fabricated on a silica microbead, the free end of the thread was

optically trapped and secured to the top of the post via MAP. The bead was then optically trapped and maneuvered to wrap the microthread around the post. When the thread was completely wrapped around the post, the bead was positioned onto one side of the post and fastened by creating a small amount of polymer between the bead and the post. SEM images of two representative tetherball pole structures are shown in Figures 4.6(B) and 4.6(C).

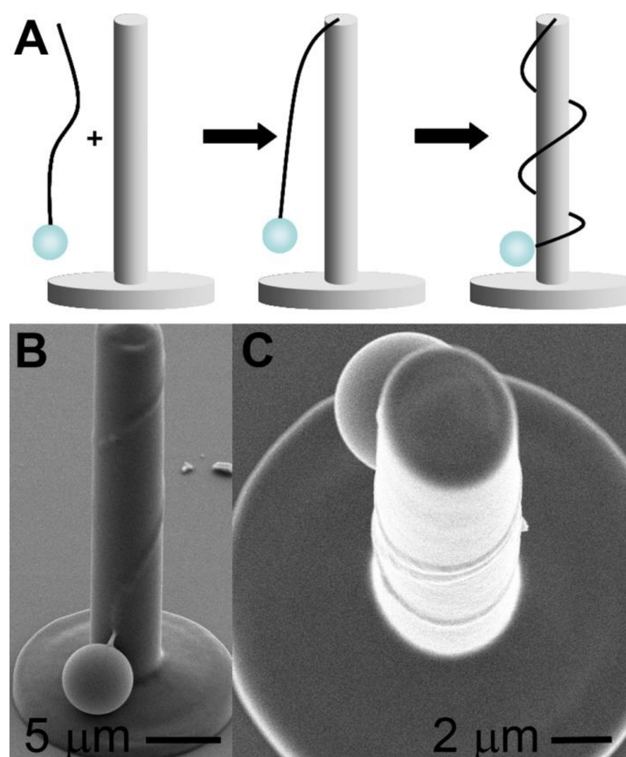

Figure 4.6 (A) Fabrication scheme for a microscale tetherball pole. A microthread is fabricated from a microbead using Method I. Optical tweezers are used to bring the end of the thread to the top of the pole, where it is attached via MAP. The optical tweezers are then used to wrap the thread around the pole, after which the bead is immobilized using MAP. (B) and (C) are views of two representative structures.

Method II also employs a silica microbead as the initial point of fabrication (Figure 4.7). In this method, a microbead is first trapped and positioned within 1 to 2

μm of the fluorinated substrate. The microbead is positioned in this manner so that when it is released from the optical trap, it remains close to its original position as its travel distance is limited due to gravitational influence. Fabrication begins simultaneously with the release of the optical trap. Because there is more voxel overlap along the elongated direction, this technique is ideal for the fabrication of less flexible threads in the direction normal to the sample surface.

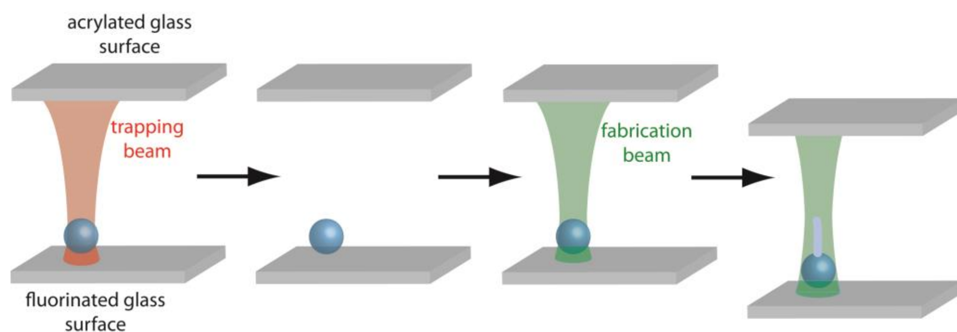

Figure 4.7 Schematic representation of Method II for creating microthreads attached to microbeads. A microbead is optically trapped near the bottom surface of the sample cell. The trapping beam is turned off, and then the fabrication beam is focused at the top of the bead. The sample is lowered to create a vertical microthread.

To demonstrate Method II we used MAP to fabricate a free-standing structure resembling the eye of a sewing needle and then threaded it using optical tweezers. A schematic diagram of the process used is shown in Figure 4.8(A). Once the needle eye had been fabricated and developed, the water-based photoresist was introduced to the sample. A 15 μm microthread was then fabricated attached to an optically trapped silica microbead. In this example, the microthread was fabricated in the direction orthogonal to the sample surface. The polymeric end of the microthread was then optically trapped and passed through the eye of the needle structure. The diameter of

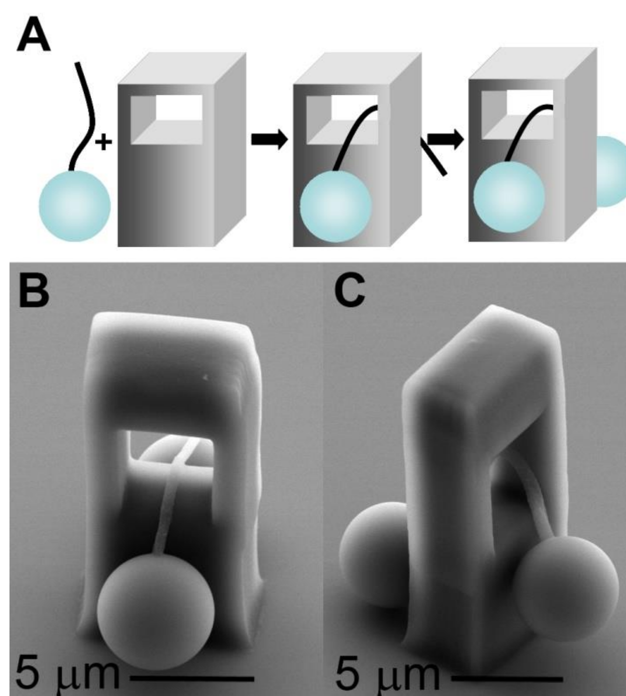

Figure 4.8 (A) Fabrication scheme for a microscale needle eye. A microthread is fabricated on a microbead using Method II. Optical tweezers are used to bring the end of the thread through the eye of the needle, after which a second microbead is attached via MAP. Panels (B) and (C) show two views of the resultant structure.

the microbead was larger than the eye of the needle, which held the thread in place. To prevent the microthread from being released during the development process, another silica microbead was positioned on the free end of the thread using optical tweezers and secured with a small amount of polymer via MAP. SEM views of the final structure are shown in Figures 4.8(B) and 4.8(C).

We have also used Method II to assemble structures consisting solely of microthreads and silica microbeads. Figure 4.9 shows a microbraid composed of three microthreads with circular cross sections. To create such threads, fabrication must be carried out normal to the sample surface. However, threads created in this manner are generally relatively stiff. This effect is due to the elongation of the voxel in the

direction normal to the sample surface and possibly also to optical waveguiding in microthreads as they are fabricated. Due to the inflexible nature of these rope-like microthreads, they do not work well for braiding. To overcome this problem, prior to fabrication we added 10 wt% of diethanolamine to the photoresist to tie up some of the acrylate groups via Michael addition [44, 45]. This process decreases the amount of crosslinking among the acrylate groups during photopolymerization, resulting in a more elastic polymer that yields flexible microthreads.

To construct a microbraid, three flexible microthreads were created and the polymeric ends were attached to the acrylate-functionalized surface. The silica microbeads were then optically trapped one by one, and were manipulated around one another to construct a microbraid. Once the braiding was completed, the beads were attached to the acrylate-functionalized surface with MAP so as to maintain the overall structure during the development process.

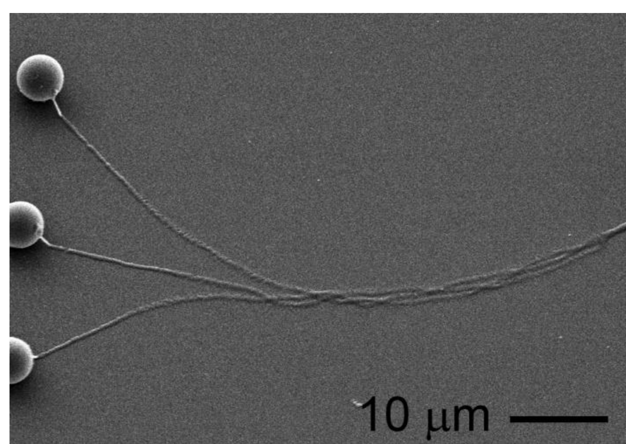

Figure 4.9 Microthreads created with MAP and braided using optical tweezers.

4.3.4 Biomolecular materials

To establish the versatility of MBS as a water-soluble radical photoinitiator, its use was extended to multiphoton fabrication with biomolecular materials. Figure 4.10

shows a maze and a pyramid that were fabricated using BSA and 10 mM MBS. While microstructures of this nature have been fabricated previously by other groups using photosensitizers [34, 35, 37]. to our knowledge ours is the first demonstration of the use of a water-soluble radical photoinitiator for this process. Unlike the photosensitizers that have been typically used to crosslink biomolecular materials, when exposed to light, MBS decomposes into small fragments that can more easily be washed away during the development process. The resultant photofragments absorb light at considerably shorter wavelengths than the parent molecule, reducing any

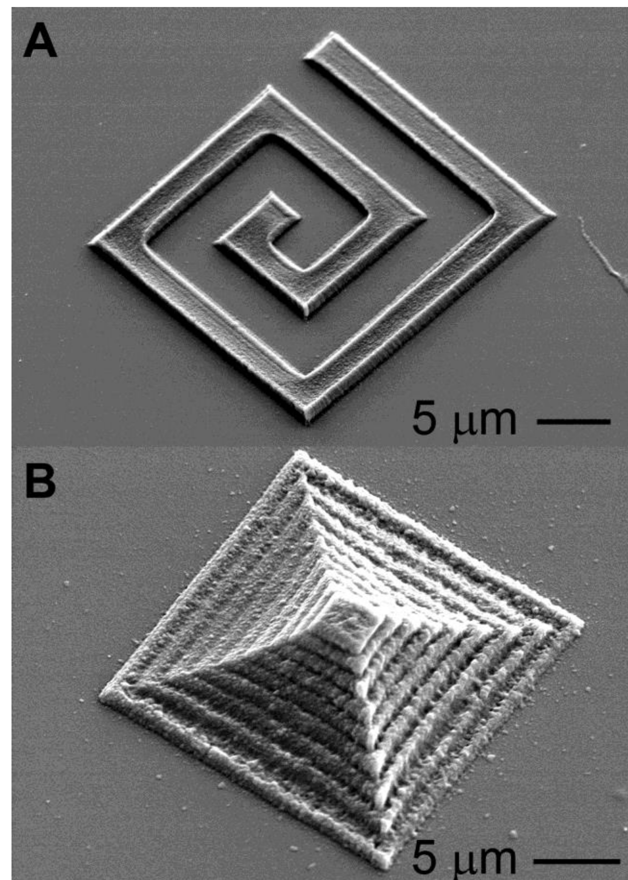

Figure 4.10 (A) Maze and (B) pyramid created by radical crosslinking of BSA.

residual photoactivity. These features, along with the relatively low cost of MBS when compared to purely biocompatible photosensitizers such as flavin adenine dinucleotide, makes MBS an attractive candidate for the photocrosslinking of

biological materials.

In Figure 4.11 we show cross-sectional fluorescence images of a structure created by microweaving of threads created with the acrylic photoresist and threads created with the biophotoresist. To carry out microweaving, free-standing posts were first fabricated on an acrylate-functionalized coverslip. These posts were fabricated along the edges of a 50 μm × 50 μm square to serve as tethering points for the microthreads. First, an acrylate monomer solution containing Rhodamine B base was introduced into the sample. A 50 μm acrylic microthread was fabricated from a microbead in the direction normal to the sample surface and the ends of the microthread were positioned and fixed onto posts that were on opposing edges of the square. Rigid microthreads were fabricated so that they would maintain their structure during the development process. Two more microthreads were then fabricated and fixed parallel to the first. The sample was developed in ethanol and then immersed in a 20 vol% solution of diethanolamine in ethanol for 15 minutes to react with any unreacted acrylate groups so as to prevent the BSA microthreads from attaching to the acrylic microthreads during the weaving process. The sample was developed in ethanol and hexanes before the biophotoresist was introduced to the sample to carry out weaving. 65-μm-long, flexible BSA microthreads attached to silica microbeads were fabricated parallel to the sample surface. The weaving process was carried out by optical trapping of the silica microbeads. Both ends of the flexible microthreads were then fixed onto posts on opposing ends of the 50 μm × 50 μm square. Once multiple flexible threads were woven, fluorescence images were collected by scanning the laser beam over the entire sample. As Figure 4.11 shows, the rigid microthreads with Rhodamine B base appear brighter than the BSA microthreads, which contain no fluorescent agent. Also, alternating junctions between microthreads

show brighter fluorescence, which reveals the weaving pattern as each alternating junction has a fluorescent acrylic microthread woven below the non-fluorescent BSA microthread and therefore in the same plane as detected by the photodiode.

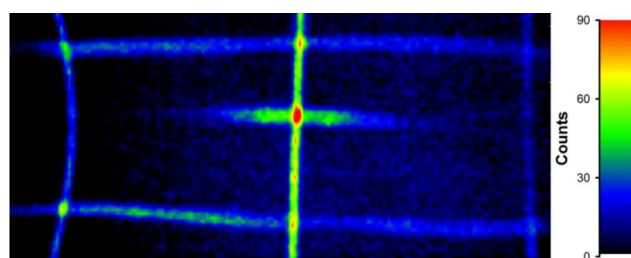

Figure 4.11 Background-subtracted, cross-sectional two-photon fluorescence intensity image of microwoven threads of acrylic polymer (vertical) and BSA (horizontal). The focal plane is on the top edge of the woven structure so that the junctions in which the dye-infused acrylic threads pass over the BSA threads are brighter than the junctions in which they pass under the BSA threads.

4.4 Conclusions

By combining MAP and optical tweezers, we have developed a suite of simple techniques that allow for precise control over the fabrication, manipulation, and positioning of microstructures in aqueous media. We have demonstrated the versatility of MBS for the photocrosslinking of acrylic monomers and proteins in aqueous solution. These materials and techniques open the door to employing fabrication methods, such as microbraiding and microweaving, that are not possible using other direct-write methods. The new capabilities afforded by the combination of MAP and optical tweezers will have many microsystems applications in chemical and biological sciences and engineering, and beyond.

References

[1] J. El-Ali, P. K. Sorger and K. F. Jensen, "Cells on chips," *Nature*, vol. 442, pp. 403-411, 2006.

[2] J. E. Keymer, P. Galajda, C. Muldoon, S. Park and R. H. Austin, "Bacterial metapopulations in nanofabricated landscapes," *Proc. Nat. Acad. Sci. USA*, vol. 103, pp. 17290-17295, 2006.

[3] E. Livak-Dahl, I. Sinn and M. Burns, "Microfluidic chemical analysis systems," *Annu. Rev. Chem. Biomol. Eng.*, vol. 2, pp. 325-353, 2011.

[4] G. M. Whitesides, "The origins and future of microfluidics," *Nature*, vol. 442, pp. 368-373, 2006.

[5] G. M. Whitesides and A. D. Stroock, "Flexible methods for microfluidics," *Phys. Today*, vol. 54, pp. 42-48, 2001.

[6] R. V. Bellamkonda, "Peripheral nerve regeneration: An opinion on channels, scaffolds and anisotropy," *Biomater.*, vol. 27, pp. 3515-3518, 2006.

[7] A. Reiser, *Photoreactive polymers:the science and technology of resists*, Wiley, New York, 1989.

[8] J.-P. Fouassier, *photoinitiation, photopolymerization and photocuring: fundamentals and applications*, Hanser Publishers, Munich, 1995.

[9] A. Ashkin, J. M. Dziedzic, J. E. Bjorkholm and S. Chu, "Observation of a single-beam gradient force optical trap for dielectric particles," *Opt. Lett.*, vol. 11, pp. 288-290, 1986.

[10] S. M. Block, "Making light work with optical tweezers," *Nature*, vol. 360, pp. 493-495, 1992.

[11] D. G. Grier, "A revolution in optical manipulation," *Nature*, vol. 424, pp. 810-816, 2003.

[12] K. Dholakia and P. Reece, "Optical micromanipulation takes hold," *Nano Today*, vol. 1, pp. 18-27, 2006.

[13] A. Jonas and P. Zemanek, "Light at work: the use of optical forces for particle manipulation, sorting and analysis," *Electrophor.*, vol. 29, pp. 4813-4851, 2008.

[14] K. Ladavac, K. Kasza and D. G. Grier, "Sorting mesoscopic objects with periodic potential landscapes: Optical fractionation," *Phys. Rev. E*, vol.70, pp. 010901, 2004.

[15] M. P. MacDonald, L. Paterson, K. Volke-Sepulveda, J. Arlt, W. Sibbett and K. Dholakia, "Creation and enhanced manipulation of 3-dimensional optically trapped structures," *Science*, vol. 296, pp. 1101-1103, 2002.

[16] P. Galajda and P. Ormos, "Complex micromachines produced and driven by light," *Appl. Phys. Lett.*, vol. 78, pp. 249-251, 2001.

[17] S. Maruo, K. Ikuta and H. Korogi, "Force-controllable, optically driven micromachines fabricated by single-step two-photon microstereolithography," *J. Microelectromech. Syst.*, vol. 12, pp. 533-539, 2003.

[18] S. Maruo, A. Takaura and Y. Saito, "Optically driven micropump with a twin spiral microrotor," *Opt. Express*, vol. 17, pp. 18525-18532, 2009.

[19] J. T. Finer, R. M. Simmons and J. A. Spudich, "Single myosin molecule mechanics: piconewton forces and nanometre steps," *Nature*, vol. 368, pp. 113-119, 1994.

[20] A. D. Mehta, M. Rief, J. A. Spudich, D. A. Smith and R. M. Simmons, "Single-molecule biomechanics with optical methods," *Science*, vol. 283, pp. 1689-1695, 1999.

[21] K. Svoboda, P. P. Mitra and S. M. Block, "Fluctuation analysis of kinesin movement," *Proc. Nat. Acad. Sci. USA*, vol. 91, pp. 11782-11786, 1994.

[22] K. Svoboda, C. F. Schmidt, B. J. Schnapp and S. M. Block, "Direct observation of kinesin stepping by optical trapping interferometry," *Nature*, vol. 365, pp. 721-727, 1993.

[23] R. E. Holmlin, M. Schiavoni, C. Y. Chen, S. P. Smith, M. G. Prentiss and G. M. Whitesides, "Light-driven microfabrication: assembly of multicomponent, three-dimensional structures by using optical tweezers," *Angew. Chem. Int. Ed.*, vol. 39, pp. 3503-3506, 2000.

[24] A. Terray, J. Oakey and D. W. M. Marr, "Fabrication of linear colloidal structures for microfluidic applications," *Appl. Phys. Lett.*, vol. 81, pp. 1555-1557, 2002.

[25] A. Terray, J. Oakey and D. W. M. Marr, "Microfluidic control using colloidal devices," *Science,* vol. 296, pp. 1841-1844, 2002.

[26] E. McLeod and C. B. Arnold, "Subwavelength direct-write nanopatterning using optically trapped microspheres," *Nature Nanotech.*, vol. 3, pp. 413-417, 2008.

[27] E. McLeod and C. B. Arnold, "Array-based optical nanolithography using optically trapped microlenses," *Opt. Express*, vol. 17, pp. 3640-3650, 2009.

[28] S. Kawata, H. B. Sun, T. Tanaka and K. Takada, "Finer features for functional micro- devices," *Nature*, vol. 412, pp. 697-698, 2001.

[29] C. N. LaFratta, J. T. Fourkas, T. Baldacchini and R. A. Farrer, “Multiphoton fabrication,” *Angew. Chem. Int. Ed.*, vol. 46, pp. 6238-6258, 2007.

[30] S. Maruo and J. T. Fourkas, "Recent progress in multiphoton microfabrication," *Laser Photon. Rev.*, vol. 2, pp. 100-111, 2008.

[31] D. Yang, S. J. Jhaveri and C. K. Ober, "Three-dimensional microfabrication by Two-Photon Lithography," *MRS Bull.*, vol. 30, pp. 976-982, 2005.

[32] J. T. Fourkas, “Nanoscale photolithography with visible light,” *J. Phys. Chem. Lett.*, vol. 1, pp. 1221-1227, 2010.

[33] J.-F. Xing, X.-Z. Dong, W.-Q. Chen, X.-M. Duan, N. Takeyasu, T. Tanaka and S. Kawata, “Improving spatial resolution of two-photon microfabrication by using photoinitiator with high initiating efficiency,” *Appl. Phys. Lett.*, vol. 90, pp. 131106, 2007

[34] S. Basu and P. J. Campagnola, "Properties of crosslinked protein matrices for tissue engineering applications synthesized by multiphoton excitation," *J. Biomed. Mater. Res. A*, vol. 71A, pp. 359-368, 2004.

[35] S. Basu, L. P. Cunningham, G. D. Pins, K. A. Bush, R. Taboada, A. R. Howell, J. Wang and P. J. Campagnola, "Multiphoton excited fabrication of collagen matrixes cross-linked by a modified benzophenone dimer: bioactivity and enzymatic degradation," *Biomacromol.*, vol. 6, pp. 1465-1474, 2005.

[36] S. Basu, C. W. Wolgemuth and P. J. Campagnola, "Measurement of normal and anomalous diffusion of dyes within protein structures fabricated *via* multiphoton excited cross-linking," *Biomacromol.*, vol. 5, pp. 2347-2357, 2004.

[37] R. T. Hill, J. L. Lyon, R. Allen, K. J. Stevenson and J. B. Shear, "Microfabrication of three-dimensional bioelectronic architectures," *J. Amer. Chem. Soc.*, vol. 127, pp. 10707-10711, 2005.

[38] B. Kaehr, R. Allen, D. J. Javier, J. Currie and J. B. Shear, "Guiding neuronal development with in situ microfabrication," *Proc. Nat. Acad. Sci.* USA, vol. 101, pp. 16104-16108, 2004.

[39] B. Kaehr and J. B. Shear, "Mask-directed multiphoton lithography," *J. Amer. Chem. Soc.*, vol. 129, pp. 1904-1905, 2007.

[40] A. Berg, R. Wyrwa, J. Weisser, T. Weiss, R. Schade, G. Hildebrand, K. Liefeith, B. Schneider, R. Ellinger and M. Schnabelrauch, "Synthesis of photopolymerizable hydrophilic macromers and evaluation of their applicability as reactive resin components for the fabrication of three-dimensionally structured hydrogel matrices by 2-photon-polymerization," *Adv. Eng. Mater.*, vol. 13, pp. B274-B284, 2011.

[41] L. Grimm, K. J. Hilke and E. Scharrer, "The mechanism of the cross linking of poly(vinyl alcohol) by ammonium dichromate with U.V. light," *J. Electrochem. Soc.*, vol. 130, pp. 1767-1771, 1983.

[42] A. Chemtob, B. Kunstler, C. Croutxe-Barghorn and S. Fouchard, "Photoinduced miniemulsion polymerization," *Colloid Polymer Sci.*, vol. 288, pp. 579-587, 2010.

[43] S. J. Jhaveri, J. D. McMullen, R. Sijbesma, L.-S. Tan, W. Zipfel and C. K. Ober, "Direct three-dimensional microfabrication of hydrogels via two-photon lithography in aqueous solution," *Chem. Mater.*, vol. 21, pp. 2003-2006, 2009.

[44] B. D. Mather, K. Viswanathan, K. M. Miller and T. E. Long, "Michael addition reactions in macromolecular design for emerging technologies," *Prog. Polymer Sci.*, vol. 31, pp. 487-531, 2006.

[45] L. Li, M. Driscoll, G. Kumi, R. Hernandez, K. J. Gaskell, W. Losert and J. T. Fourkas, "Binary and gray-scale patterning of chemical functionality on polymer films," *J. Amer. Chem. Soc.*, vol. 130, pp. 13512-13513, 2008.

[46] K. Kojima, M. Ito, H. Morishita and N. Hayashi, "Thioxanthone based water-soluble photoinitiators for acrylamide photopolymerization," *Chem. Mater.*, vol. 10, pp. 3429-3433, 1998.

[47] C. Ropp, Z. Cummins, R. Probst, S. Qin, J. T. Fourkas, B. Shapiro and E. Waks, "Positioning and immobilization of individual quantum dots with nanoscale precision," *Nano Lett.*, vol. 10, pp. 4673-4679, 2010.

[48] T. Baldacchini, C. N. LaFratta, R. A. Farrer, M. C. Teich, B. E. A. Saleh, M. J. Naughton and J. T. Fourkas, "Acrylic-based resin with favorable properties for three-dimensional two-photon polymerization," *J. Appl. Phys.*, vol. 95, pp. 6072-6076, 2004.

Chapter 5: Reactive-Ion-Etched Nanograss Fabricated using MAP and UV Exposure

5.1 Introduction

A superhydrophobic surface is one with a contact angle (CA) larger than 150 ° for a water droplet, as shown in Figures 5.1(a) and (b). Two of the most well-known examples of natural superhydrophobic surfaces are lotus leaves and a butterfly wings. The mystery of their superhydrophobicity has been unraveled since the development of SEM. Figure 5.1(c) illustrates the multiple rough, raised points on the lotus leaf, and Figure 5.1(d) shows the complex microstructure of a butterfly's wing. The current consensus is that the combination of roughness and a low surface-free-energy material provides a superhydrophobic surface with a large CA. However, low surface free energy is not necessary to build up superhydrophobic structures, whereas the hierarchical roughness is required for the superhydrophobicity. Based on these facts, many artificial, biomimetic superhydrophobic materials have been fabricated [1-8], and have attained performance that is comparable with that of natural materials.

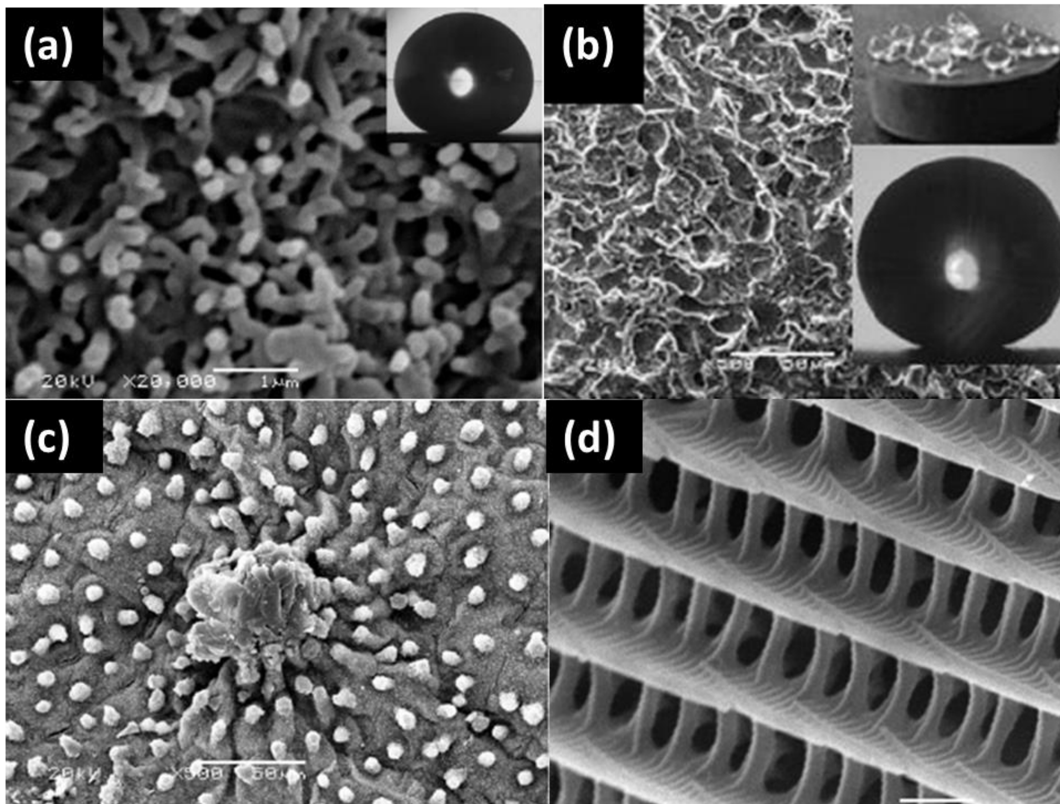

Figure 5.1. (a) An SEM image of a lotus leaf. The inset is a water droplet on the leaf. Its CA is 162 ° [9]. (b) An SEM image of etched steel treated with fluoroalkylsilane; this surface exhibits superhydrophobicity [9]. (c) An SEM image of the rough projections on the lotus leaf [9]. (d) The microstructure of a butterfly's wing [10].

Superhydrophobic coatings are useful for improving safety as well as efficiency for industrial applications, and also for extending equipment lifetime. Superhydrophobic materials have drawn significant attention for various applications, such as preventing the corrosion of bridges, pipes and ships. They are used to make surfaces self-cleaning [11], anti-icing [12], anti-fouling [13], anti-condensing [14], anti-friction [15] and anti-clotting [16]. They are also used for the applications such as mildew and mold resistance [17], sealants [18], electronics [19], and evaporative desalination [20]. An example of anti-icing and anti-corrosion capabilities is shown in Figure 5.2.

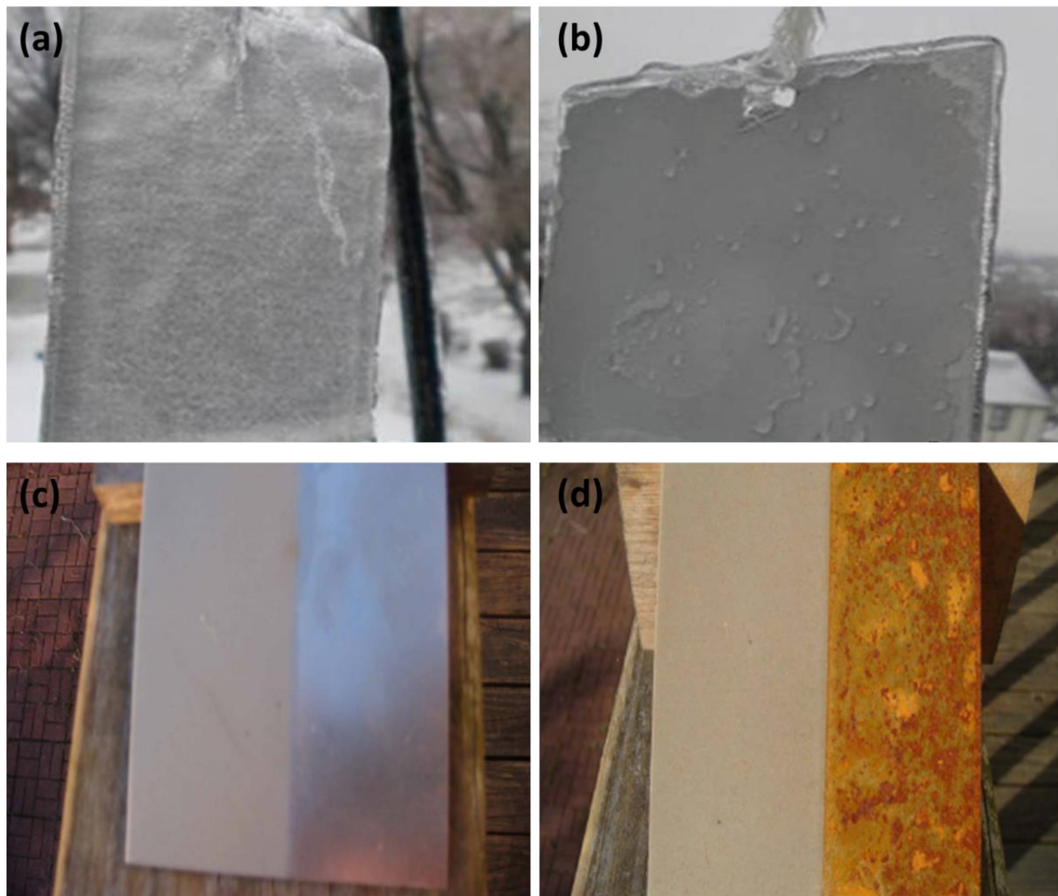

Figure 5.2. (a) and (b) A superhydrophobic anti-icing coating in a freezing rain. (a) The uncoated side of an aluminum plate is completely covered by ice. (b) The coated side of the aluminum plate has little ice [21]. (c) and (d) A 4” square steel plate on Day 1 and Day 60. The right side of the plate is uncoated, while the left side was treated with a modified SH coating [22].

Various techniques have had great success in creating rough surfaces that are superhydrophobic. These techniques include electrochemical deposition [23–26], plasma etching [27–30], hydrothermal reaction [31–34], crystallization control [35–37], self-assembly [38–42], sol-gel fabrication [43–47], and lithography [2]. Man-made superhydrophobic materials have some additional properties that natural materials do not, such as reversibility [49–51], transparency [52], tunability [28], electrowetability [53], conductivity [25], and high adhesion [54].

We have developed a new method to fabricate hydrophobic/superhydrophobic surfaces from acrylic polymers using MAP/UV exposure and reactive-ion etching (RIE). This technique is simple and quick, and can be applied to a large variety of photoresists. MAP-fabricated and UV-cured photoresists are treated with RIE for 10 minutes, to attain a hydrophobic surface. This method has some unique advantages.

1. The use of MAP allows for the fabrication of complex micro-scale hydrophobic patterns and arbitrary three-dimensional hydrophobic microstructures on many types of substrates, such as glass, polymers, and plastics.
2. Hydrophobic and hydrophilic patterns can be achieved on a single substrate using two different paths. One path is to fabricate desired patterns, treat them with RIE, and selectively functionalize either the microstructure or the substrate to obtain a hydrophobic pattern on a hydrophilic substrate (or vice versa). The other path is to etch the MAP-fabricated structure to obtain a hydrophobic pattern. Another layer of micro-structure can be created on top of this pattern using MAP, and then functionalized to achieve hydrophilicity.
3. MAP, as a mask-free fabrication technique, enables free design and requires a relatively small instrumental investment (as discussed in Chapter 1), which adds versatility and enables low-cost superhydrophobic material fabrication.
4. Molding can extend this approach to large scale structures, while MAP requires significant time to create patterns over large area. Molding and replication can be implemented to enable the mass production and improve efficiency.

In the ensuing sections of this chapter, preliminary results will be presented. Future work is discussed in Chapter 6.

5.2 Experiments and Results

5.2.1 RIE-treated MAP-fabricated acrylic film

The MAP setup and sample preparation have been discussed in Chapters 1 and 2, and thus will not be detailed here. In RIE, plasma is generated inside a parallel-plate reactor. The two plates are electrodes that accelerate the ions towards the sample. The plasma contains ions that perform isotropic physical etching, as well as activated neutrals that enhance the chemical reaction. In our process, the gas used for RIE contained O_2 (5 sccm) and CHF_3 (15 sccm). The radio frequency (RF) power used to generate the plasma was 150 W, the pressure was 50 mTorr and the etch time was 10 minutes. Originally, we etched a MAP-fabricated acrylic waveguide using RIE with the goal of changing its height. Instead of reduced height, we observed the formation of a nanograss, as shown in Figure 5.3.

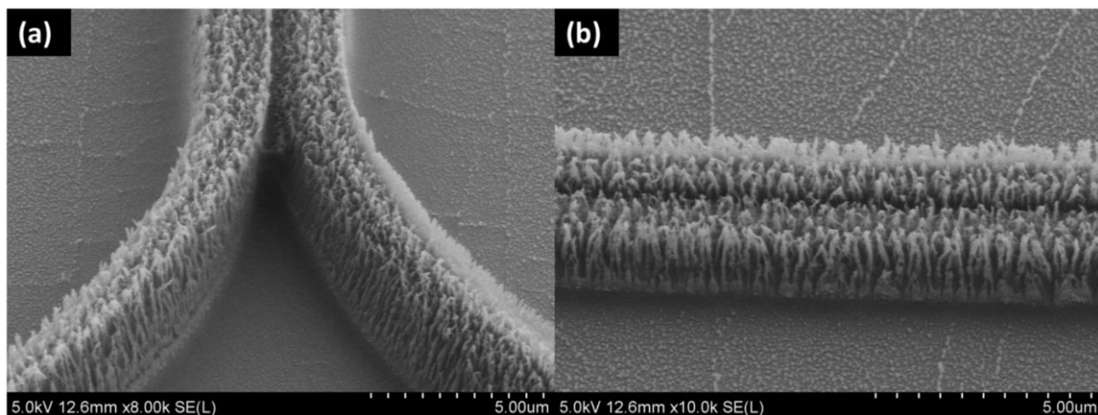

Figure 5.3. An acrylic waveguide fabricated using MAP was etched for 10 min with RIE, forming this nanograss.

To understand the mechanism of nanograss formation, different fabrication velocities were used to create the acrylic films. MAP fabrication is a point-by-point technique. To figure out whether the nanograsses are related to the basic building blocks in MAP (voxels), UV-cured polymeric films were also treated with RIE and

examined using SEM. Different etch angles were used to investigate the interplay between microscopic polymer anisotropy and the nanograss structure.

5.2.2 Velocity of MAP

During MAP fabrication, the exposure time can be adjusted by changing the fabrication velocity. A longer exposure time activates more photoinitiator, thereby generating a higher density of radicals. The polymer will therefore have a higher crosslinking ratio at higher exposures. The higher the cross-linking within a polymer, the more resistant that polymer is to the etching, all other things being equal. In our experiments, we kept the laser intensity constant at 6 mW at the sample and compared different velocities: high speed (50 μm/sec), medium speed (10 μm/sec, which is our typical fabrication speed) and low speed (2 μm/sec). The acrylic resin was composed of 54 wt% dipentaerythritol pentaacrylate (Sartomer) and 43 wt% tris (2-hydroxy ethyl) isocyanurate triacrylate (Sartomer), with 3 wt% Lucirin TPO-L (BASF) as the photoinitiator. The resultant patterns were etched for 10 minutes, using the same conditions as in section 5.2.1. The SEM images of nanograss obtained using these speeds are shown in Figures 5.4, 5.5 and 5.6.

Compared to the medium speed sample (in Figure 5.5), the high-speed sample (Figure 5.4) has a lower density of nanograss, and the size of each nanograss “blade” is smaller with less of the grainy polymer residual re-deposited on the top.

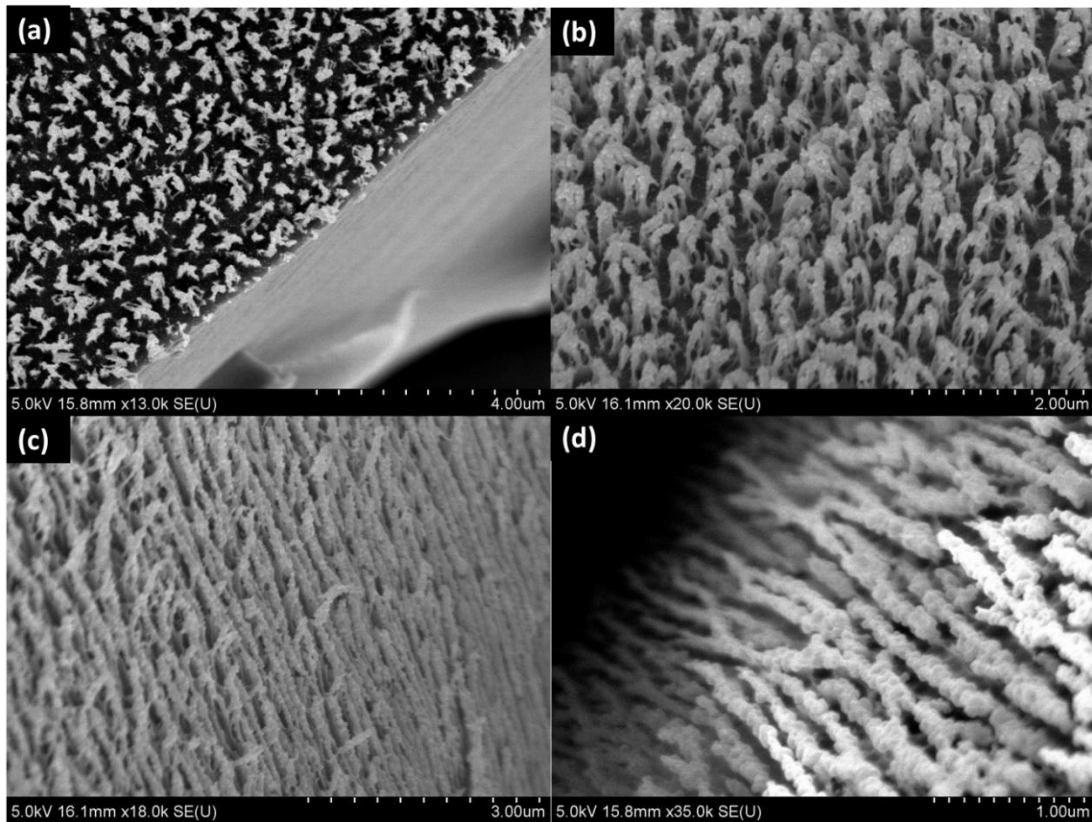

Figure 5.4. (a) - (d) SEM images of RIE-treated MAP (high speed)-fabricated acrylic film. (a) and (b) SEM images of the top of the nanograss; (c) and (d) SEM images of the side-walls.

The medium-speed nanograss (Figure 5.5) has larger and more dense blades compared to the high-speed sample. The nanograss blades tend to aggregate to form clusters. The top surface of the nanograss is grainy and rough, which makes it a good candidate for superhydrophobicity.

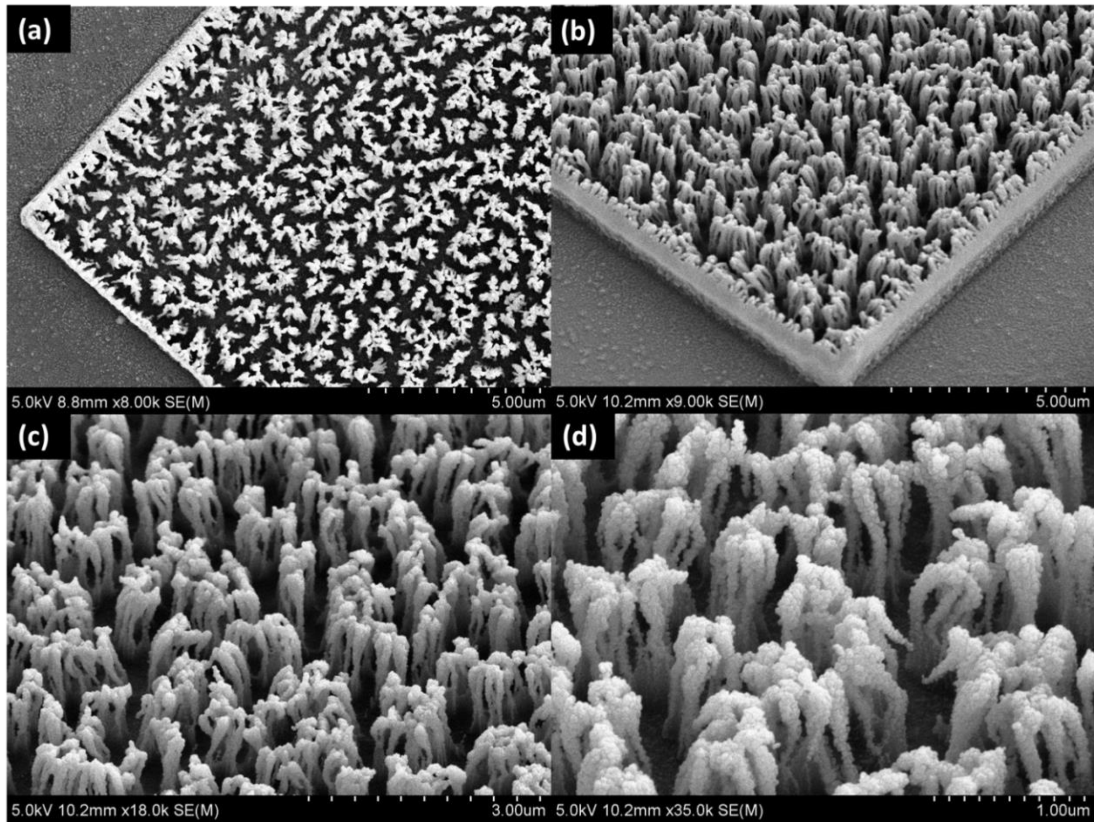

Figure 5.5. (a) - (d) SEM images of a MAP-fabricated thin film after RIE. (a) Top-view and (b) - (d) side-views. Each blade of nanograss has a detailed structure, with a rough, grainy surface. The magnification increases from (b) to (d).

As shown in Figure 5.6, the nanograss fabricated using low-speed MAP has blades with big "heads" that connect to one another. The nanograss in this sample has the highest density, the largest blade dimension, and the smallest air gaps.

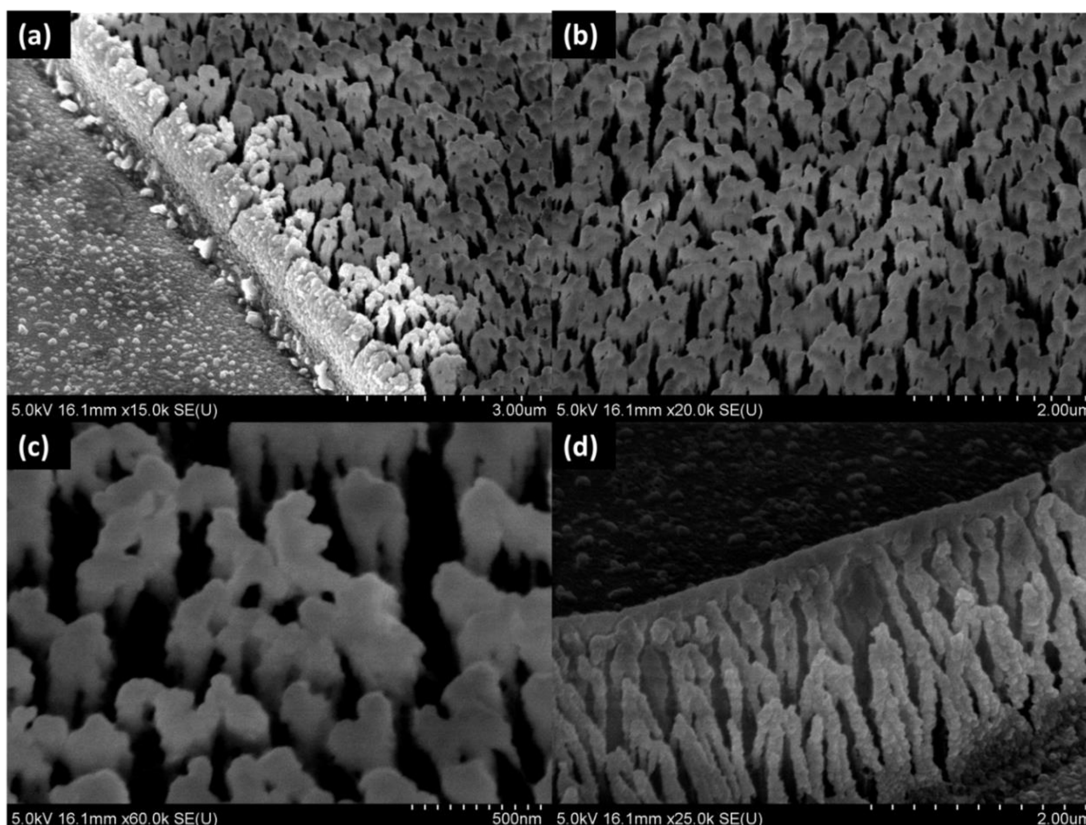

Figure 5.6. (a) - (d) SEM images of RIE-treated MAP (low speed)-fabricated acrylic structures; (a) - (c) a thin film; (d) a single line.

5.2.3 RIE-treated UV-cured acrylic films

To determine whether the nanograss morphology is related to voxels, we compared etching of substrates created with MAP and UV curing. The MAP-fabricated nanograsses were discussed in section 5.2.2. For UV curing studies, the acrylic resin was spin-coated on a glass slide and then cured by 365 nm light for 2 min. The resin composition and etch conditions were the same as those used in section 5.2.1. In the SEM images of UV-cured sample (Figure 5.7), the density and the dimensions of nanograss blades are similar to those in the high-speed MAP sample, which means that these two samples have a similar crosslinking ratio and a similar resistance to RIE. The inset of Figure 5.7(b) shows the water CA on the RIE-

treated, UV-cured film. As the UV-cured sample also shows nanograss characteristics, the formation of nanograss is not related to the existence of voxels. The properties of nanograss are, however, affected by the strength of the polymer framework. We expect that longer UV exposure will lead to denser nanograsses.

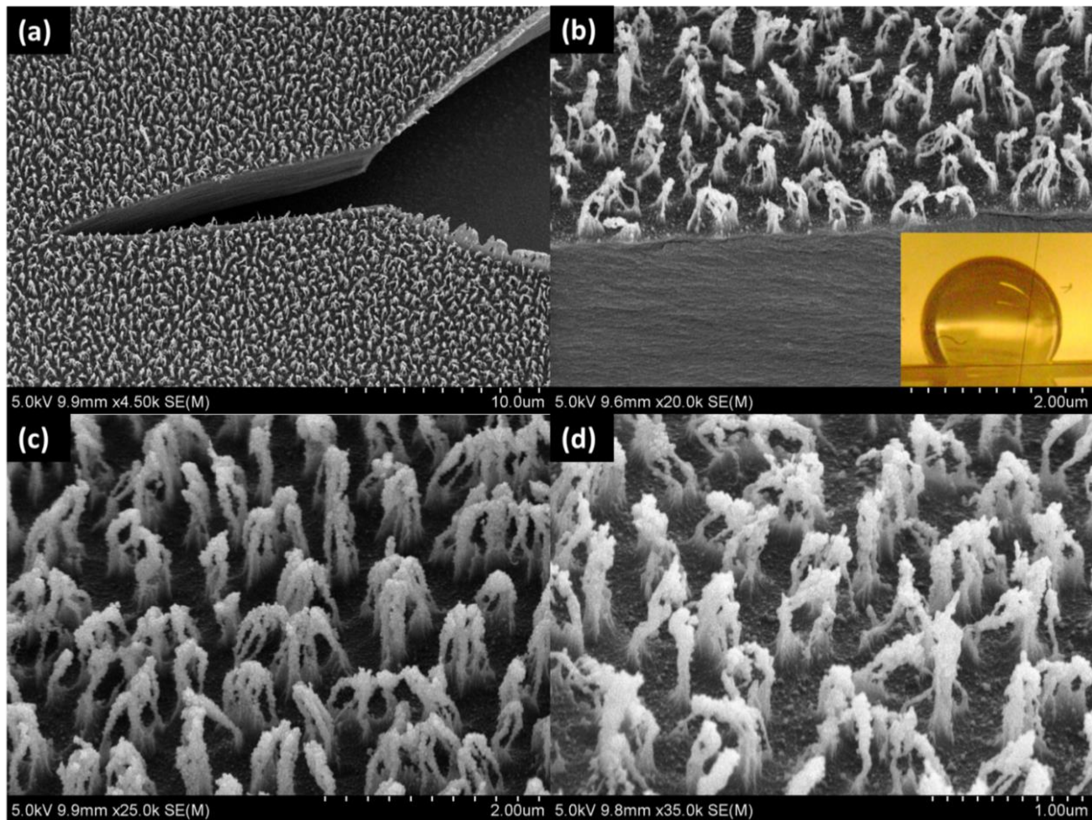

Figure 5.7. (a) and (d) SEM images of a UV-cured thin film after RIE. The magnification increases from (a) to (d). (b) has an inset showing the hydrophobicity (CA = 125°) of the nanograss. The UV-cured nanograss has a lower density and thinner blades compared with the MAP-fabricated nanograss.

5.2.4 Tilted RIE

If the framework of the acrylic polymer is isotropic, the direction of etching should not affect the growth of nanograss. Thus, we tilted the sample to attain a 45° etch angle relative to the substrate. In Figure 5.8, we show a MAP-fabricated acrylic structure etched at an angle of 45°. This sample exhibits etch traces instead of nanograss. The traces are found on the top surface as well as on the side walls. The traces have a smaller dimension and a higher density than the nanograss. Thus, the etch angle indeed affects the growth of nanograsses. A UV-cured pattern was etched with the angle of 45° and the result is illustrated in Figure 5.9. The tilted UV-cured sample also shows etch traces instead of nanograss. As shown in section 5.2.3, the formation of nanograss does not rely on the MAP voxels, because both the MAP-fabricated and UV-cured samples obtained the nanograss pattern after RIE. However, the formation of nanograss in both MAP-fabricated and UV-cured samples depends on the etch angle. The mechanism of the formation of nanograss and etch traces is unclear currently. Different etch angles should be tested to understand the etch-angle effect.

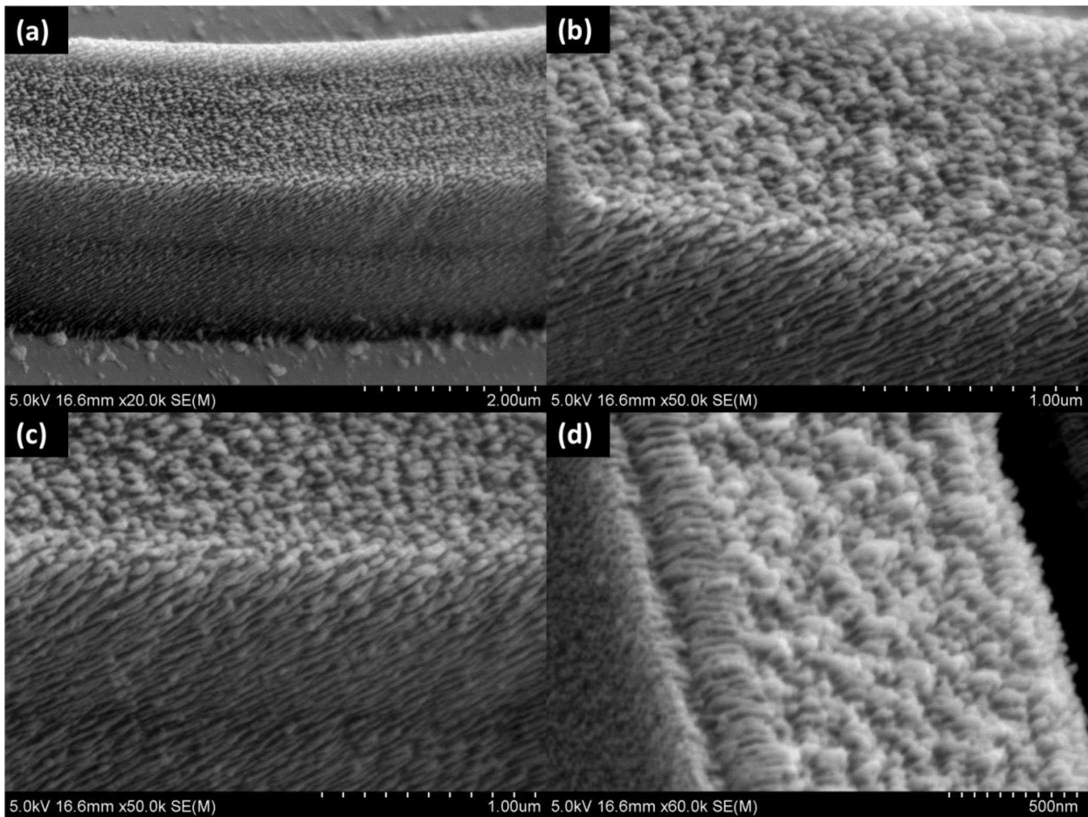

Figure 5.8. (a) A tilted, RIE-treated, MAP-fabricated waveguide (cross section 2 μm by 2 μm); (b) - (d) The same sample at higher magnification.

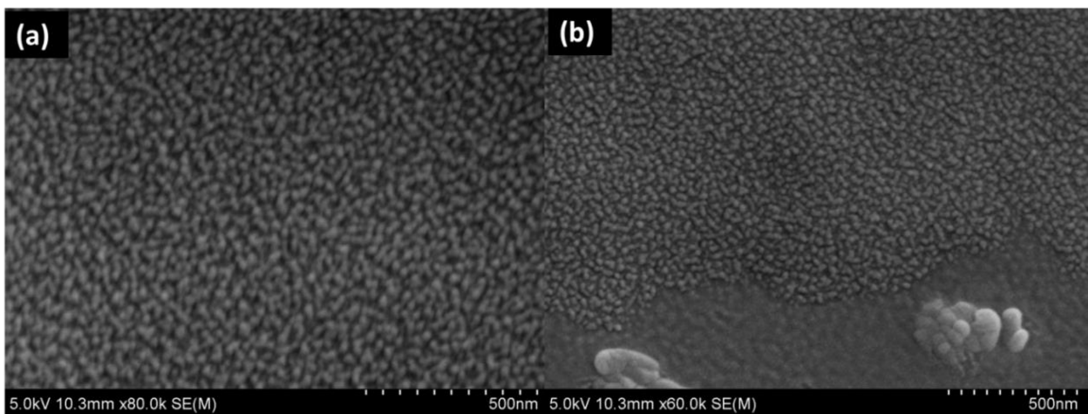

Figure 5.9. (a) and (b) SEM images of a tilted, RIE-treated, UV-cured thin film with a grainy surface.

5.3 Conclusions

Figure 5.10 gives a comprehensive comparison of MAP-fabricated and UV-cured nanograsses with RIE angles of 90° and 45°, and also different speeds of MAP fabrication. Our findings from the work detailed in this chapter suggest that:

1. In MAP, lower fabrication speeds (longer exposure times) give rise to a higher crosslinking ratio, lead to denser nanograsses with thicker blades.
2. The RIE-treated, UV-cured polymer structure also exhibits nanograss, which indicates that the nanograss does not originate from voxels.
3. Tilted etching causes only etch traces to appear, but not nanograsses.

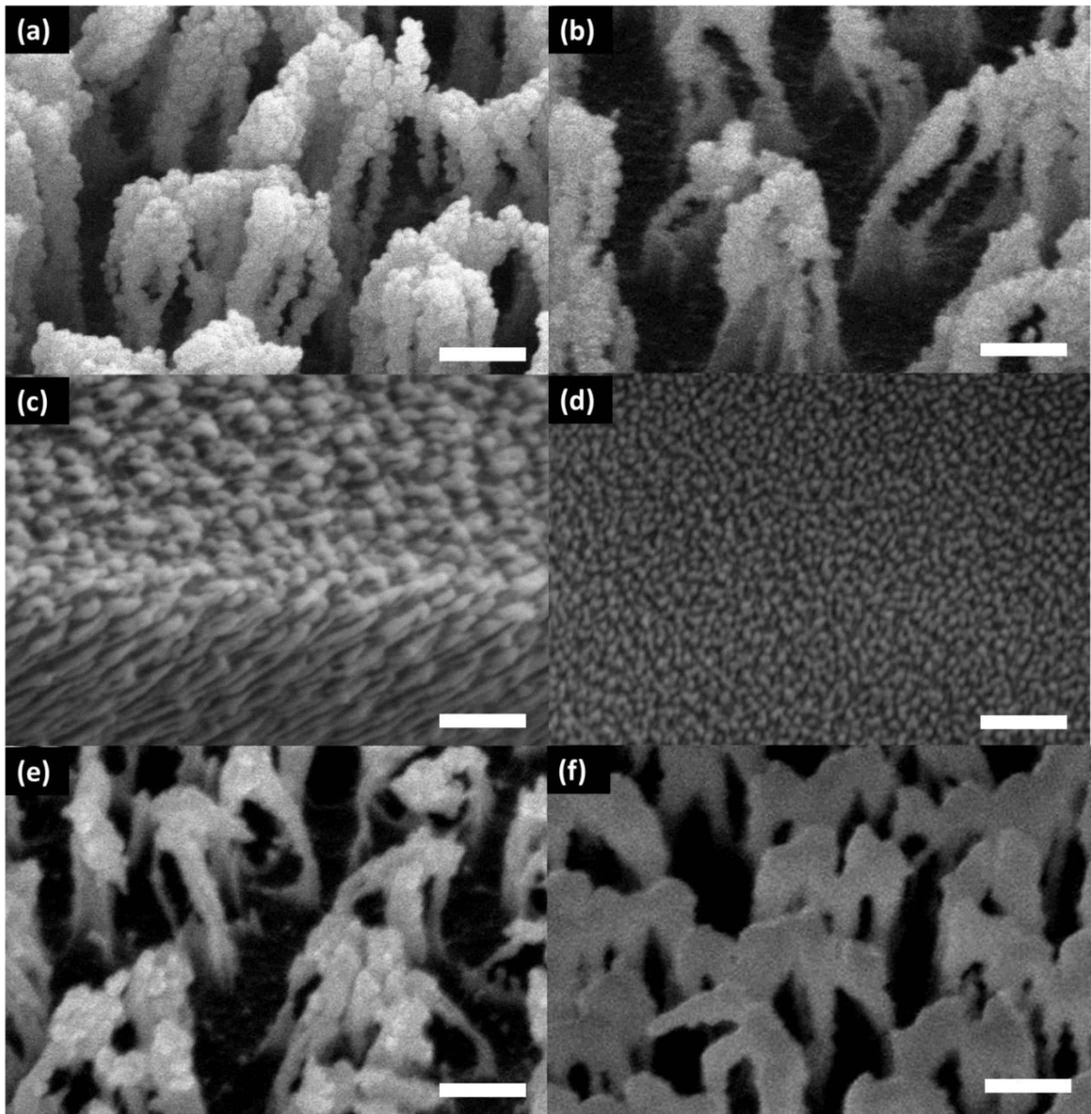

Figure 5.10. (a) RIE-treated, MAP-fabricated (medium speed) nanograss; (b) RIE-treated UV-cured (2 min) nanograss; (c) RIE-treated (tilted 45 °) MAP-fabricated (medium speed) nanograss; (d) RIE- treated (tilted 45 °) UV-cured (2 min) nanograss; (e) RIE-treated MAP-fabricated (high speed) nanograss; (f) RIE-treated MAP-fabricated (low speed) nanograss; all the scale bars are 250 nm.

References:

[1] M.-C. Yang, J. Shieh, C.-C. Hsu, and T.-C. Cheng, “Well-aligned silicon nanograss fabricated by hydrogen plasma dry etching,” *Electrochem. Solid-State Lett.*, vol. 8, pp. C131–C133, 2005.

[2] C.-C. Hong, P. Huang, and J. Shieh, “Fabrication of morphology-controlled sub-20-nm polymer nanotip and nanopore arrays using an identical nanograss mold,” *Macromolecules*, vol. 43, pp. 7722–7728, 2010.

[3] P. Roach, N. J. Shirtcliffe, and M. I. Newton, “Progess in superhydrophobic surface development,” *Soft Matter.*, vol. 4, p. 224, 2008.

[4] T. Krupenkin, J. A. Taylor, P. Kolodner, and M. Hodes, “Electrically tunable superhydrophobic nanostructured surfaces,” *Bell Labs Tech. J.*, vol. 10, pp. 161–170, 2005.

[5] C. Dorrer and J. Rühe, “Wetting of silicon nanograss: From superhydrophilic to superhydrophobic surfaces,” *Adv. Mater.*, vol. 20, pp. 159–163, 2008.

[6] N. Blondiaux, E. Scolan, A. M. Popa, J. Gavillet, and R. Pugin, “Fabrication of superhydrophobic surfaces with controlled topography and chemistry,” *Appl. Surf. Sci.*, vol. 256, pp. S46–S53, 2009.

[7] N. Vourdas, A. Tserepi, and E. Gogolides, “Nanotextured super-hydrophobic transparent poly(methyl methacrylate) surfaces using high-density plasma processing,” *Nanotechnology*, vol. 18, p. 125304, 2007.

[8] G. Sun, T. Gao, X. Zhao, and H. Zhang, "Fabrication of micro/nano dual-scale structures by improved deep reactive ion etching," *J. Micromech. Microeng.*, vol. 20, p. 075028, 2010.

[9] Z. Guo, W. Liu, and B.-L. Su, "Superhydrophobic surfaces: from natural to biomimetic to functional," *J. Colloid Interface Sci.*, vol. 353, pp. 335–355, 2011.

[10] "http://www.trincoll.edu/~alehman/PhotoBIOL210_03.htm." .

[11] R. Fürstner, W. Barthlott, C. Neinhuis, and P. Walzel, "Wetting and self-cleaning properties of artificial superhydrophobic surfaces," *Langmuir*, vol. 21, pp. 956–961, 2005.

[12] S. Farhadi, M. Farzaneh, and S. A. Kulinich, "Anti-icing performance of superhydrophobic surfaces," *Appl. Surf. Sci.*, vol. 257, pp. 6264–6269, 2011.

[13] O.-U. Nimittrakoolchai and S. Supothina, "Deposition of organic-based superhydrophobic films for anti-adhesion and self-cleaning applications," *J. Eur. Ceram. Soc.*, vol. 28, pp. 947–952, 2008.

[14] K. Koch and W. Barthlott, "Superhydrophobic and superhydrophilic plant surfaces: an inspiration for biomimetic materials," *Philos. Transact. A Math. Phys. Eng. Sci.*, vol. 367, pp. 1487–1509, 2009.

[15] Z. Guo, J. Fang, L. Wang, and W. Liu, "Fabrication of superhydrophobic copper by wet chemical reaction," *Thin Solid Films*, vol. 515, pp. 7190–7194, 2007.

[16] B. R. D'Urso and J. T. Simpson, "Composite, nanostructured, super-hydrophobic material," U.S. Patent 7,258,731 B22007.

[17] R. P. Hohmann, "Water-shedding flashings," U.S. Patent 0277393 A12011.

[18] M. Jiao, B. Yu, H. Cong, S. Yang, S. Huang, and S. Wang, "Preparation and property of a superhydrophobic glass sealant," *Adv. Mater.*, vol. 669, pp. 63–66, 2013.

[19] K. K. S. Lau, J. Bico, K. B. K. Teo, M. Chhowalla, G. a. J. Amaratunga, W. I. Milne, G. H. McKinley, and K. K. Gleason, "Superhydrophobic carbon nanotube forests," *Nano Lett.*, vol. 3, pp. 1701–1705, 2003.

[20] T. Humplik, J. Lee, S. C. O'Hern, B. a Fellman, M. a Baig, S. F. Hassan, M. a Atieh, F. Rahman, T. Laoui, R. Karnik, and E. N. Wang, "Nanostructured materials for water desalination," *Nanotechnology*, vol. 22, p. 292001, 2011.

[21] "http://www.gao.pitt.edu/antiicing.html."

[22] "http://www.ornl.gov/adm/partnerships/events/bridging_gap/presentations/Superhydrophobic_Materials.pdf." .

[23] L. Zhai, F. Ç. Cebeci, R. E. Cohen, and M. F. Rubner, "Stable superhydrophobic coatings from polyelectrolyte multilayers," *Nano Lett.*, vol. 4, pp. 1349–1353, 2004.

[24] F. Shi, Z. Wang, and X. Zhang, "Combining a layer-by-layer assembling technique with electrochemical deposition of gold aggregates to mimic the legs of water striders," *Adv. Mater.*, vol. 17, pp. 1005–1009, 2005.

[25] M. Li, J. Zhai, H. Liu, Y. Song, L. Jiang, and D. Zhu, "Electrochemical deposition of conductive superhydrophobic zinc oxide thin films," *J. Phys. Chem. B*, vol. 107, pp. 9954–9957, 2003.

[26] X. Zhang, F. Shi, X. Yu, H. Liu, Y. Fu, Z. Wang, L. Jiang, and X. Li, "Polyelectrolyte multilayer as matrix for electrochemical deposition of gold clusters: Toward super-hydrophobic surface," *J. Am. Chem. Soc.*, vol. 126, pp. 3064–3065, 2004.

[27] N. Vourdas, A. Tserepi, and E. Gogolides, "Nanotextured super-hydrophobic transparent poly(methyl methacrylate) surfaces using high-density plasma processing," *Nanotechnology*, vol. 18, p. 125304, 2007.

[28] J. Shiu, C. Kuo, and P. Chen, "Fabrication of tunable superhydrophobic surface by nanosphere lithography," *Chem. Mater.*, vol. 16, pp. 561–564, 2004.

[29] K. Tsougeni, N. Vourdas, A. Tserepi, E. Gogolides, and C. Cardinaud, "Mechanisms of oxygen plasma nanotexturing of organic polymer surfaces: from stable super hydrophilic to super hydrophobic surfaces," *Langmuir*, vol. 25, pp. 11748–11759, 2009.

[30] B. Balu, V. Breedveld, and D. W. Hess, "Fabrication of 'roll-off' and 'sticky' superhydrophobic cellulose surfaces via plasma processing," *Langmuir*, vol. 24, pp. 4785–4790, 2008.

[31] D. Wang, Z. Guo, Y. Chen, J. Hao, and W. Liu, "In situ hydrothermal synthesis of nanolamellate $CaTiO_3$ with controllable structures and wettability," *Inorg. Chem.*, vol. 46, pp. 7707–7709, 2007.

[32] X. Liu and J. He, "One-step hydrothermal creation of hierarchical microstructures toward superhydrophilic and superhydrophobic surfaces," *Langmuir*, vol. 25, pp. 11822–11826, 2009.

[33] F. Shi, X. Chen, L. Wang, J. Niu, J. Yu, Z. Wang, and X. Zhang, "Roselike microstructures formed by direct in situ hydrothermal synthesis: From superhydrophilicity to superhydrophobicity," *Chem. Mater.*, vol. 17, pp. 6177–6180, 2005.

[34] X. Zhang, F. Shi, J. Niu, Y. Jiang, and Z. Wang, "Superhydrophobic surfaces: from structural control to functional application," *J. Mater. Chem.*, vol. 18, pp. 621–633, 2008.

[35] X. J. Feng and L. Jiang, “Design and creation of superwetting/antiwetting surfaces,” *Adv. Mater.*, vol. 18, pp. 3063–3078, 2006.

[36] J. Shi, N. M. Alves, and J. F. Mano, “Towards bioinspired superhydrophobic poly(L-lactic acid) surfaces using phase inversion-based methods,” *Bioinspiration & Biomimetics*, vol. 3, p. 034003, 2008.

[37] X. Lu, C. Zhang, and Y. Han, “Low-density polyethylene superhydrophobic surface by control of its crystallization behavior,” *Macromol. Rapid Commun.*, vol. 25, pp. 1606–1610, 2004.

[38] X. Song, J. Zhai, Y. Wang, and L. Jiang, “Fabrication of superhydrophobic surfaces by self-assembly and their water-adhesion properties,” *J. Chem. Phys. B*, vol. 109, pp. 4048–4052, 2005.

[39] J. T. Han, Y. Zheng, J. H. Cho, X. Xu, and K. Cho, “Stable superhydrophobic organic-inorganic hybrid films by electrostatic self-assembly,” *J. Chem. Phys. B*, vol. 109, pp. 20773–20778, 2005.

[40] S. Srinivasan, V. K. Praveen, R. Philip, and A. Ajayaghosh, “Bioinspired superhydrophobic coatings of carbon nanotubes and linear π systems based on the ‘bottom-up’ self-assembly approach,” *Angew. Chem. Int. Ed.*, vol. 120, pp. 5834–5838, 2008.

[41] X. Song, J. Zhai, Y. Wang, and L. Jiang, “Self-assembly of amino-functionalized monolayers on silicon surfaces and preparation of superhydrophobic surfaces based on alkanoic acid dual layers and surface roughening,” *J. Colloid Interface Sci.*, vol. 298, pp. 267–273, 2006.

[42] K.-S. Liao, A. Wan, J. D. Batteas, and D. E. Bergbreiter, “Superhydrophobic surfaces formed using layer-by-layer self-assembly with aminated multiwall carbon nanotubes,” *Langmuir*, vol. 24, pp. 4245–4253, 2008.

[43] M. Manca, A. Cannavale, L. De Marco, A. S. Aricò, R. Cingolani, and G. Gigli, "Durable superhydrophobic and antireflective surfaces by trimethylsilanized silica nanoparticles-based sol-gel processing," *Langmuir*, vol. 25, pp. 6357–6362, 2009.

[44] K. Tadanaga, J. Morinaga, and T. Minami, "Formation of superhydrophobic-superhydrophilic pattern on flowerlike alumina thin film by the sol-gel method," *J. Sol-Gel Sci. Tech.*, vol. 19, pp. 211–214, 2000.

[45] K. Tadanaga, K. Kitamuro, A. Matsuda, and T. Minami, "Formation of superhydrophobic alumina coating films with high transparency on polymer substrates by the sol-gel method," *J. Sol-Gel Sci. Tech.*, vol. 26, pp. 705–708, 2003.

[46] N. J. Shirtcliffe, G. Mchale, M. I. Newton, and C. C. Perry, "Intrinsically superhydrophobic organosilica sol-gel foams," *Langmuir*, vol. 104, pp. 7777–7782, 2003.

[47] K. Tadanaga and J. Morinaga, "Micropatterning on flowerlike alumina coating film by the sol-gel method," *Chem. Mater.*, vol. 944, pp. 590–592, 2000.

[48] M. Callies, Y. Chen, F. Marty, A. Pépin, and D. Quéré, "Microfabricated textured surfaces for super-hydrophobicity investigations," *Microelectron. Eng.*, vol. 78, pp. 100–105, 2005.

[49] H. Liu, L. Feng, J. Zhai, L. Jiang, and D. Zhu, "Reversible wettability of a chemical vapor deposition prepared ZnO film between superhydrophobicity and superhydrophilicity," *Langmuir*, vol. 20, pp. 5659–5661, 2004.

[50] T. Sun, G. Wang, L. Feng, B. Liu, Y. Ma, L. Jiang, and D. Zhu, "Reversible switching between superhydrophilicity and superhydrophobicity," *Angew. Chem. Int. Ed.*, vol. 43, pp. 357–360, 2004.

[51] H. S. Lim, J. T. Han, D. Kwak, M. Jin, and K. Cho, "Photoreversibly switchable superhydrophobic surface with erasable and rewritable pattern," *J. Am. Chem. Soc.*, vol. 128, pp. 14458–14459, 2006.

[52] A. Nakajima, A. Fujishima, K. Hashimoto, and T. Watanabe, "Preparation of transparent superhydrophobic boehmite and silica films by sublimation of aluminum acetylacetonate," *Adv. Mater.*, vol. 11, pp. 1365–1368, 1999.

[53] N. Verplanck, E. Galopin, J.-C. Camart, V. Thomy, Y. Coffinier, and R. Boukherroub, "Reversible electrowetting on superhydrophobic silicon nanowires," *Nano Lett.*, vol. 7, pp. 813–817, 2007.

[54] L. Feng, Y. Zhang, J. Xi, Y. Zhu, N. Wang, F. Xia, and L. Jiang, "Petal effect: A superhydrophobic state with high adhesive force," *Langmuir*, vol. 24, pp. 4114–4119, 2008.

Chapter 6: Conclusions and Future Works

6.1 Conclusions

In recent years, a range of micro/nano fabrication methods have been developed and used to create nano- and micro-sized functional devices. Among these techniques, MAP stands out for its high resolution, ease of design and ability to create arbitrary 3-D microstructures.

In Chapter 2, we showed that by making use of the dependence of the coupling coefficient on the coupling gap sizes, optimized DRRs could be fabricated. Using the chosen parameters, pedestal DRRs with wide (> 30 nm) *FSR* and large isolation were directly fabricated using MAP. Their spectral properties were in good agreement with the simulation results. Thermal reflow and new materials are currently under study for improving device performance further.

In the third chapter, we demonstrated that μRR devices fabricated on a PDMS substrate offer a simple means of mapping the spatial dependence of the coupling on the polished face of an SPF. Coupling measurements made in this manner are non-destructive and highly reproducible. The resolution of the mapping depends on the length of the coupling region of the μRR device, which can be matched to the coupling length of whatever device is ultimately intended to be coupled to the SPF. It is also possible to fabricate a set of μRR devices with a range of coupling lengths on a

single PDMS substrate so that mapping can be performed at any desired resolution. We have also demonstrated that spectrum of a μRR device that has been fabricated on a PDMS substrate and is brought into contact with an SPF is sensitive to pressure. This phenomenon could lend itself to the development of new sensors. The fact that the resonances of the device shift with increasing pressure could also be employed as a tuning mechanism.

In Chapter 4, we combine MAP and optical tweezers to develop a suite of simple techniques that allow for precise control over the fabrication, manipulation, and positioning of microstructures in aqueous media. We have demonstrated the versatility of MBS for the photocrosslinking of acrylic monomers and proteins in aqueous solution. These materials and techniques open the door to employing fabrication methods, such as microbraiding and microweaving that are not possible using other direct-write methods. The new capabilities afforded by the combination of MAP and optical tweezers will have many microsystems applications in chemical and biological sciences and engineering, and beyond.

The fifth chapter focused on the development of a hydrophobic nanograss material obtained by etching the MAP-fabricated and UV-cured acrylic patterns. The comparison of MAP-fabricated and UV-cured nanograsses indicated that the nanograss pattern does not originate from MAP voxels. In MAP, a lower fabrication speed (longer exposure time), which gives rise to a higher crosslinking ratio, leads to denser nanograsses. This phenomenon illustrates that lower fabrication speed creates stronger polymer framework, which exhibits higher resistance to RIE. The acrylic patterns were etched at 90° and 45°. Tilted etching (45°) caused only etch traces but did not produce nanograsses.

6.2 Future work

6.2.1 On-chip optical devices

The second chapter discussed DRRs with expanded *FSR* and isolation of approximately -15 dB. To improve the finesse and isolation, the propagation loss inside the waveguides needs to be reduced. One approach to reduce the loss is using PDMS, instead of the acrylic resin, to fabricate the platform of the pedestal waveguide, as shown in Figure 6.1(a). This design will further enhance the mode confinement and decrease the mode leakage into the substrate. Preliminary SEM results are shown in Figure 6.1(b) and (c), where the acrylic waveguide were fabricated on top of the PDMS platform.

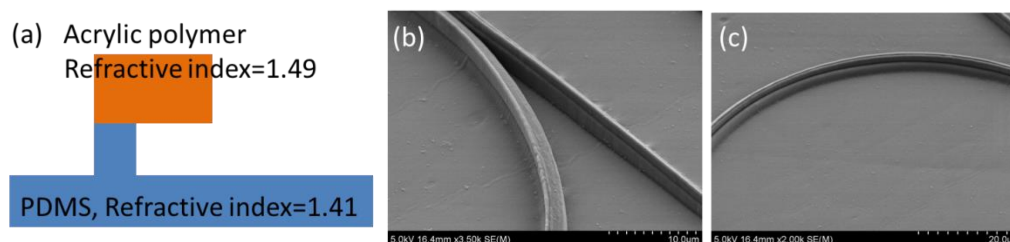

Figure 6.1. (a) Pedestal structure with PDMS platform. (b) and (c) are SEM images of acrylic waveguide sitting on the PDMS platform.

Another approach to improve the DRR performance is to explore novel materials with an even higher refractive index. We have demonstrated fabrication with commercially available, UV-curable optical adhesive NOA61. NOA61 has a relatively high refractive index (1.54 at 1550 nm), contributing to reduced propagation and bending loss. Compared with our acrylic resin, NOA61 also obtains a much higher temperature coefficient of its refractive index ($2x10^{-4}$/K) than our usual

materials, which enables the application for thermal-optic tuning [33]. Thus NOA61 is a good candidate for active resonator devices.

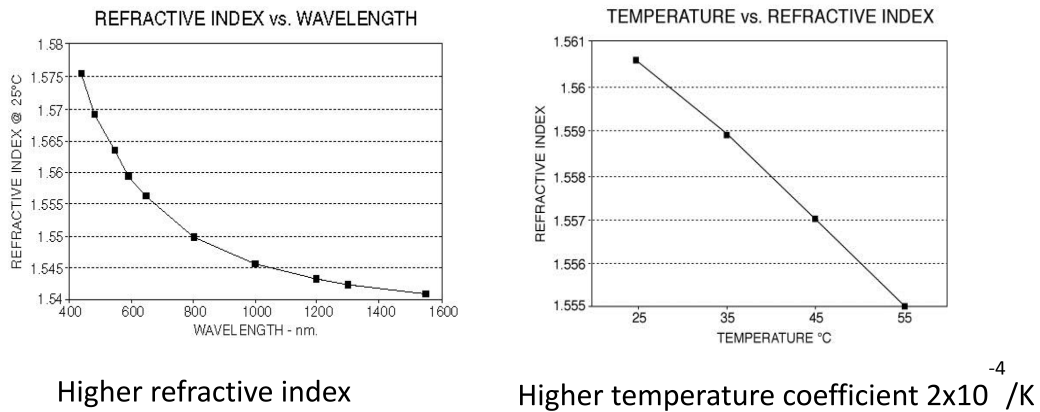

Figure 6.2. The refractive index of NOA 61 vs. wavelength and temperature.

As shown in Figure 6.3(a) and (c), waveguides made from NOA61 have rougher surfaces than the ones fabricated from acrylic resin, perhaps because the NOA61 has a higher refractive index and therefore leads to smaller voxel dimension. To achieve the same smoothness, either higher power or a closer spacing between points during fabrication is required. The high-index material already performs comparably to our usual materials, and once we have determined the appropriate fabrication and thermal-reflow parameters we expect to be able to achieve substantially improved performance.

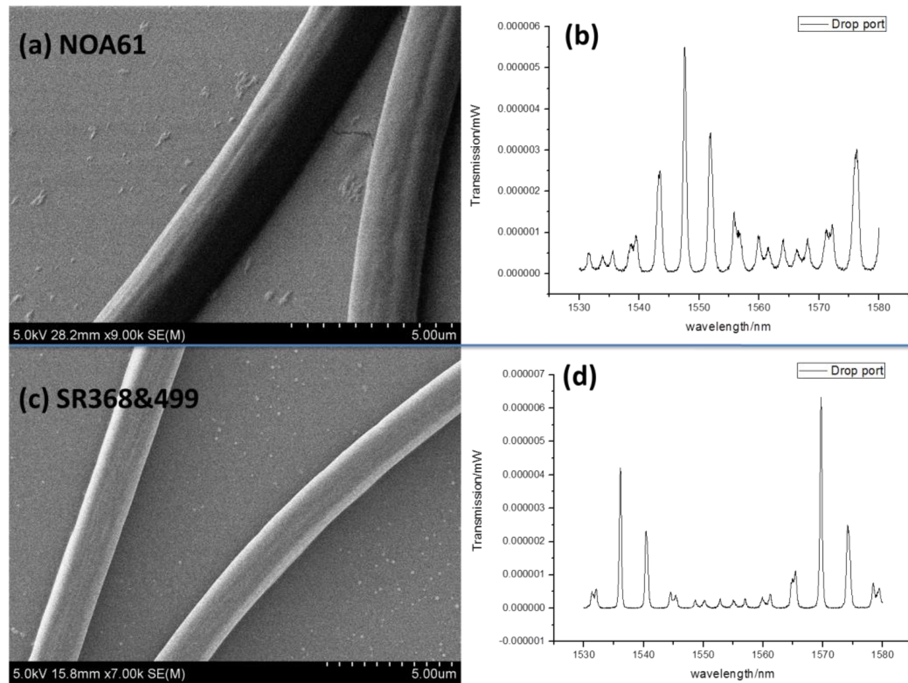

Figure 6.3. The NOA61 serial DRR in (a) has a drop port spectrum shown in (b). SEM image and drop-port spectrum of DRRs made from acrylic resin (SR368 and SR499) are shown in (c) and (d).

6.2.2 Side-polished optical fibers

We have showed in Chapter 3 that contacting a resonator to an SPF can be used to map the polished surface and sense the pressure. The next aim is to integrate the SPF with the polymeric resonator to form a functional, portable, single-piece device. This device can be used to introduce spectral notches in the fiber output or to drop out selected channels. To fabricate this device, the best coupling region on the SPF needs to be determined first, and then the resonator must be aligned with the fiber. To integrate the SPF with the resonator, a holder must be installed. The design of this holder is in progress.

In the future, an SPF-based modulator can be created if we choose a photoresist with a higher refractive index temperature coefficient or with electro

optical properties, such that temperature or electric field can be applied to tune the resonance peaks. Moreover, we have demonstrated the ability to fabricate DRRs with a *FSR* as high as 33 nm and isolation of approximately -15 dB. If the DRRs are coupled to an SPF instead of single microring resonators, only one channel will be dropped out in the entire C-band (1530 nm - 1560 nm). Combining the tunable photoresist and DRRs, a powerful modulator can be created with the capability of tuning a single channel from 1530 nm to 1565 nm.

6.2.3 MAP in aqueous system

As shown in Chapter 4, MAP and OTs can be combined in an aqueous photoresist to fabricate, manipulate and immobilize the complex micro-structures. As a next step, we can fabricate movable structures, such as micro-rotors or micro-pumps, in the aqueous medium inside a microfluidic channel. Optically driven rotation or pumping can be performed without changing the solution. Another future direction will be to use this toolbox to fabricate and manipulate the biomaterials, such as proteins and DNA.

6.2.4 Nanograss and superhydrophobicity

I have shown some preliminary results of hydrophobic nanograss materials in Chapter 5. However, further roughing and functionalization of the nanograss patterns is required to achieve superhydrophobicity.

To roughen the nanograss, the etch conditions, such as gas composition, pressure and etch time, require optimization. The optimal fabrication power and velocity need to be chosen. My preliminary studies indicate that a velocity of 10 μm/sec and an intensity of 5 mW (at the sample) give the roughest surface.

Functionalization can be carried out to reduce the surface free energy during or after RIE. In the process of RIE, the gas mixture, which contains a larger percentage of a fluoride-based compound (CF_4, CHF_3, SF_6), leads to an etched surface with a lower surface free energy. Different etch gas compositions give different hydrophobicity. After RIE, the sample can be treated with fluoride-based chemicals to obtain a low surface free energy.

References:

[1] Z.-S. Wang, H. Kawauchi, T. Kashima, and H. Arakawa, "Significant influence of TiO2 photoelectrode morphology on the energy conversion efficiency of N719 dye-sensitized solar cell," *Coord. Chem. Rev.*, vol. 248, pp. 1381–1389, 2004.

[2] A. W. Martinez, S. T. Phillips, G. M. Whitesides, and E. Carrilho, "Diagnostics for the developing world: Microfluidic paper-based analytical devices," *Anal. Chem.*, vol. 82, pp. 3–10, 2010.

[3] M. E. Motamedi, T. Oaks, M. C. Wu, L. Angeles, and K. S. J. Pister, "Micro-opto-electro-mechanical devices and on-chip optical processing," *Opt. Eng.*, vol. 36, pp. 1282–1297, 1997.

[4] M. V Schneider, "Contact lithography," U.S. Patent US39363011976.

[5] H. Lorenz, M. Despont, N. Fahrni, J. Brugger, P. Vettiger, and P. Renaud, "High-aspect-ratio, ultrathick, negative-tone near-UV photoresist and its applications for MEMS," *Sensor. Actuat. A*, vol. 64, pp. 33–39, 1998.

[6] J. Appelbaum, N. Plainfield, M. Feldman, and M. Hill, "Proximity lithography," U.S. Patent US40266531975.

[7] H. Kawata, J. M. Carter, A. Yen, and H. I. Smith, "Optical projection lithography using lenses with numerical apertures greater than unity," *Microelectron. Eng.*, vol. 9, pp. 31–36, 1989.

[8] J. D. Buckley, "Step-and-scan lithography using reduction optics," *J. Vac. Sci. Technol. B*, vol. 7, pp. 1607–1612, 1989.

[9] J. E. Bjorkholm, "EUV lithography — the successor to optical lithography," *Intel Technol. J.*, pp. 1–8, 1998.

[10] A. Heuberger, "X-ray lithography," *Microelectron. Eng.*, vol. 5, pp. 3–38, 1986.

[11] L. R. Harriott, B. Laboratories, L. Technologies, and M. Hill, "Scalpel : Projection electron beam lithography," *Proc. 1999 Part. Accelerator Conf.*, pp. 595–599, 1999.

[12] A. A Tseng, "Recent developments in nanofabrication using ion projection lithography," *Small*, vol. 1, pp. 594–608, 2005.

[13] C. Vieu, F. Carcenac, A. Pepin, Y. Chen, M. Mejias, A. Lebib, L. Couraud, and H. Launois, "Electron beam lithography : Resolution limits and applications," *Appl. Surf. Sci.*, vol. 164, pp. 111–117, 2000.

[14] J. Melngailis, "Focused ion beam lithography," *Nucl. Instrum. Meth. B*, vol. 80–81, pp. 1271–1280, 1993.

[15] X. N. Xie, H. J. Chung, C. H. Sow, and A. T. S. Wee, "Nanoscale materials patterning and engineering by atomic force microscopy nanolithography," *Mater. Sci. Eng. R*, vol. 54, pp. 1–48, 2006.

[16] H. Search, C. Journals, A. Contact, M. Iopscience, and I. P. Address, "Nanoimprint lithography : Challenges and prospects," *Nanotechnology*, vol. 91, pp. 91–95, 2001.

[17] S. Maruo, O. Nakamura, and S. Kawata, "Three-dimensional microfabrication with two-photon-absorbed photopolymerization," *Opt. Lett.*, vol. 22, pp. 132–134, 1997.

[18] Y.-H. Pao and P. M. Rentzepis, "Multiphoton absorption and optical-harmonic generation in highly absorbing molecular crystals," *J. Chem. Phys.*, vol. 43, pp. 1281–1286, 1965.

[19] C. N. LaFratta, J. T. Fourkas, T. Baldacchini, and R. a Farrer, "Multiphoton fabrication," *Angew. Chem. Int. Ed.*, vol. 46, pp. 6238–58, 2007.

[20] L. Li and J. T. Fourkas, "Multiphoton polymerization," *Mater. Today*, vol. 10, pp. 30–37, 2007.

[21] L. Li, R. R. Gattass, E. Gershgoren, H. Hwang, and J. T. Fourkas, "Achieving lambda/20 resolution by one-color initiation and deactivation of polymerization," *Science*, vol. 324, pp. 910–913, 2009.

[22] G. Kumi, C. O. Yanez, K. D. Belfield, and J. T. Fourkas, "High-speed multiphoton absorption polymerization: Fabrication of microfluidic channels with arbitrary cross-sections and high aspect ratios," *Lab Chip*, vol. 10, pp. 1057–1060, 2010.

[23] C. N. LaFratta, L. Li, and J. T. Fourkas, "Soft-lithographic replication of 3D microstructures with closed loops," *Proc. Nat. Acad. Sci. U.S.A.*, vol. 103, pp. 8589–8594, 2006.

[24] L. Li, E. Gershgoren, G. Kumi, W.-Y. Chen, P.-T. Ho, W. N. Herman, and J. T. Fourkas, "High-performance microring resonators fabricated with multiphoton absorption polymerization," *Adv. Mater.*, vol. 20, pp. 3668–3671, 2008.

[25] S. Maruo, K. Ikuta, and H. Korogi, "Force-controllable , optically driven micromachines fabricated by single-step two-photon," *J. Microelectromech. Syst.*, vol. 12, pp. 533–539, 2003.

[26] T. Umversrty, A. Aoba, and A. Aobaku, “Micropump and sample-injector for integrated chemical analyzing systems,” *Sensor. Actuat. A*, vol. 23, pp. 189–192, 1990.

[27] F. Dawood, S. Qin, L. Li, E. Y. Lin, and J. T. Fourkas, “Simultaneous microscale optical manipulation, fabrication and immobilisation in aqueous media,” *Chem. Sci.*, vol. 3, pp. 2449–2456, 2012.

[28] A. H. J. Yang and D. Erickson, “Optofluidic ring resonator switch for optical particle transport,” *Lab Chip*, vol. 10, pp. 769–774, 2010.

[29] A. Rostami and G. Rostami, “Full-optical realization of tunable low pass, high pass and band pass optical filters using ring resonators,” *Opt. Commun.*, vol. 240, pp. 133–151, 2004.

[30] D. Yevick, “High-speed polymer/silicon on insulator ring resonator switch,” *Opt. Eng.*, vol. 47, p. 094601, 2008.

[31] G. Chen, Y. Zhang, D. Huang, X. Zhang, H. Cao, and W. Chen, “Photonic generation of a microwave signal by employing a microfiber ring resonator,” *Opt. Commun.*, vol. 282, pp. 2552–2555, 2009.

[32] J. Hu, X. Sun, A. Agarwal, and L. C. Kimerling, “Design guidelines for optical resonator biochemical sensors,” *J. Opt. Soc. Am. B*, vol. 26, pp. 1032–1041, 2009.

[33] M. S. Luchansky and R. C. Bailey, “Silicon photonic microring resonators for quantitative cytokine detection and T-cell secretion analysis,” *Anal. Chem.*, vol. 82, pp. 1975–1981, 2010.

[34] H. P. Weber and R. Ulrich, “A thin-film ring laser,” *Appl. Phys. Lett.*, vol. 19, pp. 38–40, 1971.

[35] P. Rabiei, S. Member, W. H. Steier, L. Fellow, C. Zhang, and L. R. Dalton, "Polymer micro-ring filters and modulators," *J. Lightwave Technol.*, vol. 20, pp. 1968–1975, 2002.

[36] J. Haavisto and G. a Pajer, "Resonance effects in low-loss ring waveguides," *Opt. Lett.*, vol. 5, p. 510, 1980.

[37] D. Rafizadeh, J. P. Zhang, S. C. Hagness, A. Taflove, K. A. Stair, and S. T. Ho, "Waveguide-coupled AlGaAs � GaAs microcavity ring and disk resonators with high finesse and 21 . 6-nm free spectral range," *Opt. Lett.*, vol. 22, pp. 1244–1246, 1997.

[38] P. P. Absil, J. V Hryniewicz, B. E. Little, P. S. Cho, R. a Wilson, L. G. Joneckis, and P. T. Ho, "Wavelength conversion in GaAs micro-ring resonators," *Opt. Lett.*, vol. 25, pp. 554–556, 2000.

[39] Y. Kokubum, S. Kubota, and S. T. Chu, "Polarisation-independent vertically coupled microring resonator filter," *Electron. Lett.*, vol. 37, pp. 90–92, 2001.

[40] B. E. Little, T. Kaneko, and Y. Kokubun, "Cascaded microring resonators for crosstalk reduction and spectrum cleanup in add-drop filters," *IEEE Photon. Technol. Lett.*, vol. 11, pp. 1423–1425, 1999.

[41] S. T. Chu, W. Pan, S. Sato, B. E. Little, T. Kaneko, and Y. Kokubun, "ARROW-type vertical coupler filter: Design and fabrication," *J. Lightwave Technol.*, vol. 17, pp. 652–658, 1999.

[42] K. Oda, N. Takato, and H. Toba, "A wide-*FSR* waveguide double-ring resonator for optical FDM transmission systems," *J. Lightwave Technol.*, vol. 9, pp. 728–736, 1991.

[43] D. Rezzonico, A. Guarino, C. Herzog, M. Jazbinsek, and P. Günter, "High-finesse laterally coupled organic – inorganic hybrid polymer microring

resonators for VLSI photonics," *IEEE Photon. Technol. Lett.*, vol. 18, pp. 865–867, 2006.

[44] L. Li, E. Gershgoren, G. Kumi, W.-Y. Chen, P.-T. Ho, W. N. Herman, and J. T. Fourkas, "High-performance microring resonators fabricated with multiphoton absorption polymerization," *Adv. Mater.*, vol. 20, pp. 3668–3671, 2008.

[45] A. Schweinsberg, S. Hocdé, N. N. Lepeshkin, R. W. Boyd, C. Chase, and J. E. Fajardo, "An environmental sensor based on an integrated optical whispering gallery mode disk resonator," *Sensor. Actuat. B*, vol. 123, pp. 727–732, 2007.

[46] A. M. Armani and K. J. Vahala, "Heavy water detection using ultra-high-Q microcavities," *Opt. Lett.*, vol. 31, pp. 1896–1898, 2006.

[47] P. P. Yupapin, "Coupler-loss and coupling-coefficient-dependent bistability and instability in a fiber ring resonator," *Int. J. Light Electron Opt.*, vol. 119, pp. 492–494, 2008.

[48] J. Zhang, Y. Zhang, Q. Song, H. Tian, X. Zhang, H. Wu, J. Wang, C. Yu, G. Li, D. Fan, and P. Yuan, "A double-ring Mach–Zehnder interferometer sensor with high sensitivity," *J. Phys. D: Appl. Phys.*, vol. 45, p. 255102, 2012.

[49] W. Bogaerts, P. De Heyn, T. Van Vaerenbergh, K. De Vos, S. Kumar Selvaraja, T. Claes, P. Dumon, P. Bienstman, D. Van Thourhout, and R. Baets, "Silicon microring resonators," *Laser Photon. Rev.*, vol. 6, pp. 47–73, 2012.

[50] J. Yang, Q. Zhou, F. Zhao, X. Jiang, B. Howley, M. Wang, and R. T. Chen, "Characteristics of optical bandpass filters employing series-cascaded double-ring resonators," *Opt. Commun.*, vol. 228, pp. 91–98, 2003.

[51] C. H. Chaichuay, P. R. P. Yupapin, and P. R. Saeung, "The serially coupled multiple ring resonator filters and Vernier effect," *Opt. Appl.*, vol. 39, pp. 175–194, 2009.

[52] B. E. Little, S. T. Chu, H. a. Haus, J. Foresi, and J.-P. Laine, "Microring resonator channel dropping filters," *J. Lightwave Technol.*, vol. 15, pp. 998–1005, 1997.

[53] A. Shakouri and J. E. Bowers, "Wide tunable double ring resonator coupled lasers," *IEEE Photon. Technol. Lett.*, vol. 14, pp. 600–602, 2002.

[54] B. D. Timotijevic, F. Y. Gardes, W. R. Headley, G. T. Reed, M. J. Paniccia, O. Cohen, D. Hak, and G. Z. Masanovic, "Multi-stage racetrack resonator filters in silicon-on-insulator," *J. Opt. A*, vol. 8, pp. S473–S476, 2006.

[55] S. Suzuki, K. Oda, and Y. Hibino, "Integrated-optic double-ring resonators with a wide free spectral range of 100 GHz," *J. Lightwave Technol.*, vol. 13, pp. 1766–1771, 1995.

[56] D. G. Rabus, M. Hamacher, and H. Heidrich, "Resonance frequency tuning of a double ring resonator in GaInAsP/InP: Experiment and simulation," *Japan. J. Appl. Phys.*, vol. 41, pp. 1186–1189, 2002.

[57] L. Li, R. R. Gattass, E. Gershgoren, H. Hwang, and J. T. Fourkas, "Achieving lambda/20 Resolution by One-Color Initiation and Deactivation of Polymerization," *Science*, vol. 324, pp. 910–913, 2009.

[58] A Yariv, Y. Xu, R. K. Lee, and A. Scherer, "Coupled-resonator optical waveguide: A proposal and analysis," *Opt. Lett.*, vol. 24, pp. 711–713, 1999.

[59] M. Cai, O. Painter, and K. Vahala, "Observation of critical coupling in a fiber taper to a silica-microsphere whispering-gallery mode system," *Phys. Rev. Lett.*, vol. 85, pp. 74–77, 2000.

[60] H. Kogelnik and T. Li, “Laser beams and resonators,” *Proc. IEEE*, vol. 54, pp. 1312–1329, 1966.

[61] J. Poon, J. Scheuer, S. Mookherjea, G. Paloczi, Y. Huang, and A. Yariv, “Matrix analysis of microring coupled-resonator optical waveguides,” *Opt. Express*, vol. 12, pp. 90–103, 2004.

[62] W. A. Gambling, “The rise and rise of optical fibers,” *IEEE J. Sel.Top. Quantum Electron.*, vol. 6, pp. 1084–1093, 2000.

[63] L. F. Stokes, M. Chodorow, and H. J. Shaw, “All-single-mode fiber resonator,” *Opt. Lett.*, vol. 7, pp. 288–290, 1982.

[64] M. J. Guy, S. V Chernikov, J. R. Taylor, and R. Kashyap, “Low-loss fibre Bragg grating transmission filter based on a fibre polarisation splitter,” *Electron. Lett.*, vol. 30, pp. 1512–1513, 1994.

[65] A. S. Kewitsch, G. A. Rakuljic, P. A. Willems, and A. Yariv, “All-fiber zero-insertion-loss add-drop filter for wavelength-division multiplexing,” *Opt. Lett.*, vol. 23, pp. 106–108, 1998.

[66] J. C. Knight, G. Cheung, F. Jacques, and T. a Birks, “Phase-matched excitation of whispering-gallery-mode resonances by a fiber taper,” *Opt. Lett.*, vol. 22, pp. 1129–1131, 1997.

[67] B. S. Kawasaki, K. O. Hill, and R. G. Lamont, “Biconical-taper single-mode fiber coupler,” *Opt. Lett.*, vol. 6, pp. 327–328, 1981.

[68] S. Tseng and C. Chen, “Side-polished fibers,” *Appl. Opt.*, vol. 31, pp. 3438–3447, 1992.

[69] J. Laegsgaard, O. Bang, and A. Bjarklev, “Photonic crystal fiber design for broadband directional coupling,” *Opt. Lett.*, vol. 29, pp. 2473–2475, 2004.

[70] W. Jung, S. Kim, K. Kim, E. Kim, and S. Kang, "High-sensitivity temperature sensor using a side-polished single-mode fiber covered with the polymer planar waveguide," *IEEE Photon. Technol. Lett.*, vol. 13, pp. 1209–1211, 2001.

[71] F. Polarizers, S. Ma, and S. Tseng, "High-performance side-polished fibers and applications as liquid crystal clad," *J. Lightwave Technol.*, vol. 15, pp. 1554–1558, 1997.

[72] H. Sun, S. Member, A. Pyajt, J. Luo, Z. Shi, S. Hau, A. K. Jen, L. R. Dalton, A. Chen, and A. Abstract, "All-dielectric electrooptic sensor based on a polymer microresonator coupled side-polished optical fiber," *IEEE Sensor. J.*, vol. 7, pp. 515–524, 2007.

[73] R. K. Varshney, A. Singh, K. Pande, and B. P. Pal, "Side-polished fiber based gain-flattening filter for erbium doped fiber amplifiers," *Opt. Commun.*, vol. 271, pp. 441–444, 2007.

[74] N.-K. Chen, S. Chi, and S.-M. Tseng, "Wideband tunable fiber short-pass filter based on side-polished fiber with dispersive polymer overlay," *Opt. Lett.*, vol. 29, pp. 2219–2221, 2004.

[75] J. Heebner, R. Grover, and T. Ibrahim, "Optical microresonator theory," in *Optical Microresonators: Theory, Fabrication, and Applications*, 2008, pp. 71–103.

[76] J. V. Hryniewicz, P. P. Absil, B. E. Little, R. a. Wilson, and P.-T. Ho, "Higher order filter response in coupled microring resonators," *IEEE Photon. Technol. Lett.*, vol. 12, pp. 320–322, 2000.

[77] P. Rabiei, S. Member, W. H. Steier, L. Fellow, C. Zhang, and L. R. Dalton, "Polymer micro-ring filters and modulators," *J. Lightwave Technol.*, vol. 20, pp. 1968–1975, 2002.

[78] N. Jokerst, M. Royal, S. Palit, L. Luan, S. Dhar, and T. Tyler, "Chip scale integrated microresonator sensing systems," *J. Biophoton.*, vol. 2, pp. 212–226, 2009.

[79] M. K. S. Martin T. Hill, Harmen J. S. Dorren, Tjibbe de Vries, Xaveer J. M. Leijtens, Jan Hendrik den Besten, Barry Smalbrugge, Yok-Siang Oei, Hans Binsma, Giok-Djan Khoe, "A fast low-power optical memory based on coupled micro-ring lasers," *Nature*, vol. 432, pp. 11–14, 2004.

[80] T. Sherwood, A. C. Young, J. Takayesu, A. K. Y. Jen, and L. R. Dalton, "Microring resonators on side-polished optical fiber," *IEEE Photon. Technol. Lett.*, vol. 17, pp. 2107–2109, 2005.

[81] Shoji Maruo and J. T. Fourkas, "Recent progress in multiphoton microfabrication," *Laser Photon. Rev.*, vol. 2, pp. 100–111, 2008.

[82] C. N. LaFratta, J. T. Fourkas, T. Baldacchini, and R. a Farrer, "Multiphoton fabrication," *Angew. Chem. Int. Ed.*, vol. 46, pp. 6238–58, 2007.

[83] L. Li, E. Gershgoren, G. Kumi, W.-Y. Chen, P.-T. Ho, W. N. Herman, and J. T. Fourkas, "High-performance microring resonators fabricated with multiphoton absorption polymerization," *Adv. Mater.*, vol. 20, pp. 3668–3671, 2008.

[84] H. Zappe, *Fundamentals of Micro-Optics* (Cambridge University Press, Cambridge, UK, 2010)

[85] J. El-Ali, P. K. Sorger and K. F. Jensen, "Cells on chips," *Nature*, vol. 442, pp. 403-411, 2006.

[86] J. E. Keymer, P. Galajda, C. Muldoon, S. Park and R. H. Austin, "Bacterial metapopulations in nanofabricated landscapes," *Proc. Nat. Acad. Sci. USA*, vol. 103, pp. 17290-17295, 2006.

[87] E. Livak-Dahl, I. Sinn and M. Burns, "Microfluidic chemical analysis systems," *Annu. Rev. Chem. Biomol. Eng.*, vol. 2, pp. 325-353, 2011.

[88] G. M. Whitesides, "The origins and future of microfluidics," *Nature*, vol. 442, pp. 368-373, 2006.

[89] G. M. Whitesides and A. D. Stroock, "Flexible methods for microfluidics," *Phys. Today*, vol. 54, pp. 42-48, 2001.

[90] R. V. Bellamkonda, "Peripheral nerve regeneration: An opinion on channels, scaffolds and anisotropy," *Biomater.*, vol. 27, pp. 3515-3518, 2006.

[91] A. Reiser, *Photoreactive polymers: The science and technology of resists*, Wiley, New York, 1989.

[92] J.-P. Fouassier, *Photoinitiation, photopolymerization and photocuring: Fundamentals and applications*, Hanser Publishers, Munich, 1995.

[93] A. Ashkin, J. M. Dziedzic, J. E. Bjorkholm and S. Chu, "Observation of a single-beam gradient force optical trap for dielectric particles," *Opt. Lett.*, vol. 11, pp. 288-290, 1986.

[94] S. M. Block, "Making light work with optical tweezers," *Nature*, vol. 360, pp. 493-495, 1992.

[95] D. G. Grier, "A revolution in optical manipulation," *Nature*, vol. 424, pp. 810-816, 2003.

[96] K. Dholakia and P. Reece, "Optical micromanipulation takes hold," *Nano Today*, vol. 1, pp. 18-27, 2006.

[97] A. Jonas and P. Zemanek, "Light at work: The use of optical forces for particle manipulation, sorting and analysis," *Electrophor.*, vol. 29, pp. 4813-4851, 2008.

[98] K. Ladavac, K. Kasza and D. G. Grier, "Sorting mesoscopic objects with periodic potential landscapes: Optical fractionation," *Phys. Rev. E*, vol.70, pp. 010901, 2004.

[99] M. P. MacDonald, L. Paterson, K. Volke-Sepulveda, J. Arlt, W. Sibbett and K. Dholakia, "Creation and enhanced manipulation of 3-dimensional optically trapped structures," *Science*, vol. 296, pp. 1101-1103, 2002.

[100] P. Galajda and P. Ormos, "Complex micromachines produced and driven by light," *Appl. Phys. Lett.*, vol. 78, pp. 249-251, 2001.

[101] S. Maruo, K. Ikuta and H. Korogi, "Force-controllable, optically driven micromachines fabricated by single-step two-photon microstereolithography," *J. Microelectromech. Syst.*, vol. 12, pp. 533-539, 2003.

[102] S. Maruo, A. Takaura and Y. Saito, "Optically driven micropump with a twin spiral microrotor," *Opt. Express*, vol. 17, pp. 18525-18532, 2009.

[103] J. T. Finer, R. M. Simmons and J. A. Spudich, "Single myosin molecule mechanics: Piconewton forces and nanometre steps," *Nature*, vol. 368, pp. 113-119, 1994.

[104] A. D. Mehta, M. Rief, J. A. Spudich, D. A. Smith and R. M. Simmons, "Single-molecule biomechanics with optical methods," *Science*, vol. 283, pp. 1689-1695, 1999.

[105] K. Svoboda, P. P. Mitra and S. M. Block, "Fluctuation analysis of kinesin movement," *Proc. Nat. Acad. Sci. USA*, vol. 91, pp. 11782-11786, 1994.

[106] K. Svoboda, C. F. Schmidt, B. J. Schnapp and S. M. Block, "Direct observation of kinesin stepping by optical trapping interferometry," *Nature*, vol. 365, pp. 721-727, 1993.

[107] R. E. Holmlin, M. Schiavoni, C. Y. Chen, S. P. Smith, M. G. Prentiss and G. M. Whitesides, "Light-driven microfabrication: Assembly of multicomponent, three-dimensional structures by using optical tweezers," *Angew. Chem. Int. Ed.*, vol. 39, pp. 3503-3506, 2000.

[108] A. Terray, J. Oakey and D. W. M. Marr, "Fabrication of linear colloidal structures for microfluidic applications," *Appl. Phys. Lett.*, vol. 81, pp. 1555-1557, 2002.

[109] A. Terray, J. Oakey and D. W. M. Marr, "Microfluidic control using colloidal devices," *Science,* vol. 296, pp. 1841-1844, 2002.

[110] E. McLeod and C. B. Arnold, "Subwavelength direct-write nanopatterning using optically trapped microspheres," *Nature Nanotech.*, vol. 3, pp. 413-417, 2008.

[111] E. McLeod and C. B. Arnold, "Array-based optical nanolithography using optically trapped microlenses," *Opt. Express*, vol. 17, pp. 3640-3650, 2009.

[112] S. Kawata, H. B. Sun, T. Tanaka and K. Takada, "Finer features for functional micro- devices," *Nature*, vol. 412, pp. 697-698, 2001.

[113] C. N. LaFratta, J. T. Fourkas, T. Baldacchini and R. A. Farrer, “Multiphoton fabrication,” *Angew. Chem. Int. Ed.*, vol. 46, pp. 6238-6258, 2007.

[114] S. Maruo and J. T. Fourkas, "Recent progress in multiphoton microfabrication," *Laser Photon. Rev.*, vol. 2, pp. 100-111, 2008.

[115] D. Yang, S. J. Jhaveri and C. K. Ober, "Three-dimensional microfabrication by Two-Photon Lithography," *MRS Bull.*, vol. 30, pp. 976-982, 2005.

[116] J. T. Fourkas, "Nanoscale photolithography with visible light," *J. Phys. Chem. Lett.*, vol. 1, pp. 1221-1227, 2010.

[117] J.-F. Xing, X.-Z. Dong, W.-Q. Chen, X.-M. Duan, N. Takeyasu, T. Tanaka and S. Kawata, "Improving spatial resolution of two-photon microfabrication by using photoinitiator with high initiating efficiency," *Appl. Phys. Lett.*, vol. 90, pp. 131106, 2007

[118] S. Basu and P. J. Campagnola, "Properties of crosslinked protein matrices for tissue engineering applications synthesized by multiphoton excitation," *J. Biomed. Mater. Res. A*, vol. 71A, pp. 359-368, 2004.

[119] S. Basu, L. P. Cunningham, G. D. Pins, K. A. Bush, R. Taboada, A. R. Howell, J. Wang and P. J. Campagnola, "Multiphoton excited fabrication of collagen matrixes cross-linked by a modified benzophenone dimer: Bioactivity and enzymatic degradation," *Biomacromol.*, vol. 6, pp. 1465-1474, 2005.

[120] S. Basu, C. W. Wolgemuth and P. J. Campagnola, "Measurement of normal and anomalous diffusion of dyes within protein structures fabricated *via* multiphoton excited cross-linking," *Biomacromol.*, vol. 5, pp. 2347-2357, 2004.

[121] R. T. Hill, J. L. Lyon, R. Allen, K. J. Stevenson and J. B. Shear, "Microfabrication of three-dimensional bioelectronic architectures," *J. Amer. Chem. Soc.*, vol. 127, pp. 10707-10711, 2005.

[122] B. Kaehr, R. Allen, D. J. Javier, J. Currie and J. B. Shear, "Guiding neuronal development with in situ microfabrication," *Proc. Nat. Acad. Sci.* USA, vol. 101, pp. 16104-16108, 2004.

[123] B. Kaehr and J. B. Shear, "Mask-directed multiphoton lithography," *J. Amer. Chem. Soc.*, vol. 129, pp. 1904-1905, 2007.

[124] A. Berg, R. Wyrwa, J. Weisser, T. Weiss, R. Schade, G. Hildebrand, K. Liefeith, B. Schneider, R. Ellinger and M. Schnabelrauch, "Synthesis of photopolymerizable hydrophilic macromers and evaluation of their applicability as reactive resin components for the fabrication of three-dimensionally structured hydrogel matrices by 2-photon-polymerization," *Adv. Eng. Mater.*, vol. 13, pp. B274-B284, 2011.

[125] L. Grimm, K. J. Hilke and E. Scharrer, "The mechanism of the cross linking of poly(vinyl alcohol) by ammonium dichromate with U.V.-light," *J. Electrochem. Soc.*, vol. 130, pp. 1767-1771, 1983.

[126] A. Chemtob, B. Kunstler, C. Croutxe-Barghorn and S. Fouchard, "*Photoinduced miniemulsion polymerization,*" *Colloid Polymer Sci.*, vol. 288, pp. 579-587, 2010

[127] S. J. Jhaveri, J. D. McMullen, R. Sijbesma, L.-S. Tan, W. Zipfel and C. K. Ober, "Direct three-dimensional microfabrication of hydrogels via two-photon lithography in aqueous solution," *Chem. Mater.*, vol. 21, pp. 2003-2006, 2009.

[128] B. D. Mather, K. Viswanathan, K. M. Miller and T. E. Long, "*Michael addition reactions in macromolecular design for emerging technologies,*" *Prog. Polymer Sci.*, vol. 31, pp. 487-531, 2006.

[129] L. Li, M. Driscoll, G. Kumi, R. Hernandez, K. J. Gaskell, W. Losert and J. T. Fourkas, “Binary and gray-scale patterning of chemical functionality on polymer films,” *J. Amer. Chem. Soc.*, vol. 130, pp. 13512-13513, 2008.

[130] K. Kojima, M. Ito, H. Morishita and N. Hayashi, "Thioxanthone based water-soluble photoinitiators for acrylamide photopolymerization," *Chem. Mater.*, vol. 10, pp. 3429-3433, 1998.

[131] C. Ropp, Z. Cummins, R. Probst, S. Qin, J. T. Fourkas, B. Shapiro and E. Waks, "Positioning and immobilization of individual quantum dots with nanoscale precision," *Nano Lett.*, vol. 10, pp. 4673-4679, 2010.

[132] T. Baldacchini, C. N. LaFratta, R. A. Farrer, M. C. Teich, B. E. A. Saleh, M. J. Naughton and J. T. Fourkas, "Acrylic-based resin with favorable properties for three-dimensional two-*photon polymerization,*" *J. Appl. Phys.*, vol. 95, pp. 6072-6076, 2004.

[133] M.-C. Yang, J. Shieh, C.-C. Hsu, and T.-C. Cheng, "Well-aligned silicon nanograss fabricated by hydrogen plasma dry etching," *Electrochem. Solid-State Lett.*, vol. 8, pp. C131–C133, 2005.

[134] C.-C. Hong, P. Huang, and J. Shieh, "Fabrication of morphology-controlled sub-20-nm polymer nanotip and nanopore arrays using an identical nanograss mold," *Macromolecules*, vol. 43, pp. 7722–7728, 2010.

[135] P. Roach, N. J. Shirtcliffe, and M. I. Newton, "Progess in superhydrophobic surface development," *Soft Matter.*, vol. 4, p. 224, 2008.

[136] T. Krupenkin, J. A. Taylor, P. Kolodner, and M. Hodes, "Electrically tunable superhydrophobic nanostructured surfaces," *Bell Labs Tech. J.*, vol. 10, pp. 161–170, 2005.

[137] C. Dorrer and J. Rühe, "Wetting of silicon nanograss: From superhydrophilic to superhydrophobic surfaces," *Adv. Mater.*, vol. 20, pp. 159–163, 2008.

[138] N. Blondiaux, E. Scolan, A. M. Popa, J. Gavillet, and R. Pugin, "Fabrication of superhydrophobic surfaces with controlled topography and chemistry," *Appl. Surf. Sci.*, vol. 256, pp. S46–S53, 2009.

[139] N. Vourdas, A. Tserepi, and E. Gogolides, "Nanotextured super-hydrophobic transparent poly(methyl methacrylate) surfaces using high-density plasma processing," *Nanotechnology*, vol. 18, p. 125304, 2007.

[140] G. Sun, T. Gao, X. Zhao, and H. Zhang, "Fabrication of micro/nano dual-scale structures by improved deep reactive ion etching," *J. Micromech. Microeng.*, vol. 20, p. 075028, 2010.

[141] Z. Guo, W. Liu, and B.-L. Su, "Superhydrophobic surfaces: From natural to biomimetic to functional," *J. Colloid Interface Sci.*, vol. 353, pp. 335–355, 2011.

[142] "http://www.trincoll.edu/~alehman/PhotoBIOL210_03.htm." .

[143] R. Fürstner, W. Barthlott, C. Neinhuis, and P. Walzel, "Wetting and self-cleaning properties of artificial superhydrophobic surfaces," *Langmuir*, vol. 21, pp. 956–961, 2005.

[144] S. Farhadi, M. Farzaneh, and S. A. Kulinich, "Anti-icing performance of superhydrophobic surfaces," *Appl. Surf. Sci.*, vol. 257, pp. 6264–6269, 2011.

[145] O.-U. Nimittrakoolchai and S. Supothina, "Deposition of organic-based superhydrophobic films for anti-adhesion and self-cleaning applications," *J. Eur. Ceram. Soc.*, vol. 28, pp. 947–952, 2008.

[146] K. Koch and W. Barthlott, "Superhydrophobic and superhydrophilic plant surfaces: An inspiration for biomimetic materials," *Philos. Transact. A Math. Phys. Eng. Sci.*, vol. 367, pp. 1487–1509, 2009.

[147] Z. Guo, J. Fang, L. Wang, and W. Liu, “Fabrication of superhydrophobic copper by wet chemical reaction,” *Thin Solid Films*, vol. 515, pp. 7190–7194, 2007.

[148] B. R. D’Urso and J. T. Simpson, “Composite, nanostructured, super-hydrophobic material,” U.S. Patent 7,258,731 B22007.

[149] R. P. Hohmann, “Water-shedding flashings,” U.S. Patent 0277393 A12011.

[150] M. Jiao, B. Yu, H. Cong, S. Yang, S. Huang, and S. Wang, “Preparation and property of a superhydrophobic glass sealant,” *Adv. Mater.*, vol. 669, pp. 63–66, 2013.

[151] K. K. S. Lau, J. Bico, K. B. K. Teo, M. Chhowalla, G. a. J. Amaratunga, W. I. Milne, G. H. McKinley, and K. K. Gleason, “Superhydrophobic carbon nanotube forests,” *Nano Lett.*, vol. 3, pp. 1701–1705, 2003.

[152] T. Humplik, J. Lee, S. C. O’Hern, B. a Fellman, M. a Baig, S. F. Hassan, M. a Atieh, F. Rahman, T. Laoui, R. Karnik, and E. N. Wang, “Nanostructured materials for water desalination,” *Nanotechnology*, vol. 22, p. 292001, 2011.

[153] “http://www.gao.pitt.edu/antiicing.html.”

[154] “http://www.ornl.gov/adm/partnerships/events/bridging_gap/presentations/Superhydrophobic_Materials.pdf.” .

[155] L. Zhai, F. Ç. Cebeci, R. E. Cohen, and M. F. Rubner, “Stable superhydrophobic coatings from polyelectrolyte multilayers,” *Nano Lett.*, vol. 4, pp. 1349–1353, 2004.

[156] F. Shi, Z. Wang, and X. Zhang, “Combining a layer-by-layer assembling technique with electrochemical deposition of gold aggregates to mimic the legs of water striders,” *Adv. Mater.*, vol. 17, pp. 1005–1009, 2005.

[157] M. Li, J. Zhai, H. Liu, Y. Song, L. Jiang, and D. Zhu, "Electrochemical deposition of conductive superhydrophobic zinc oxide thin films," *J. Phys. Chem. B*, vol. 107, pp. 9954–9957, 2003.

[158] X. Zhang, F. Shi, X. Yu, H. Liu, Y. Fu, Z. Wang, L. Jiang, and X. Li, "Polyelectrolyte multilayer as matrix for electrochemical deposition of gold clusters: Toward super-hydrophobic surface," *J. Am. Chem. Soc.*, vol. 126, pp. 3064–3065, 2004.

[159] N. Vourdas, A. Tserepi, and E. Gogolides, "Nanotextured super-hydrophobic transparent poly(methyl methacrylate) surfaces using high-density plasma processing," *Nanotechnology*, vol. 18, p. 125304, 2007.

[160] J. Shiu, C. Kuo, and P. Chen, "Fabrication of tunable superhydrophobic surface by nanosphere lithography," *Chem. Mater.*, vol. 16, pp. 561–564, 2004.

[161] K. Tsougeni, N. Vourdas, A. Tserepi, E. Gogolides, and C. Cardinaud, "Mechanisms of oxygen plasma nanotexturing of organic polymer surfaces: From stable super hydrophilic to super hydrophobic surfaces," *Langmuir*, vol. 25, pp. 11748–11759, 2009.

[162] B. Balu, V. Breedveld, and D. W. Hess, "Fabrication of 'roll-off' and 'sticky' superhydrophobic cellulose surfaces via plasma processing," *Langmuir*, vol. 24, pp. 4785–4790, 2008.

[163] D. Wang, Z. Guo, Y. Chen, J. Hao, and W. Liu, "In situ hydrothermal synthesis of nanolamellate CaTiO3 with controllable structures and wettability," *Inorg. Chem.*, vol. 46, pp. 7707–7709, 2007.

[164] X. Liu and J. He, "One-step hydrothermal creation of hierarchical microstructures toward superhydrophilic and superhydrophobic surfaces," *Langmuir*, vol. 25, pp. 11822–11826, 2009.

[165] F. Shi, X. Chen, L. Wang, J. Niu, J. Yu, Z. Wang, and X. Zhang, "Roselike microstructures formed by direct in situ hydrothermal synthesis: From superhydrophilicity to superhydrophobicity," *Chem. Mater.*, vol. 17, pp. 6177–6180, 2005.

[166] X. Zhang, F. Shi, J. Niu, Y. Jiang, and Z. Wang, "Superhydrophobic surfaces: From structural control to functional application," *J. Mater. Chem.*, vol. 18, pp. 621–633, 2008.

[167] X. J. Feng and L. Jiang, "Design and creation of superwetting/antiwetting surfaces," *Adv. Mater.*, vol. 18, pp. 3063–3078, 2006.

[168] J. Shi, N. M. Alves, and J. F. Mano, "Towards bioinspired superhydrophobic poly(L-lactic acid) surfaces using phase inversion-based methods," *Bioinspiration & Biomimetics*, vol. 3, p. 034003, 2008.

[169] X. Lu, C. Zhang, and Y. Han, "Low-density polyethylene superhydrophobic surface by control of its crystallization behavior," *Macromol. Rapid Commun.*, vol. 25, pp. 1606–1610, 2004.

[170] X. Song, J. Zhai, Y. Wang, and L. Jiang, "Fabrication of superhydrophobic surfaces by self-assembly and their water-adhesion properties," *J. Chem. Phys. B*, vol. 109, pp. 4048–4052, 2005.

[171] J. T. Han, Y. Zheng, J. H. Cho, X. Xu, and K. Cho, "Stable superhydrophobic organic-inorganic hybrid films by electrostatic self-assembly," *J. Chem. Phys. B*, vol. 109, pp. 20773–20778, 2005.

[172] S. Srinivasan, V. K. Praveen, R. Philip, and A. Ajayaghosh, "Bioinspired superhydrophobic coatings of carbon nanotubes and linear π systems based on the 'bottom-up' self-assembly approach," *Angew. Chem. Int. Ed.*, vol. 120, pp. 5834–5838, 2008.

[173] X. Song, J. Zhai, Y. Wang, and L. Jiang, "Self-assembly of amino-functionalized monolayers on silicon surfaces and preparation of superhydrophobic surfaces based on alkanoic acid dual layers and surface roughening," *J. Colloid Interface Sci.*, vol. 298, pp. 267–273, 2006.

[174] K.-S. Liao, A. Wan, J. D. Batteas, and D. E. Bergbreiter, "Superhydrophobic surfaces formed using layer-by-layer self-assembly with aminated multiwall carbon nanotubes," *Langmuir*, vol. 24, pp. 4245–4253, 2008.

[175] M. Manca, A. Cannavale, L. De Marco, A. S. Aricò, R. Cingolani, and G. Gigli, "Durable superhydrophobic and antireflective surfaces by trimethylsilanized silica nanoparticles-based sol-gel processing," *Langmuir*, vol. 25, pp. 6357–6362, 2009.

[176] K. Tadanaga, J. Morinaga, and T. Minami, "Formation of superhydrophobic-superhydrophilic pattern on flowerlike alumina thin film by the sol-gel method," *J. Sol-Gel Sci. Tech.*, vol. 19, pp. 211–214, 2000.

[177] K. Tadanaga, K. Kitamuro, A. Matsuda, and T. Minami, "Formation of superhydrophobic alumina coating films with high transparency on polymer substrates by the sol-gel method," *J. Sol-Gel Sci. Tech.*, vol. 26, pp. 705–708, 2003.

[178] N. J. Shirtcliffe, G. Mchale, M. I. Newton, and C. C. Perry, "Intrinsically Superhydrophobic Organosilica Sol-Gel Foams," *Langmuir*, vol. 104, pp. 7777–7782, 2003.

[179] K. Tadanaga and J. Morinaga, "Micropatterning on flowerlike alumina coating film by the sol-gel method," *Chem. Mater.*, vol. 944, pp. 590–592, 2000.

[180] M. Callies, Y. Chen, F. Marty, A. Pépin, and D. Quéré, "Microfabricated textured surfaces for super-hydrophobicity investigations," *Microelectron. Eng.*, vol. 78, pp. 100–105, 2005.

[181] H. Liu, L. Feng, J. Zhai, L. Jiang, and D. Zhu, "Reversible wettability of a chemical vapor deposition prepared ZnO film between superhydrophobicity and superhydrophilicity," *Langmuir*, vol. 20, pp. 5659–5661, 2004.

[182] T. Sun, G. Wang, L. Feng, B. Liu, Y. Ma, L. Jiang, and D. Zhu, "Reversible switching between superhydrophilicity and superhydrophobicity," *Angew. Chem. Int. Ed.*, vol. 43, pp. 357–360, 2004.

[183] H. S. Lim, J. T. Han, D. Kwak, M. Jin, and K. Cho, "Photoreversibly switchable superhydrophobic surface with erasable and rewritable pattern," *J. Am. Chem. Soc.*, vol. 128, pp. 14458–14459, 2006.

[184] A. Nakajima, A. Fujishima, K. Hashimoto, and T. Watanabe, "Preparation of transparent superhydrophobic boehmite and silica films by sublimation of aluminum acetylacetonate," *Adv. Mater.*, vol. 11, pp. 1365–1368, 1999.

[185] N. Verplanck, E. Galopin, J.-C. Camart, V. Thomy, Y. Coffinier, and R. Boukherroub, "Reversible electrowetting on superhydrophobic silicon nanowires," *Nano Lett.*, vol. 7, pp. 813–817, 2007.

[186] L. Feng, Y. Zhang, J. Xi, Y. Zhu, N. Wang, F. Xia, and L. Jiang, "Petal effect: A superhydrophobic state with high adhesive force," *Langmuir*, vol. 24, pp. 4114–4119, 2008.